

INFORMATION TO USERS

This was produced from a copy of a document sent to us for microfilming. While the most advanced technological means to photograph and reproduce this document have been used, the quality is heavily dependent upon the quality of the material submitted.

The following explanation of techniques is provided to help you understand markings or notations which may appear on this reproduction.

1. The sign or "target" for pages apparently lacking from the document photographed is "Missing Page(s)". If it was possible to obtain the missing page(s) or section, they are spliced into the film along with adjacent pages. This may have necessitated cutting through an image and duplicating adjacent pages to assure you of complete continuity.
2. When an image on the film is obliterated with a round black mark it is an indication that the film inspector noticed either blurred copy because of movement during exposure, or duplicate copy. Unless we meant to delete copyrighted materials that should not have been filmed, you will find a good image of the page in the adjacent frame.
3. When a map, drawing or chart, etc., is part of the material being photographed the photographer has followed a definite method in "sectioning" the material. It is customary to begin filming at the upper left hand corner of a large sheet and to continue from left to right in equal sections with small overlaps. If necessary, sectioning is continued again—beginning below the first row and continuing on until complete.
4. For any illustrations that cannot be reproduced satisfactorily by xerography, photographic prints can be purchased at additional cost and tipped into your xerographic copy. Requests can be made to our Dissertations Customer Services Department.
5. Some pages in any document may have indistinct print. In all cases we have filmed the best available copy.

University
Microfilms
International

300 N. ZEEB ROAD, ANN ARBOR, MI 48106
18 BEDFORD ROW, LONDON WC1R 4EJ, ENGLAND

8017764

EDDY, JAMES WALTER, JR.

THE EFFECT OF COHERENT MAGNETIC BREAKDOWN ON THE DE
HAAS - VAN ALPHEN EFFECT IN MAGNESIUM

The University of Arizona

PH.D.

1980

**University
Microfilms
International**

300 N. Zeeb Road, Ann Arbor, MI 48106

18 Bedford Row, London WC1R 4EJ, England

THE EFFECT OF COHERENT MAGNETIC BREAKDOWN
ON THE de HAAS-van ALPHEN EFFECT IN MAGNESIUM

by

James Walter Eddy, Jr.

A Dissertation Submitted to the Faculty of the

DEPARTMENT OF PHYSICS

In Partial Fulfillment of the Requirements
For the Degree of

DOCTOR OF PHILOSOPHY

In the Graduate College

THE UNIVERSITY OF ARIZONA

1 9 8 0

THE UNIVERSITY OF ARIZONA
GRADUATE COLLEGE

As members of the Final Examination Committee, we certify that we have read
the dissertation prepared by James Walter Eddy, Jr.

entitled THE EFFECT OF COHERENT MAGNETIC BREAKDOWN ON THE
de HAAS - van ALPHEN EFFECT IN MAGNESIUM

and recommend that it be accepted as fulfilling the dissertation requirement
for the Degree of Doctor of Philosophy.

Res. Starb

1/29/80
Date

Roald K Wangness

29 January 1980
Date

Michael D. Scadron

1/29/80
Date

Kog M. Emich

29 Jan 1980
Date

Date

Final approval and acceptance of this dissertation is contingent upon the
candidate's submission of the final copy of the dissertation to the Graduate
College.

I hereby certify that I have read this dissertation prepared under my
direction and recommend that it be accepted as fulfilling the dissertation
requirement.

Res Starb

Dissertation Director

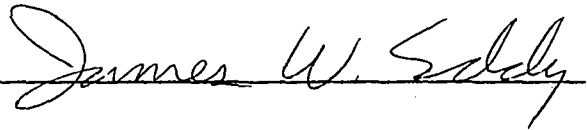
1/29/80
Date

STATEMENT BY AUTHOR

This dissertation has been submitted in partial fulfillment of requirements for an advanced degree at The University of Arizona and is deposited in the University Library to be made available to borrowers under rules of the Library.

Brief quotations from this dissertation are allowable without special permission, provided that accurate acknowledgment of source is made. Requests for permission for extended quotation from or reproduction of this manuscript in whole or in part may be granted by the head of the major department or the Dean of the Graduate College when in his judgment the proposed use of the material is in the interest of scholarship. In all other instances, however, permission must be obtained from the author.

SIGNED:

A handwritten signature in cursive script, reading "James W. Saddy", written over a horizontal line.

For my wife, Cecelia

ACKNOWLEDGMENT

I want very much to take this opportunity to thank my advisor, Royal Stark, for his sure guidance and inspiration throughout every aspect of this work. I learned how to do experimental research in graduate school and this was due principally to the teaching of my advisor.

I wish to thank Richard Young and Niranjan Sandesara for their enthusiasm and for many discussions which helped to improve my understanding of this problem. I am also grateful to Roy Emrick for his help in preparing this dissertation, to John Kupter for analyzing some of the data, to Elaine Segura for her typing and editing skills, and to John Howe for drawing the many figures contained within these pages. Special thanks to my wife, Cecelia, for her support and encouragement throughout my graduate school years and for the many hours spent working at my side to finish this dissertation on time.

TABLE OF CONTENTS

	Page
LIST OF ILLUSTRATIONS	vi
LIST OF TABLES	ix
ABSTRACT	x
1. INTRODUCTION	1
The Coupled Orbit Network	1
The de Haas-van Alphen Effect	29
Previous Investigations of the Coupled Orbit System	37
Pippard's Model Band Structure	37
The Predictions of Falicov and Stachowiak	53
2. EXPERIMENTAL TECHNIQUE	64
The Crystal and the Crystal Mount	64
The Cryostat	69
The Electronics	79
The Detection System	79
The Data Processing System	89
3. THE EXPERIMENTAL DATA	102
4. INTERPRETATION OF THE DATA	133
5. CONCLUSIONS	156
APPENDIX A: A CONVERS CASE STUDY	158
REFERENCES	183

LIST OF ILLUSTRATIONS

Figure	Page
1. The Fermi surface of Mg in the extended zone scheme	5
2. The Fermi surface of Mg in the reduced zone scheme	7
3. The hexagonal orbit	12
4. The coupled orbit network	15
5. Energy levels corresponding to the free-electron-like orbit	20
6. Energy levels of a simple hypothetical atom	22
7. Broadening of degenerate valence levels into bands as interatomic spacing is decreased	23
8. Broadening of degenerate Landau levels into bands as interorbital coupling is increased	25
9. Schematic density of states for a narrow slab cut through the Fermi surface normal to the applied magnetic field	26
10. The MB switching model: (a) amplitude and phase relationships at a junction, (b) the geometry of switching from orbit 0_1 to orbit 0_2	39
11. The hexagonal network, showing areas 2ξ , 2η , δ , and Δ . . .	42
12. Assumed amplitudes on the network: (a) around one orbit, (b) in the unit cell	43
13. The 0-lattice Brillouin zone, showing contours of constant $C(\vec{\kappa})$	50
14. Energy band structure for hexagonal network $\gamma_p = 31/5$	52
15. Selected simple closed orbit trajectories	56
16. The predicted magnetic field dependence of the amplitude of the oscillatory magnetization for a few selected simple closed orbits	60

LIST OF ILLUSTRATIONS--Continued

Figure	Page
17. Qualitative representation of a typical spectrum predicted by Fig. 16	62
18. Cross-section of the crystal mounting assembly	68
19. The He ³ -He ⁴ dilution refrigerator cryostat	70
20. The detection system	82
21. Large amplitude modulation effects I	86
22. Large amplitude modulation effects II	87
23. Two field sweep dHvA spectral scans	90
24. Block diagram of the data processing hardware	92
25. Fourier transform of digitalized dHvA field sweep data . .	104
26. Two Fourier transforms showing dHvA peaks in the high frequency regime	107
27. Magnetic field dependence of coupled orbit dHvA spectra I	109
28. Magnetic field dependence of coupled orbit dHvA spectra II	110
29. Magnetic field dependence of coupled orbit dHvA spectra III	111
30. Comparison of theory and experiment for the amplitude of the A peak	117
31. Magnetic field dependence of coupled orbit dHvA spectra IV	127
32. Magnetic field dependence of coupled orbit dHvA spectra V	128
33. The density of \vec{k} states $\eta(C)$ as a function of C within a single band	136

LIST OF ILLUSTRATIONS--Continued

Figure	Page
34. The coupled orbit density of states calculated from Pippard's band structure	138
35. Fourier transform of the model density of states $\eta(\epsilon)$ for high values of q	140
36. Fourier transform of the model density of states $\eta(\epsilon)$ for intermediate and low values of q	141
37. Two simple closed orbits (a) and (b), and the interfering combination of these (c) which would be expected to produce an A- γ frequency and mass	145
38. The q dependence of the amplitude of the G peak in the coupled orbit density of states	146
39. A section of the model density of states $\eta(\epsilon)$ shown at four closely spaced magnetic field strengths	151
40. Two difference paths that enclose the Brillouin zone area $A_{BZ}^{(r)}$	154

LIST OF TABLES

Table		Page
1.	Symmetry properties of a few selected orbits	58
2.	Fit parameters for three-segment fifth degree polynomial representation of $\eta(C)$	137
3.	An abridged listing of 8080 assembly code	167
4.	An abridged 8080 assembler defined in Convers code	170

ABSTRACT

We report here the results of a de Haas-van Alphen (dHvA) investigation of the coupled orbit system in magnesium. The data were taken for magnetic fields extending to 52 kG and temperatures down to 0.29^oK. The experimental data are interpreted in the light of coupled orbit system theories of Pippard and of Falicov and Stachowiak; these are each reviewed in some detail. The data are found to disagree qualitatively with the predictions of Falicov and Stachowiak. Since this theory has been assumed, for more than a decade, to be equivalent to Pippard's theory, a detailed comparison of these was made. Full spectrum Fourier analysis of Pippard's band structure density of states shows that the two models disagree qualitatively and, therefore, that they are not equivalent. These experimental results, which do not appear to disagree with Pippard's theory, are interpreted to mean that it is finally possible to obtain crystals of sufficient purity and perfection to make it necessary to use a band structure description of the delocalized electrons on the coupled network.

Evidence is presented for the existence of a new type of dHvA frequency corresponding to the PKM plane cross-section of the Brillouin zone. A proposed explanation for this dHvA frequency involves the field dependent modulation of the zero frequency component of the Fourier transform of the coupled orbit system density of states.

Also included are discussions of crystal preparation and handling, cryogenic apparatus, analogue detection apparatus, digital data acquisition and processing hardware based on a microcomputer, and a new software system ideally suited to small computer research environments.

CHAPTER 1

INTRODUCTION

This dissertation will present results of an experimental study of the coupled orbit network in magnesium. The existence of this network is one manifestation of a phenomenon called magnetic breakdown. The method of observation invokes the measurement of a second phenomenon, the de Haas-van Alphen effect. None of these three subjects can be discussed without considerable specialized vocabulary. A principal goal of this introduction is to define the terms and concepts necessary to an understandable discussion of the problem. The introduction is divided into three sections. The first section deals with the relevant physical properties of Magnesium, the nature of magnetic breakdown, and the existence of the coupled orbit network. The second section is a brief discussion of the de Haas-van Alphen effect. The third section is a review of the previous investigations of the coupled orbit system that forms the context which aids in understanding the meaning of the present work.

A concise statement of the reasons for the interest in the coupled orbit problem is included at the end of the first section.

The Coupled Orbit Network

In the one-electron theory of metals, the equations of motion for conduction electrons in the presence of externally applied electric and magnetic fields are

$$\hbar \dot{\vec{k}} = -|e| \left[\vec{E} + \frac{1}{c} \vec{V}_n(\vec{k}) \times \vec{H} \right] \quad (1.1)$$

$$\vec{v}_n(\vec{k}) = \frac{1}{\hbar} \vec{v}_k e_n(\vec{k}) \quad (1.2)$$

In these equations $\vec{v}_n(\vec{k})$ is the group velocity of the electron wave packet with band index n , centered on the state \vec{k} , and the set of functions $e_n(\vec{k})$ define the band structure of the metal. These equations differ from the free electron equations of motion only in the fact that $e_n(\vec{k})$ appears in (1.2) instead of the free electron energy $\hbar^2 k^2/2m$, and it is therefore apparent that all of the effects associated with the presence of the periodic lattice potential are contained within the $e_n(\vec{k})$'s. The quantity $\hbar\vec{k}$ is called the crystal momentum of the electron. It is appropriately distinguished from the real momentum because it responds only to the externally applied forces, as is evident from (1.1). In addition to these equations of motion, a proper description of many observed phenomena, especially at low temperatures, requires the introduction of the concept of the Fermi surface. The Fermi surface is defined when the system is in the ground state ($T = 0^\circ\text{K}$) and all of the electrons are condensed into the lowest energy single particle states. When the system is in this state there will be a constant energy surface in \vec{k} space for which all \vec{k} states of lower energy are filled and all states of higher energy are empty. This surface is called the Fermi surface.

The importance of this concept cannot be overstressed. It is clear from Eqs. (1.1) and (1.2) that, within the one-electron theory of metals, the system response to externally applied perturbations is limited to transitions between single particle \vec{k} states. Experiments which

do not involve high energy transitions ($\gg kT$) will, therefore, produce results that are entirely determined by \vec{k} states very close to the Fermi surface since this is the only region of \vec{k} space where there is an abundance of both filled and empty states. The gradient in Eq. (1.2) indicates that the response of the electrons in these states can be related to the local geometry of the Fermi surface and the neighboring constant energy surfaces. Much of what is known about the behavior of electrons in metals can be expressed in terms of the geometry of the Fermi surface.

Among the factors that determine this geometry, the most important is the presence of the periodic lattice potential. Perhaps the easiest way to visualize the effect of this potential is by using the concept of the Brillouin zone. Brillouin zones are multifaceted enclosed volumes in \vec{k} space whose precise shape is determined solely by the geometry of the crystalline lattice. The planes which define the surfaces of the various zones delineate the regions of \vec{k} space for which the lattice potential has a significant perturbing effect on the idealized free-electron-like single particle states of the system. In other words, the Fermi surface of a metal will be distorted from the free electron sphere (which is the Fermi surface defined by the ground state of the free electron gas) in those regions of \vec{k} space where it is closest to the Brillouin zone planes. In the monovalent metals this is particularly straightforward. For these metals the number of valence electrons in the system is equal to the number of primitive cells in the lattice. For a lattice of N cells, the associated Brillouin zones each have volumes in \vec{k} space sufficient to contain N discrete \vec{k} states, and hence,

$2N$ electrons can occupy states within a single zone (there being two spin states associated with each \vec{k}). Thus, in monovalent metals, the volume of occupied states is half the zone volume, and the Fermi surface will be contained entirely within the first Brillouin zone. In many such metals (Na, K, Rb, Cs) the Fermi surface never approaches a zone plane closely enough to be deformed significantly from the free electron sphere.

In polyvalent metals or in metals whose lattice structure includes a basis, the situation is somewhat more complicated. For these metals the volume of occupied states in \vec{k} space extends out of the first zone into a number of higher zones. In such cases it is convenient to refer separately to portions of the Fermi surface that are found in the various zones; it is customary to refer to the first band sheet, the second band sheet, etc., with corresponding band index $n = 1, 2, \dots$ in Eq. (1.2).

These ideas can best be demonstrated with the aid of the specific example, magnesium (Mg), which is the object of the present study. Magnesium is a divalent metal whose lattice structure is hexagonal-close-packed (hcp) and, therefore, has a basis consisting of two atoms in each primitive cell. If the crystalline lattice includes N primitive cells there will be $4N$ occupied single electron states in the system; thus, the volume of occupied states in \vec{k} space is twice the volume of the Brillouin zone. In fact, the Mg Fermi surface extends outside of the first zone and into zones up to the fourth. In so doing, it intersects a number of perturbing zone planes and in those regions suffers deformation. In Fig. 1, the Fermi surface is shown in a display scheme (the extended zone scheme) which most clearly demonstrates its similarity to

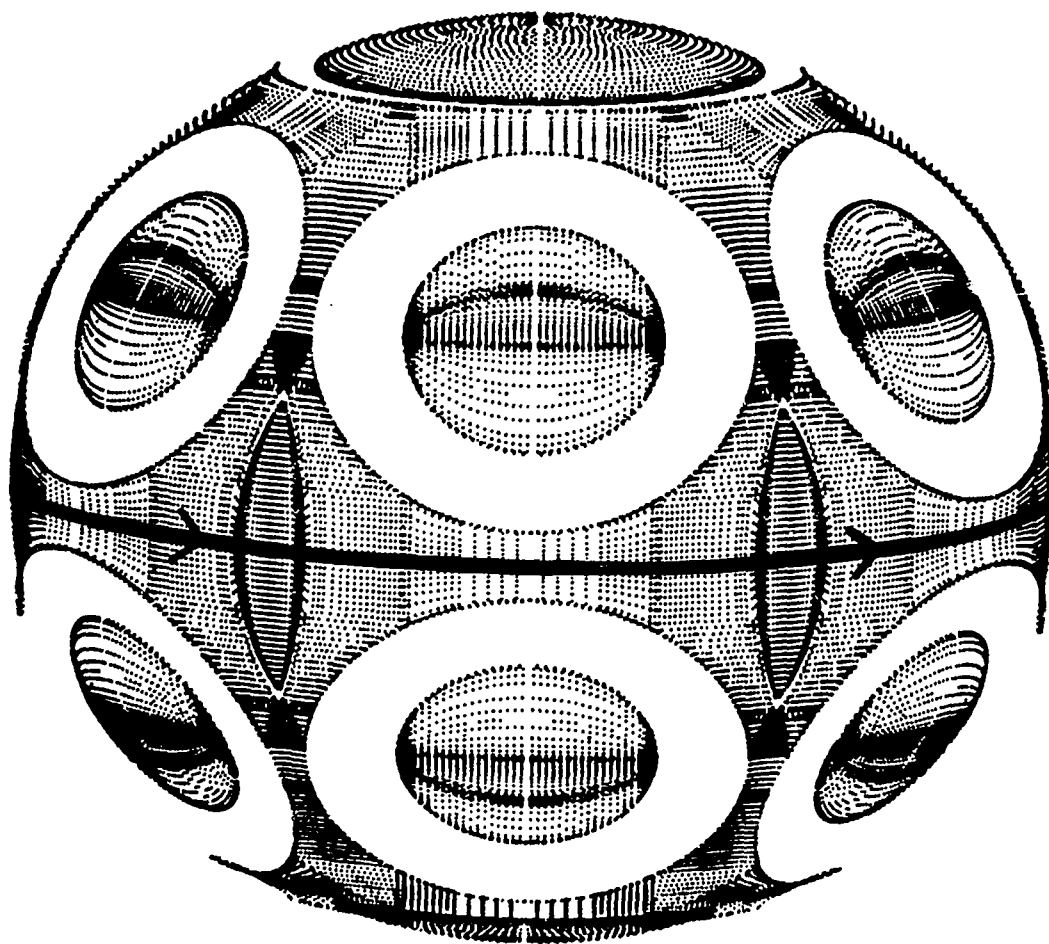


Fig. 1. The Fermi surface of Mg in the extended zone scheme.

The figure is a computer generated interpolation of data from many previous experiments. The darker areas result from the denser mesh of points in regions of high curvature. Note that the vertical dimension has been slightly compressed; the surface should have the overall shape of a sphere. The free-electron-like orbit has been drawn in.

the free electron sphere. The various gaps in the sphere are associated with the various zone planes of which three distinct types are involved; these are the $[0002]$, $[10\bar{1}0]$, and $[10\bar{1}1]$ type planes. The widths of the various gaps are determined by the strength of the Fourier coefficients of the perturbation potential associated with each type of zone plane. This representation of the Fermi surface is useful to exhibit the relatively modest energy gaps and the similarity to the free electron sphere, but it obscures the band nature of the system by failing to isolate the portions of the surface which lie in the various Brillouin zones. These ends are accomplished by an alternative display format called the reduced zone scheme. This method takes advantage of the fact that the single particle states of the system are invariant under a translation in \vec{k} space corresponding to any of the reciprocal lattice vectors \vec{G}_i . These vectors can be used to translate the disparate pieces of the various band sheets back into the first Brillouin zone. When this is done for Mg, the results appear as shown in Fig. 2. Objects (a) and (b) are hole surfaces because they enclose regions of empty states in \vec{k} space. Object (a) is the second band hole surface and it is called the "monster." Object (b) is a first band hole surface, usually called the "cap." Objects (c), (d), and (e) are all electron pockets enclosed by sheets of the third band Fermi surface. They have been named the "cigar," the "lens," and the "butterfly," respectively. The small piece of the Fermi surface that extends into the fourth zone is represented by object (f) and is called the "fourth-band-electron-pocket."

This method of displaying the Fermi surface sheds light on the meaning of Eqs. (1.1) and (1.2). It is to these various band sheets

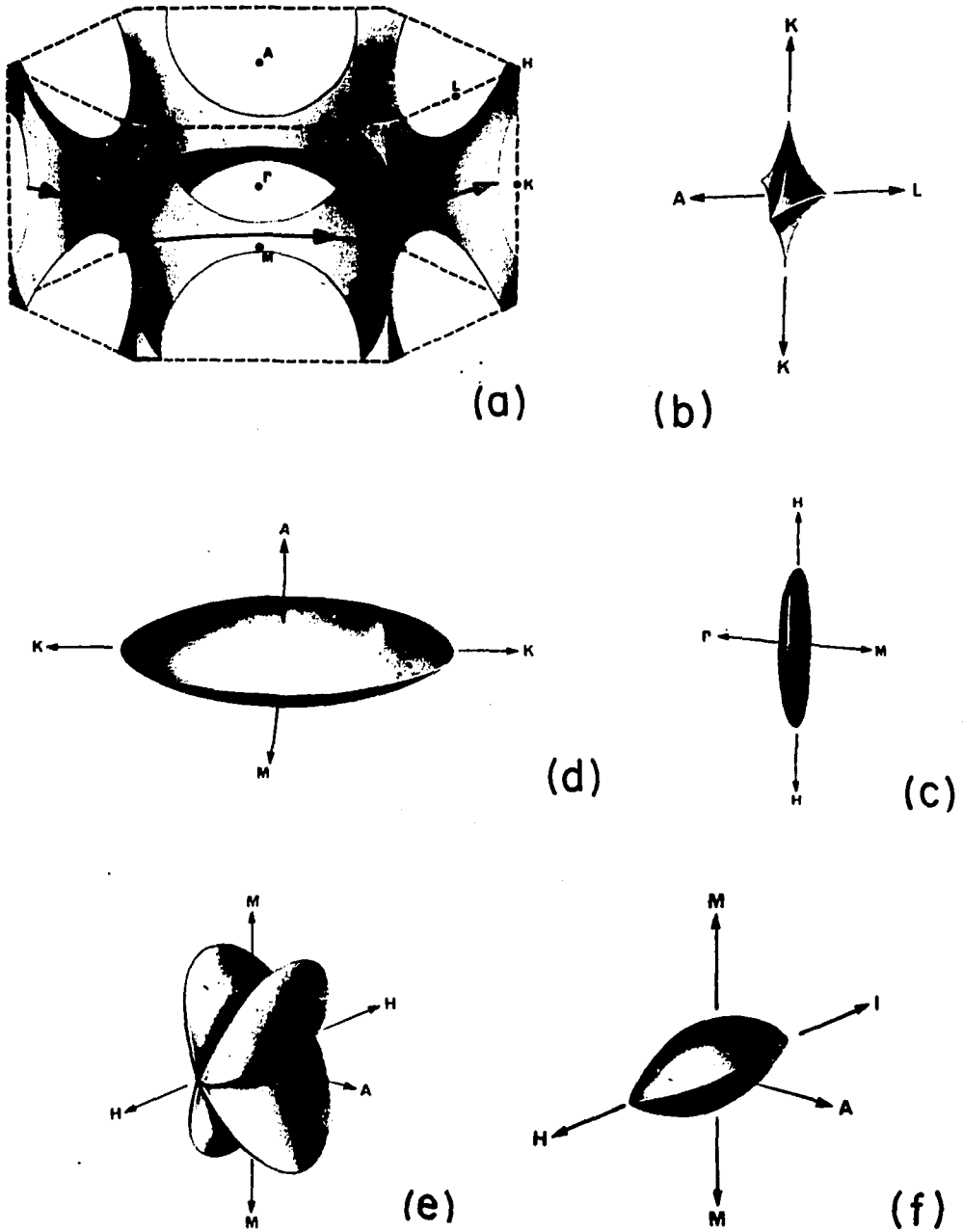


Fig. 2. The Fermi surface of Mg in the reduced zone scheme.
 The hexagonal orbit has been drawn in.

that the index n refers. The equations assert that the dynamical response of an electron on any one of the sheets of the Fermi surface can be deduced from the geometrical properties of that sheet alone, the existence of the other band sheets being completely ignored. This, of course, is an approximation since it overlooks the possibility of electron transitions from one band to another. There are experimental situations for which this approximation is valid and Eqs. (1.1) and (1.2) are essentially rigorously obeyed. In other situations the approximation completely breaks down, and in these cases experimental results are found to be qualitatively different from the predictions that derive from a rigorous application of (1.1) and (1.2). The questions of when these equations are valid and when and how they break down is a central issue in the present work.

Consider the case where only an external magnetic field is applied to the crystal. Under these conditions Eq. (1.1) reduces to

$$\hbar \dot{\vec{k}} = - \frac{|e|}{c} \vec{v}_n(\vec{k}) \times \vec{H} . \quad (1.3)$$

Since the magnetic field does not induce transitions between states of different energy, the trajectories of electrons in \vec{k} space will be along surfaces of constant energy and in planes perpendicular to the magnetic field. For an electron at the Fermi energy, the trajectory will be around the Fermi surface. If the magnetic field is applied along the direction of the Mg c-axis (directed out of the "north pole" of the Fermi surface as it is shown in Fig. 1), one of these trajectories will be around the "equator."

In Fig. 1 the dark circular arc segments that intersect the sphere represent narrow band gaps which occur at intersections with $[10\bar{1}0]$ -type Brillouin zone planes. These gaps subdivide the equatorial trajectory at twelve points around the sphere. Electrons orbiting along this trajectory will encounter these gaps and will either tunnel through and continue along the circular path or be Bragg reflected and remain on the same band sheet. When the magnetic field is high, there will be a high probability that the electron will tunnel through the gap and follow the free-electron trajectory. When the field is sufficiently low, the lattice perturbation will dominate at the gap, the electron will tend to be Bragg reflected, and the tunneling probability will be correspondingly low. This magnetic-field-induced transition between electron states on adjacent band sheets of the Fermi surface is called magnetic breakdown (MB).

MB was first proposed by Cohen and Falicov (1961) to explain this very free-electron-like orbit which, impossible in the absence of MB, was observed by Priestley in his Mg de Haas-van Alphen (dHvA) experiments (Priestley et al. 1963, and Priestley 1963). Since that time, MB has been observed in many metals (see, for example, Stark et al. 1962, Stark 1962, Young 1965, and Ashcroft 1963) and has been the subject of a number of theoretical papers. One of the important results that has come out of the theoretical work is an expression which relates the breakdown probability to the physical properties of the gap. The calculation has been done in the low field limit (Blount 1962) and in the high field limit (Pippard 1962 and Reitz 1964) and the result was the same:

$$P = \exp \left[- \frac{\pi}{4} \frac{\mathcal{E}_g^2}{\hbar H |V_x V_y|} \right]. \quad (1.4)$$

In this expression \mathcal{E}_g is the width of the energy gap, and V_x and V_y are the cartesian components of the Fermi velocity perpendicular to \vec{H} . The tunneling probability is found to be affected only by the field and by properties of the gap which are constant for a given metal. It is customary to summarize the behavior of the gap by defining an equivalent breakdown field H_0 . In terms of H_0 the breakdown probability becomes

$$P = \exp[-H_0/H]. \quad (1.5)$$

Figure 1 shows qualitatively that the energy gap that interrupts the equatorial, free-electron-like orbit is rather small. In fact, it has been shown to have a breakdown field, $H_0 = 5.85$ kG (Falicov et al. 1966). This is a rather convenient breakdown field because it permits the breakdown probability to be varied over most of the range from zero to one for magnetic fields that are common in the laboratory (2 to 100 kG).

Figure 1 is the appropriate display scheme to demonstrate the electron behavior in the high field limit because it shows clearly the closed circular trajectory that results when all of the gaps are broken down. In the low field limit, the electron response is better represented on the Fermi surface shown in Fig. 2. Consider an electron at the Fermi energy on the midplane of the monster. In the presence of a field directed along the c-axis (the sixfold rotational symmetry axis of the monster), the electron will orbit around the surface as shown in the figure. The electron approaches band gaps at the six cusps in the

orbit. If the field is sufficiently small, the electron is reflected at each of these gaps and continues around the monster. When this orbit is viewed from along the c-axis, it appears as a regular hexagonal closed trajectory made up of equal length circular arcs. The electron motion in real space is very similar to this trajectory in \vec{k} space. This can be seen by considering a wave packet moving in the basal plane of the hcp lattice (perpendicular to the c-axis) in real space. When the field is turned on, the wave packet will respond initially by following a circular free-electron path. Because of the curvature, it will travel through the lattice planes at a continuously changing angle. At some point along the path, the wave packet will be moving at the correct Bragg angle to a set of $(10\bar{1}0)$ -type planes and hence be reflected. After reflection, the free-electron trajectory is resumed until the circular path reproduces the Bragg angle at the next set of planes. Because the hcp lattice has sixfold rotational symmetry about the c-axis, the packet will be Bragg reflected six times and will follow the closed orbit shown in Fig. 3. It is clear from the figure that when the direction of closure for the free-electron path is clockwise, the direction of closure for the hexagonal path is counterclockwise. The net response to the field is that of a hole rather than an electron. Experiments which are sensitive to the ratio of electrons to holes on closed paths have been used to firmly establish the existence of this type of orbit (Stark 1964 and Stark 1965).

It is important to note that the real space orbit in Fig. 3 is exactly the same shape as the corresponding \vec{k} space orbit around the monster in Fig. 2. This will be true in general. When Eq. (1.3) is

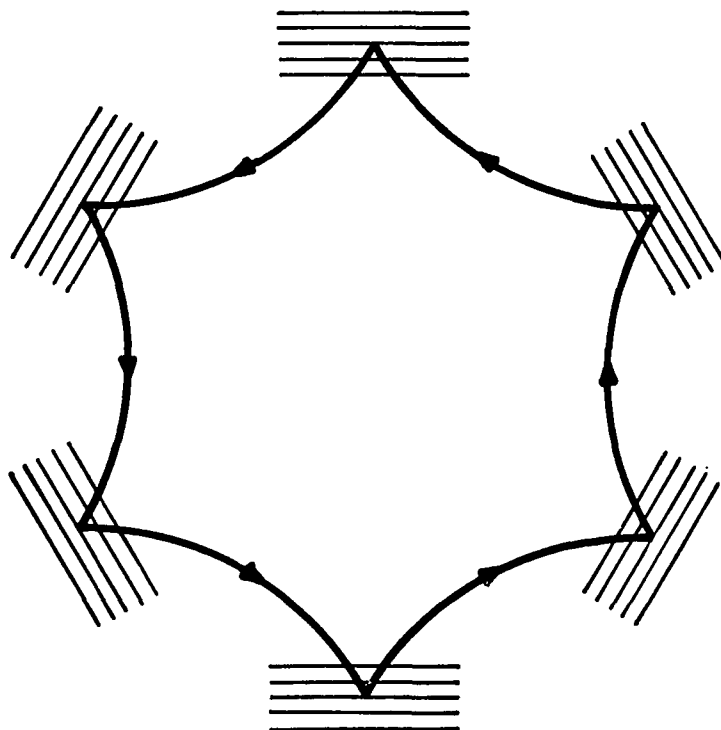


Fig. 3. The hexagonal orbit.

The $(10\bar{1}0)$ -type lattice planes responsible for Bragg reflection are shown schematically at each cusp.

integrated with respect to time, the result is an expression relating the components of \vec{k} and \vec{r} that are perpendicular to the field. If the z-axis is chosen along the field direction, the component k_z (as well as the energy) will be a constant of the motion. The other components are given by

$$\begin{aligned} k_x &= -\alpha(y-y_0) \\ k_y &= -\alpha(x-x_0) \end{aligned} \tag{1.6}$$

where k_x , k_y , y , and x are explicit functions of time and α is a field-dependent scale factor given by

$$\alpha \equiv \beta^{-1} = \frac{|e|H}{\hbar c} . \tag{1.7}$$

The trajectories of electrons in \vec{r} space normal to \vec{H} are the same as the trajectories in \vec{k} space after a rotation by $\pi/2$ and a multiplication by α . This is an exceedingly useful result for transforming orbital properties back and forth between \vec{k} space and \vec{r} space.

One reminder is worthy of mention before leaving this discussion of the correspondence between \vec{k} space and \vec{r} space orbits. A single orbit in \vec{k} space consists of a great number of one-electron \vec{k} states which have the same energy. Each such orbit describes the trajectories of many electrons in real space. Each real space trajectory is the same shape as the \vec{k} space trajectory, but they bear no particular spatial relationship to one another except to say that they are uniformly distributed throughout the crystal. This chaotic jumble of real space orbits is not nearly as unwieldy as it may seem at first. The periodic

lattice potential imposes an ordering of the orbits into manageable, even elegantly simple, subgroups. This brings the present discussion to the third MB regime for this orbit system, that of intermediate fields (5 to 30 kG) where tunneling and reflection have comparable probabilities.

Consider briefly the high field limit when all of the MB junctions on the equatorial orbit of Fig. 1 are broken down. The corresponding real space trajectories are free-electron-like circular paths distributed uniformly throughout the crystal. Since the orbital centers are much more closely spaced than an orbital diameter, each real space orbit will intersect many neighboring free-electron orbits, and necessarily, some of these neighbors will intersect at the appropriate angle for Bragg reflection. In the high field limit, this does not matter; the orbits are completely decoupled because the lattice potential is dominated by the field. But as the field is turned lower, the lattice can couple orbits which intersect at the correct angle to a set of $(10\bar{1}0)$ -type lattice planes. It is, therefore, appropriate in the intermediate field range of MB to consider as a subgroup all of the real space orbits that can be coupled by the lattice potential. Because of the sixfold symmetry of the lattice, this subgroup is a regular hexagonal network of circular orbits as shown in Fig. 4. It is important to note that there will be many other hexagonal networks, some of which will be only slightly displaced from the one shown, but because each network subgroup contains all of the orbits which can be coupled by the lattice, there will be no residual coupling between adjacent networks. The physics of each network can be considered independently and the

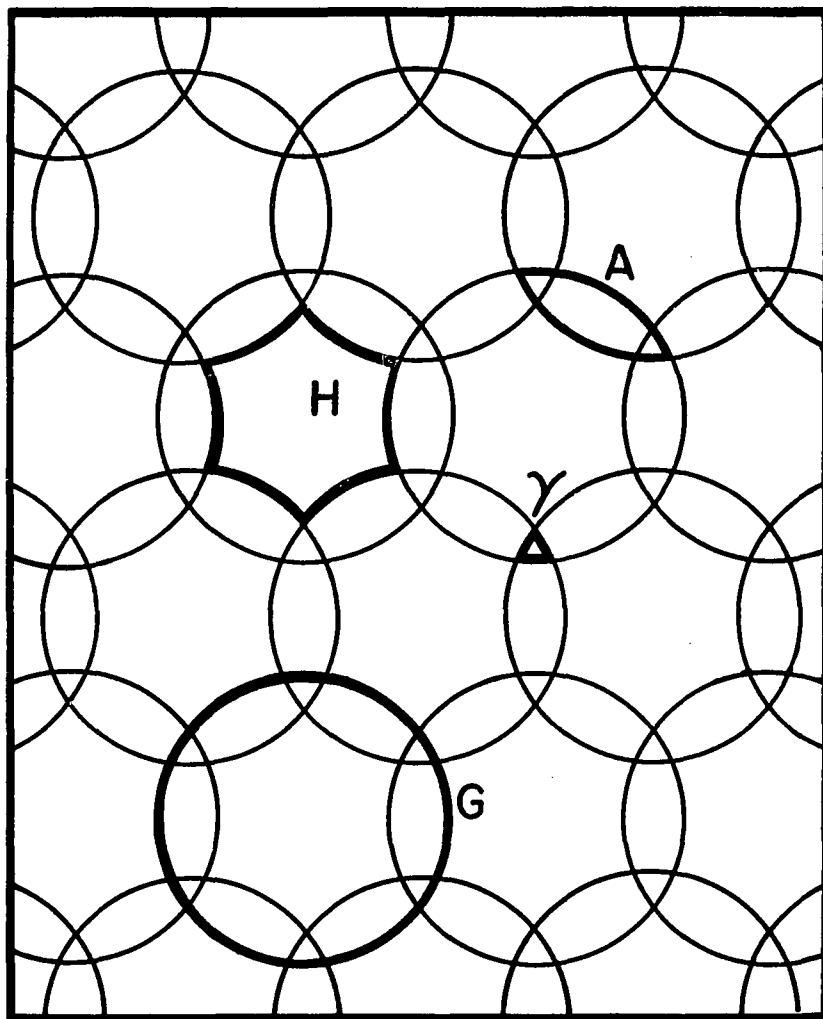


Fig. 4. The coupled orbit network.

This figure can be interpreted as representing the network in \vec{r} space or in \vec{K} space. The orbits G, H, γ , and A are drawn in.

result summed over all such networks to get the total contribution of the crystal.

There is an alternative and equally valid derivation of this coupled orbit network which begins in \vec{k} space and which involves yet a third display format for the Fermi surface called the repeated zone scheme. This display scheme once again exploits the fact that \vec{k} states are invariant under a \vec{G}_i vector translation. For example, consider the reciprocal lattice vector $\vec{G}_{10\bar{1}0}$ which extends from Γ through M in Fig. 2a. This vector can be used to translate each state \vec{k} on the monster to an equivalent state $\vec{k} + \vec{G}_{10\bar{1}0}$, and in this way the entire monster can be translated through the plane containing M. This process can be repeated for all the equivalent $(10\bar{1}0)$ -type lattice planes (the vertical planes in the figure), and the result will be a complex connected surface extending in all directions parallel to the basal (ΓMK) plane. The \vec{G} 's that extend vertically (\vec{G}_{0001} and $\vec{G}_{000\bar{1}}$) can then be used to stack monsters to arbitrary depth normal to the basal plane. This representation of the Fermi surface is most suitable for display of open orbit dynamics and dynamics of orbits which involve two or more band sheets, and it is the latter situation which is of concern here.

Consider once more the midplane orbit of Fig. 2a. In the intermediate field regime there is an appreciable probability for tunneling off of the monster at the cusps in the orbit. The other band involved in this transition is the cigar (third band electron sheet) which is located at each of the HKH lines where the monster approaches the zone boundary. In the repeated zone scheme there will be a cigar at each equivalent point K, and each will be approached on three sides by

adjacent monsters. A planar slice through this complex Fermi surface defines the same regular hexagonal network shown in Fig. 4. The small triangular paths are the midplane cross-section of the cigar; the hexagonal orbits are the cross-section of the monster. Getting back to the network of coupled orbits in real space is now just a matter of applying the transformation given by (1.6) and (1.7).

For ease of reference, it is customary to name the simplest orbit types that are possible on this network. The circular orbit is called G (for "Giant" orbit), the hexagonal orbit is H, and the triangular orbit is called γ . In the high field limit, the only orbit present is G. In the low field limit, the only orbits possible are H and γ . In addition, the lens-shaped orbit (with a γ at each end) is called the A orbit. This orbit involves four tunnelings and two reflections and is most probable at intermediate fields.

Up to this point the discussion of the coupled orbits has been in terms of position and momentum trajectories of the electrons on the network. The system can also be described in terms of its energy level structure, and this point of view is particularly useful in understanding the present interest in the problem. It has been pointed out previously that the effect of the magnetic field is to cause the electrons to orbit on surfaces of constant energy. What has not been included in the discussion so far is the well-established fact that such orbits are quantized. The Bohr-Sommerfeld quantization rule requires that the flux through a closed electron orbit be an integral multiple of the fundamental magnetic flux quantum $\frac{hc}{e}$ (within an additive constant γ). This imposes a condition on the areas of allowed orbits in

real space:

$$A^{(r)} = \frac{\hbar c}{eH} (n+\gamma) = \frac{2\pi}{\alpha} (n+\gamma),$$

$$n = 1, 2, \dots$$
(1.8)

The transformation to \vec{k} space is just a matter of multiplying the above result by α^2 (from Eqs. (1.6) and (1.7)):

$$A^{(k)} = 2\pi\alpha(n+\gamma).$$
(1.9)

This is the Onsager rule for allowed areas in \vec{k} space. The quantity $2\pi\alpha\gamma$ is the area of the orbit with zero point energy. This quantization condition can be used to establish the energy spacing of the constant energy surfaces upon which the electrons orbit:

$$\Delta\mathcal{E} = \frac{\partial\mathcal{E}}{\partial A^{(k)}} \Delta A^{(k)} = \frac{2\pi eH}{\hbar c} \frac{\partial\mathcal{E}}{\partial A^{(k)}}.$$
(1.10)

It is customary to define the cyclotron effective mass as

$$m^* \equiv \frac{\hbar^2}{2\pi} \frac{\partial A^{(k)}}{\partial\mathcal{E}}$$
(1.11)

so that Eq. (1.10) may be rewritten in a more suggestive form

$$\hbar\omega_c = \Delta\mathcal{E} = \hbar \frac{eH}{m^* c}.$$
(1.12)

The cyclotron frequency ω_c is analogous to the free-electron cyclotron frequency with the free-electron mass having been replaced by the effective mass m^* . Note that the effective mass m^* is a property of an orbit and not of a particular \vec{k} state. The allowed energies for the orbiting electrons can now be written as

$$\mathcal{E} = \hbar\omega_c (n+\gamma) \quad (1.13)$$

which is essentially the result for the harmonic oscillator. This fundamental feature of the motion of free electrons in the presence of a magnetic field is preserved for electrons in the solid.

There is another way to express the effective mass which will prove useful in later sections. The identity

$$\frac{2\pi}{\omega_c} \equiv \oint dt = \oint \frac{dk_{\perp}}{\dot{k}_{\perp}} = \frac{\hbar c}{eH} \oint \frac{dk_{\perp}}{V_{\perp}} \quad (1.14)$$

where k_{\perp} and V_{\perp} are the components of \vec{k} and \vec{V} that are perpendicular to the field, used to make the identification:

$$m^* = \frac{\hbar}{2\pi} \oint \frac{dk_{\perp}}{V_{\perp}} . \quad (1.15)$$

This result emphasizes the fact that the effective mass is related to the time for propagation around the orbit.

These ideas are most easily included into the discussion of the coupled orbit network when \vec{H} is large enough to put the system into the high field MB regime (and \vec{H} along the c-axis as always). In this limit, electrons at or near the Fermi energy \mathcal{E}_F , with zero crystal momentum along the field ($k_H = 0$), will follow the Gorbit. Electrons at lower energy will also follow circular orbits. The separation in \vec{k} space areas will be $2\pi\alpha$ [from (1.9)]. The spacing energy will be $\hbar\omega_G$. The energy levels are just those of the harmonic oscillator (Fig. 5), where each level is now highly degenerate, representing many single particle states.

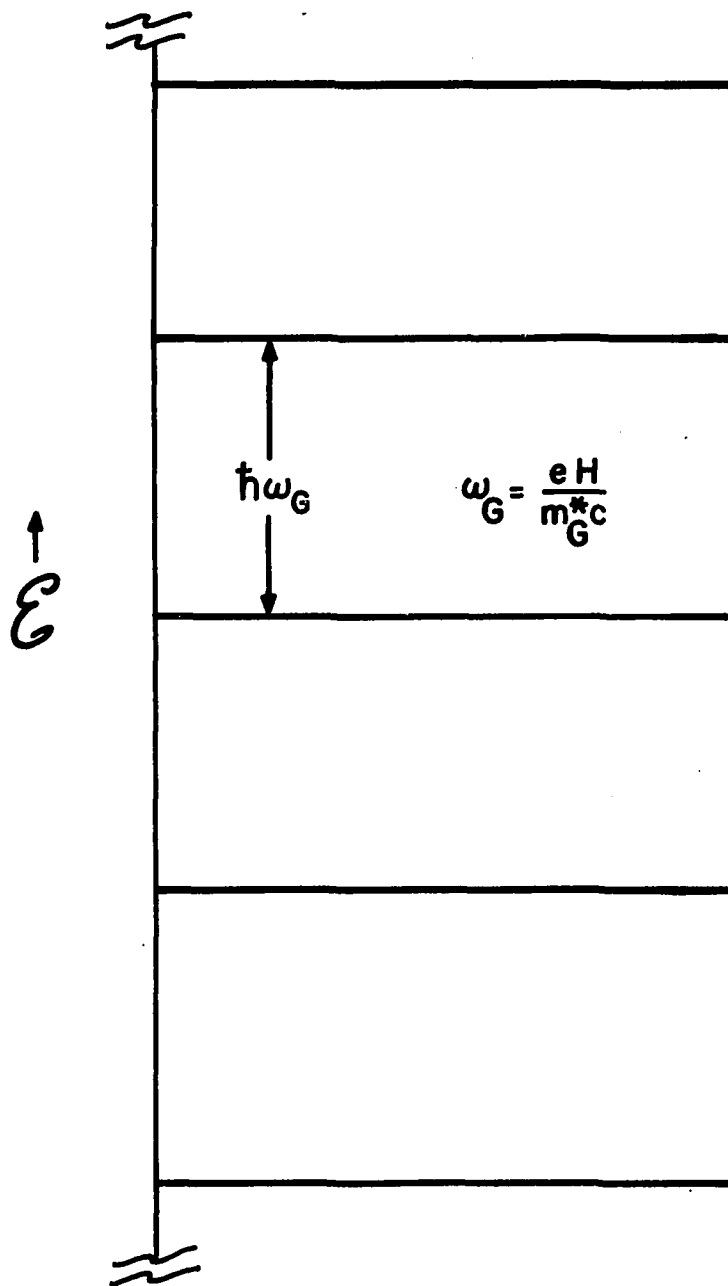


Fig. 5. Energy levels corresponding to the free-electron-like orbit.

Each level is highly degenerate, representing many single particle states.

As the magnetic field is turned lower, thereby introducing coupling among the various linked orbits, the effect upon the levels is to cause them to broaden, even to overlap. This behavior can be understood by analogy with the broadening of energy levels which occurs when a collection of identical atoms is brought together to form a crystal. Consider a system of N identical atoms of some metal, each one having an energy level structure represented by the diagram in Fig. 6. If these atoms are sufficiently far apart to rule out interactions between electrons on different atoms, Fig. 6 can be reinterpreted to represent the entire system, each level being N -fold degenerate (assuming for simplicity that each isolated atomic level is nondegenerate). When the atoms are brought together to form a crystal, the atomic wave functions of the valence electrons will overlap the sites of neighboring atoms. In those solids where only the overlap with nearest neighbor atoms need be considered (the tight binding approximation), the broadening of the energy bands can be written explicitly in terms of the overlap integrals with nearest neighbor wave functions. The level broadening that results from this overlap is shown schematically in Fig. 7 as a function of R^{-1} , where R is the interatomic separation. The hypothetical metal is assumed to have valence electron wave functions with significant overlap on nearest neighbor sites and "core" electron wave functions with very little overlap.

When the analogy is made with the two dimensional lattice of orbits, the basis states which describe the uncoupled system are not the atomic wave functions but rather the Landau orbital wave functions which describe the electrons on circular orbits in the free-electron

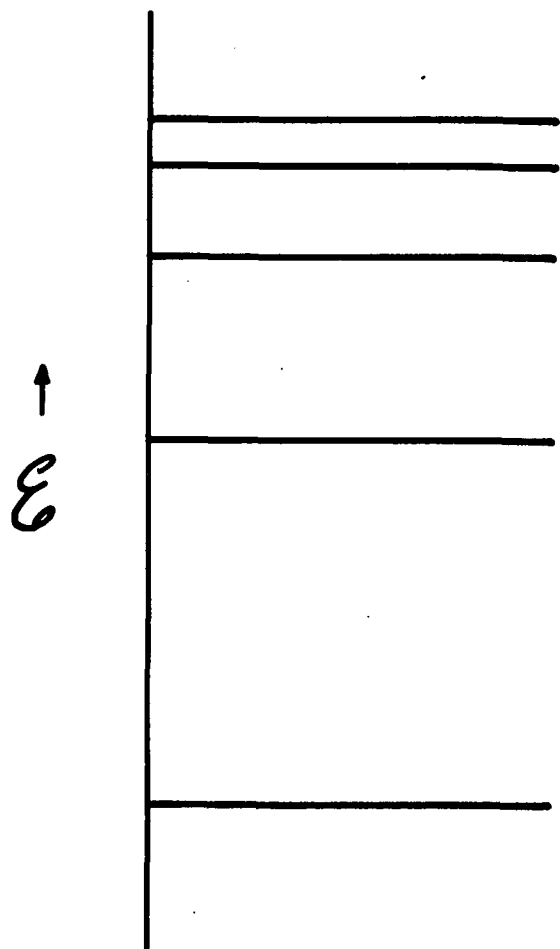


Fig. 6. Energy levels of a simple hypothetical atom.

The figure can also be interpreted as representing N completely independent atoms, in which case each level is N -fold degenerate.

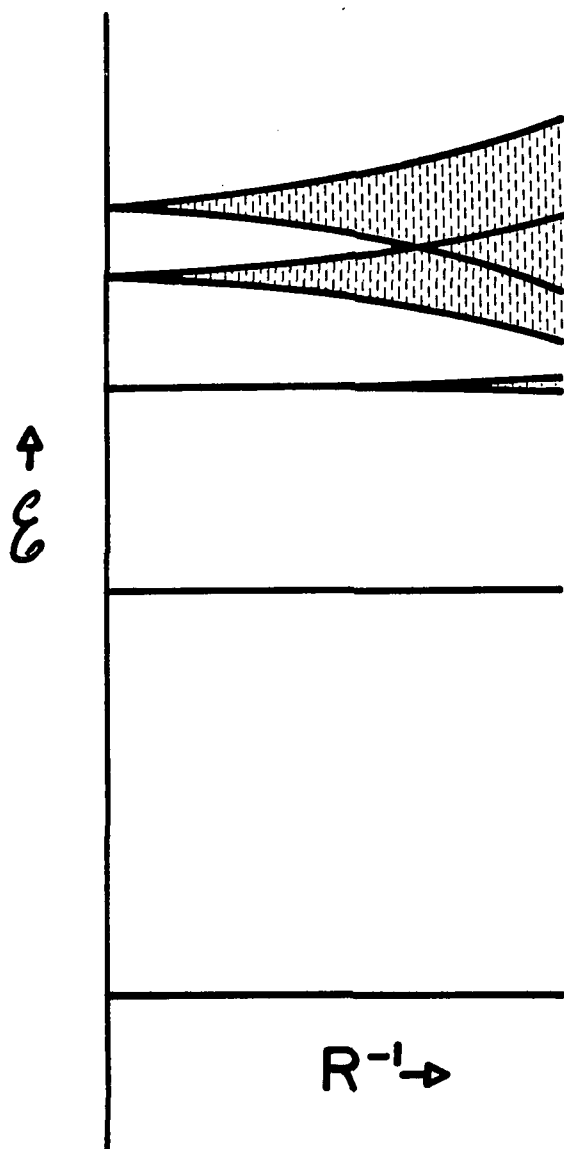


Fig. 7. Broadening of degenerate valence levels into bands as interatomic spacing is decreased.

limit. The coupling parameter is not the separation between adjacent orbits; it is instead the probability Q for Bragg reflection at a MB junction (Q can be expressed as $Q = 1 - P$ where P is the tunneling probability given by (1.4) or (1.5)). These differences do not change the fact that the overlap between adjacent orbits will force a broadening in the energy levels when the coupling is turned on. This effect on the G orbits is shown schematically in Fig. 8 where the levels shown are meant to represent the situation close to the Fermi energy. For all such levels the overlap with neighbor orbits is nearly the same, and consequently, the broadening does not change very much from level to level. Another stipulation implicit in this diagram is that Q remain small. When Q gets large, the effects of proximity to energy levels corresponding to the γ and H orbits become significant. This will be explored in greater detail in later sections.

The information presented by Fig. 8 can also be displayed in terms of a density of states $\eta(\mathcal{E})$. Figure 9 shows the density of states for the electrons in the coupled orbit system both for the high field limit ($Q = 0$) and for somewhat lower field where a small amount of coupling occurs between orbits ($Q = 0.1$). This is a highly schematic representation, but it displays clearly the essential features of a band structure: regions of energy where there are many allowed states of the system separated by gaps where states are forbidden. It is important to note that this band structure will exist only if the coupling between neighbor orbits is coherent. Quantum mechanical phase is not randomized in the Bragg reflection process, nor is it randomized by MB tunneling. It is only the coherent nature of these coupling processes

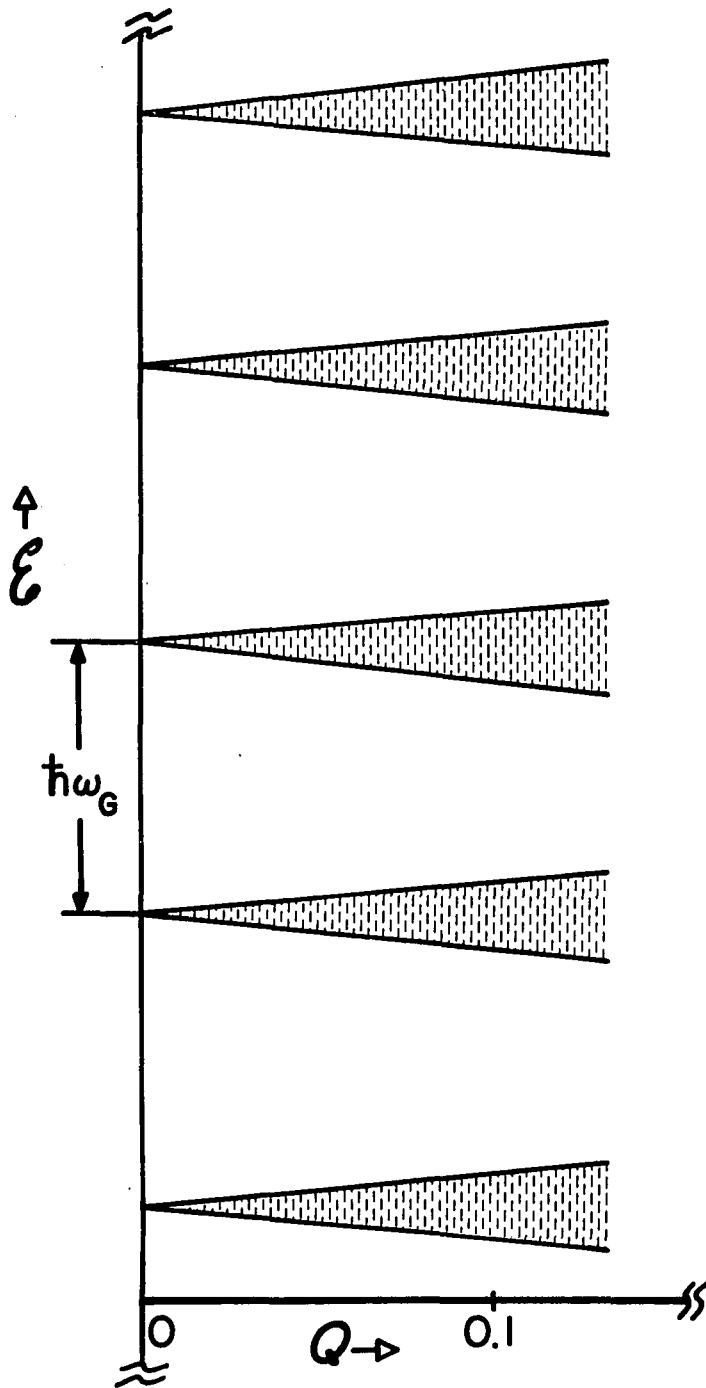


Fig. 8. Broadening of degenerate Landau levels into bands as interorbital coupling is increased.

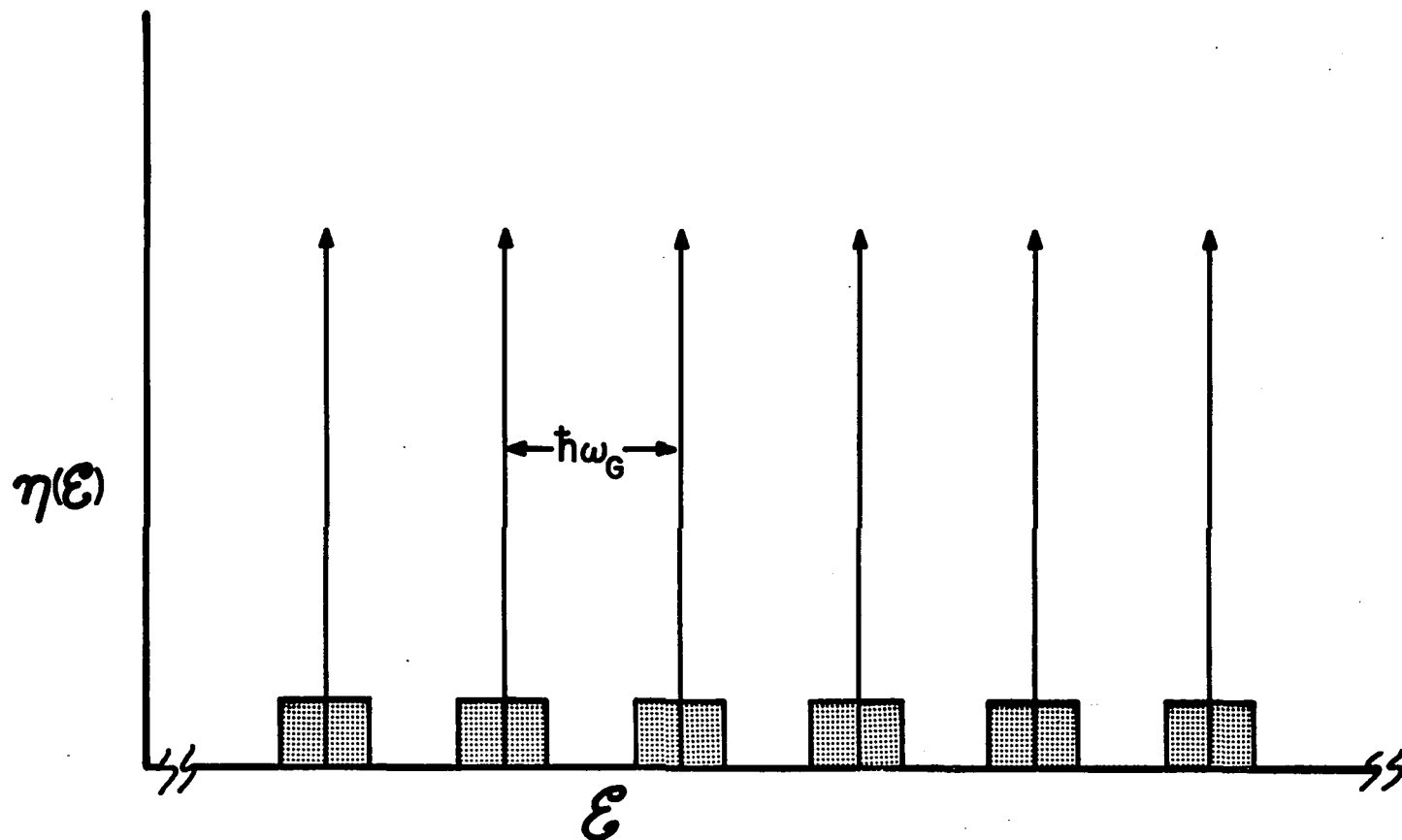


Fig. 9. Schematic density of states for a narrow slab cut through the Fermi surface normal to the applied magnetic field.

The δ function series (represented by the vertical arrows) corresponds to the high field limit of MB where only G orbits exist. The series of broad bands corresponds to a lower field where the lattice has begun to couple neighboring orbits.

that gives rise to the possibility of observing band structure effects associated with the two dimensional lattice of orbits.

It is now possible to discuss the reasons for interest in this coupled orbit problem. Suppose a perfect Mg crystal were placed in a magnetic field \vec{H} directed along the c-axis. If the magnetic field were set to some intermediate value where P and Q were comparable (~ 20 to 50 kG), one would expect to be able to see band structure effects due to the two dimensional lattice. Perfect crystals are unattainable, but it may be possible to grow crystals of sufficient lattice perfection to permit coherent coupling among fifty or so free-electron-like orbits at this moderate field. Coherence over this many orbits would give rise to observable band structure effects. If the field were then lowered, the radii of the coupled orbits in the lattice would increase, and fewer orbits would be contained within the coherence region defined by the degree of crystal perfection. A point would be reached where individual orbits would be effectively quantum mechanically decoupled by lattice scattering mechanisms. In this situation, the density of states would approach the δ function series (Fig. 9) appropriate for the completely decoupled system of orbits. If the field were lowered still further, a single orbit circumference would become longer than the coherence length. In that limit, all effects due to structure in the density of states for the network would begin to be washed out. The transition from a highly ordered quantum mechanical system to an almost completely disordered system is potentially within experimental control. Because the transition is controlled by the strength of the field, it

is a reversible process and, consequently, submits to convenient experimental investigation.

To summarize, the scale length for coherence is established by the degree of perfection of the underlying Mg crystal. The scale length of the two dimensional lattice (the coupled orbit system) can then be adjusted relative to this fixed coherence length. The effective "purity" of the two dimensional lattice becomes a tunable parameter.

These arguments can be made from a different point of view. From Fig. 9 it is clear that the characteristic width of the band gaps are under experimental control because $\hbar\omega_G$ is a function of the field. Each of the single particle states within a single band (a band such as one of those represented by boxes in Fig. 9) has an intrinsic width due to the finite lifetime imposed by the imperfect crystal. For a crystal of sufficient quality, the breadth of the single particle states would be comparable to the characteristic period of the density of states at some moderate value of the field. For this value of \vec{H} , some evidence of G orbits would be observable, but there would be no band structure effects. As \vec{H} is increased, the characteristic period of $\eta(\mathcal{E})$ will increase while the breadth of each single particle state will remain constant. At sufficiently high fields, the individual bands would be sufficiently broad to permit the breadth of the one-electron states to be neglected, and in this limit band structure effects would be clearly observable. A crystal of sufficient lattice perfection would permit the transition from short- to long-range coherence to occur for ranges of the field which are experimentally convenient and for which the breakdown probability P does not change very much.

Before this two dimensional "crystal" can be used for this or any other future purpose, it must be properly understood. An important first step was taken by Pippard in 1964 when, in a paper published in that year (Pippard 1964), he was able to derive a closed form for the band structure of the system. However, he stopped short of making predictions that were experimentally verifiable in a quantitative way. In 1966, in a second important paper on the subject (Falicov and Stachowiak 1966), Falicov and Stachowiak presented a theory which made clear quantitative predictions for dHvA experiments. (Both of these papers will be discussed in greater detail in a later section.) Since that time, there has not been a great deal of theoretical interest in the problem due to a lack of experimental evidence to either confirm or disprove this prevailing theory. Up to now, there has been no unequivocal experimental confirmation. The body of this dissertation will report experimental results which appear to be in qualitative disagreement with the predictions of Falicov and Stachowiak, and will suggest that there is reason for renewed interest in the development of a more complete theory.

The de Haas-van Alphen Effect

In this work the dHvA effect was used as a tool to study the coupled orbit network. This effect is well suited for the study of Fermi surface phenomena since the theory is well understood and generally applicable to Fermi surfaces of arbitrary shape. Specifically, the dHvA effect refers to quantum oscillations in the magnetization that are observed when a crystalline sample (usually a metal, but not

always) is placed in a changing magnetic field. The oscillations are a direct consequence of the quantization of conduction electron orbits and the sharp cutoff in the electron distribution at the Fermi energy \mathcal{E}_F . The following paragraphs will explain this phenomenon in more detail and will establish the most important features of the theory as much as possible within the framework of ideas presented in the previous section. For the sake of simplicity, the dHVA effect will be discussed in the absence of MB when the physics of each band sheet of the Fermi surface can be treated independently. The more general case is the subject of later sections.

The magnetization is given in terms of the system free energy f by the Maxwell relation

$$M = - \left(\frac{\partial f}{\partial H} \right)_T \quad (1.16)$$

and so the problem of calculating the dHVA effect becomes one of obtaining an expression for the free energy. The starting point for the standard theory (Lifshitz and Kosevich 1956) is the expression for the free energy of an electron gas

$$f = N\mathcal{E}_F + k_B T \sum_{\mathcal{E}} \ln [1 - f_0(\mathcal{E})] \quad (1.17)$$

where N is the number of conduction electrons per unit volume, k_B is Boltzmann's constant, and f_0 is the Fermi distribution function. The sum is over all energy. This expression is more conveniently stated in terms of a density of states

$$f = N\mathcal{E}_F + k_B T \iint n(\mathcal{E}) \ln [1 - f_0(\mathcal{E})] d\mathcal{E} dk_H \quad (1.18)$$

where $n(\mathcal{E})d\mathcal{E}dk_H$ is defined to be the number of states in energy interval $d\mathcal{E}$ for a slab of the Fermi surface of thickness dk_H (k_H is the component of k along the direction of applied field \vec{H}). This is the most straightforward partitioning of the problem, since in this scheme the slabs will be parallel to the orbital trajectories in \vec{k} space; there will be no field-induced transitions from slab to slab, so the physics of each can be computed separately.

The density of states for a single slab $n(\mathcal{E})dk_H$ is just the function that was introduced in Fig. 9. For a single band sheet of the Fermi surface and in the absence of broadening effects (MB or crystal imperfection), it will consist of a series of δ functions spaced by $\hbar\omega_c$. The essence of the dHvA phenomenon is contained in the fact that $\hbar\omega_c$ is field dependent and, consequently, as the field is increased, the spacing of the δ functions will increase, and they must necessarily move to higher energy. As each level moves through the Fermi surface, it will become depopulated by scattering processes, and it is just this periodic discontinuous depopulation of levels that is observed as the dHvA effect.

The period of depopulation can be related to the area of the particular slice through the Fermi surface. Suppose the field were adjusted so that the n^{th} Landau orbital were exactly at the Fermi surface at $T = 0^{\circ}\text{K}$. At this field, the enclosed area of the n^{th} orbit $A_n(k)$ will equal the cross sectional area of the Fermi surface $A_{\text{FS}_i}^{(k)}$ (the i indexes the i^{th} slice of the Fermi surface). Equation (1.9) can be solved for this value of the field

$$\frac{1}{H} = 2\pi \left(\frac{e}{\hbar c} \right) \frac{1}{A_{FS_i}^{(k)}} (n+\gamma) . \quad (1.19)$$

This equation can be interpreted to mean that a new, lower-lying level will appear at the Fermi surface each time the magnetic field is increased by an increment of $1/H$ given by

$$\Delta\left(\frac{1}{H}\right) = 2\pi \left(\frac{e}{\hbar c} \right) \frac{1}{A_{FS_i}^{(k)}} . \quad (1.20)$$

The corresponding frequency of the oscillations in H^{-1} due to the i^{th} slab of the Fermi surface is then

$$2\pi F_i = \left(\frac{\hbar c}{e} \right) A_{FS_i}^{(k)} . \quad (1.21)$$

This is a restatement of the Onsager rule (Eq. 1.9) and is often referred by that name.

The formal theory exploits this knowledge of the periodicity in \vec{H} by expanding the density of states for the slab in a fourier series of terms like $\cos(2\pi r \frac{F}{H})$, where F is the dHVA frequency for that slab and r is the series index spanning the positive integers. Using this expansion permits the effects of crystal broadening to be included in the theory directly. This is done by replacing the δ function series representation of the density of states with a series of Lorentzian functions of half width Γ related to the lifetime of the orbit by $\tau = \hbar/2\Gamma$. The harmonic expansion of these Lorentzians is accomplished with the aid of the Poisson summation formula

$$\sum_{n=-\infty}^{\infty} f(n) = \int_{-\infty}^{\infty} f(x) dx + 2 \sum_{r=1}^{\infty} \int_{-\infty}^{\infty} f(x) \cos 2\pi r x dx . \quad (1.22)$$

The detailed calculation is involved but well-documented (see, for example, Chambers 1966), and at length one obtains an expression for the oscillatory free energy in terms of the integral over k_H ;

$$f = \frac{\alpha^2 \hbar^2}{4\pi^4} \sum_{r=1}^{\infty} \frac{1}{r^2} \int \frac{I_r K_r}{m^*} \cos \left[r \frac{\hbar c}{e} \frac{A_{FS}^{(k)}}{H} - 2\pi r \gamma \right] dk_H . \quad (1.23)$$

In this expression, m^* is the effective mass of orbits in the slab and in the vicinity of the Fermi surface. It will be fixed for a given slab but is generally a function of k_H . The factor K_r is called the Dingle factor, and it is given by

$$K_r = \exp[-2\pi r (\Gamma/\hbar\omega_c)] \quad (1.24)$$

or alternatively, if the half width is expressed as an equivalent temperature T_D

$$K_r = \exp[-2\pi^2 r (m^* c k_B T_D / e \hbar H)] . \quad (1.25)$$

This factor is the result of the replacement of the δ functions by Lorentzians in the density of states for the slab. The factor I_r results from the integration over the Fermi distribution function and expresses the dependence of the oscillatory free energy upon the smearing of the Fermi surface at temperatures above $0^{\circ}K$. This factor is given by

$$I_r = \frac{X_r}{\sinh X_r} \quad (1.26)$$

where

$$\chi_{\mathbf{r}} = 2\pi^2 r \frac{m^* c k_{\mathbf{B}} T}{e \hbar H} . \quad (1.27)$$

Both $K_{\mathbf{r}}$ and $I_{\mathbf{r}}$ depend upon m^* and must be left inside the integral over $k_{\mathbf{H}}$.

One of the principal points to be emphasized in this section is the nature of this $k_{\mathbf{H}}$ integral. If a typical value for a Fermi surface cross-section is inserted into Eq. (1.21), the resulting frequency is on the order of 10^9 Gauss. This is, of course, much larger than anything obtainable in the laboratory. Thus, for all magnetic fields of experimental interest, the oscillatory argument of Eq. (1.23) will be very large and the cosine will oscillate very rapidly for small changes of $A_{\text{FS}}^{(k)}$. This means that the integral need only be evaluated in regions where $A_{\text{FS}}^{(k)}$ is an extremal (either a maximum or a minimum) cross-section. This is a very important result. It means that there will be no contribution to the oscillatory free energy, and hence to the magnetization, from any part of the Fermi surface other than at extremal cross-sections. It is for this reason that all of the discussion above that related to orbits on the midplane of the Fermi surface, is meaningful. These cross-sections are the extremal cross-sections and will be the only ones that contribute to the dHvA effect.

With these facts in hand, the $k_{\mathbf{H}}$ integral can be quickly evaluated. The three quantities $I_{\mathbf{r}}$, $K_{\mathbf{r}}$, and m^* are all very slowly varying over the vicinity of the extremal cross-section and so they may be taken out of the integral. Then, following Falicov and Stachowiak (1966), the cross-sectional area is expanded about its extremal value

$A_{\text{ext}}^{(k)}$

$$A_{\text{FS}}^{(k)} = A_{\text{ext}}^{(k)} + \frac{\partial A_{\text{FS}}^{(k)}}{\partial (k_H^2)} k_H^2 + \dots \quad (1.28)$$

From the definition of the effective mass (Eq. (1.11)), this may be rewritten

$$A_{\text{FS}}^{(k)} = A_{\text{ext}}^{(k)} - \pi \frac{m^*}{m_0} k_H^2 \quad (1.29)$$

where m_0 is the free electron mass. With this substitution, the k_H integral can be reduced to the standard Fresnel form (Cornu-Spiral integral) which is readily evaluated. The result is

$$f = - \sum_{r=1}^{\infty} \left(\frac{H^2}{2\pi F} \right) D(\vec{H}) \frac{I_r K_r}{r^{5/2}} \cos \left[2\pi r \frac{F}{H} + \beta_r \right] \quad (1.30)$$

where β_r is a constant phase shift that comes partially from the Fresnel integral and partially from the constant γ that appears in the Onsager relation (Eq. (1.9)). This constant is unimportant for the purposes of the present work but will be carried for the sake of completeness. The factor $D(H)$ is given by

$$D(\vec{H}) = - \left(\frac{e^2}{2\pi^2 m^* c^2} \right) \left(\frac{\hbar c}{e} \right) A_{\text{ext}}^{(k)} \left(\frac{2\pi e H}{\hbar c} \right)^{1/2} \left(2\pi \frac{m^*}{m_0} \right)^{-1/2} \quad (1.31)$$

or in terms of the dHvA frequency F corresponding to the extremal cross-section $A_{\text{ext}}^{(k)}$

$$D(\vec{H}) = -2\pi F \left(\frac{e^2}{2\pi^2 m^* c^2} \right) \left(\frac{e}{\hbar c} \right)^{1/2} H^{1/2} \left(\frac{m^*}{m_0} \right)^{-1/2} \quad (1.32)$$

The final step in obtaining the magnetization is simply to take the

derivative with respect to \vec{H} . All of the \vec{H} -dependent amplitude factors change very slowly over a single period of oscillation. It is customary to ignore these factors for the purposes of the derivative. The magnetization is thus given by

$$\vec{M} = 2\pi \left(\frac{e}{hc}\right)^{3/2} \vec{C}(\hat{H}) \sum_{r=1}^{\infty} \frac{rF}{r} \left(\frac{m^*}{m_0}\right)^{-1/2} K_r H^{-1/2} k_B T \left[\sinh \chi_r\right]^{-1} \sin\left[2\pi r \frac{F}{H} + \beta_r\right]. \quad (1.33)$$

The geometrical factor $\vec{C}(\hat{H})$ is, in general, a complex function of the orientation of \vec{H} with respect to the crystallographic axis of the sample. Discussion of this factor will be deferred until the section on experimental apparatus.

In Eq. (1.33) the sum over r is a left-over artifact of the expansion of the density of states in a fourier series, but it can be interpreted in a different way; the higher harmonic arguments in the sine function can be thought of as arising from multiple passages around the orbit. In this scheme an orbit which is traversed twice is considered distinct from the orbit traversed just once. For the double orbit, F is computed from the Onsager relation by counting the enclosed area twice. The effective mass for such a double orbit is interpreted similarly. From Eq. (1.15), the effective mass is shown to be related to the time of propagation around an orbit. If a double orbit is interpreted to be distinct from a single orbit, it will have exactly twice the propagation time and, hence, exactly twice the mass. With these reinterpretations of F and m^* , Eq. (1.33) becomes

$$\vec{M} = \sum_j \vec{A}_j(\vec{H}) \sin\left(\frac{2\pi F_j}{H} + \beta_j\right) \quad (1.34)$$

where

$$\vec{A}_j(\vec{H}) = \vec{C}(\hat{H}) \left(\frac{e}{\hbar c} \right)^{3/2} \frac{2\pi F_j}{\ell_j} m_j^{-1/2} K_j H^{-1/2} k_B T \left[\sinh X_j \right]^{-1} . \quad (1.35)$$

The sum is now over extremal orbits. The extra r in (1.33) has been carried as the harmonic index ℓ_j . The effective mass m_j is assumed to be in units of the free electron mass. These expressions form the basis for discussion of the dHvA effect in later sections.

Previous Investigations of the Coupled Orbit System

It would be difficult to interpret, or even to describe, the results of the present investigation into the coupled orbit problem without frequent reference to work that has been done in the past. In particular, the contributions that have been made by Pippard (1964) and by Falicov and Stachowiak (1966) are sufficiently pertinent to warrant specific review. Accordingly, these are discussed separately in the two subsections which follow.

Pippard's Model Band Structure

The starting point for Pippard's analysis is the wave function for an electron moving in a circular orbit in the presence of a magnetic field. When the gauge is chosen such that

$$\vec{A} = \frac{1}{2} \vec{H} \times \vec{r} \quad (1.36)$$

and the origin of coordinates is at the center of the orbit, this wave function is (Dingle 1952)

$$\psi = e^{i\ell\phi} \mathbf{r}^\ell e^{-\frac{1}{4}\alpha r^2} \quad (1.37)$$

where ℓ is the angular momentum quantum number and α is defined in Eq. (1.7). The maximum value of $\psi^*\psi$ occurs at $r'_0 = \left(\frac{2\ell}{\alpha}\right)^{1/2}$ which is close to the classical radius $r_c = [(2\ell+1)/\alpha]^{1/2}$ for an electron at energy $E = \hbar\omega_c(\ell+1/2)$. Near r_0 the wave function varies like $\exp[-\alpha(r-r_0)^2]$, and for large ℓ ($\sim 10^3$) the electron orbits in a circular track whose width is about 4% of the track radius.

For an electron orbit centered at location \vec{R} , the wave function is given by

$$\psi = e^{i\ell\phi} |\vec{r}-\vec{R}|^{-\ell} e^{-\frac{1}{2}\alpha|\vec{r}-\vec{R}|^2} \quad (1.38)$$

when the gauge is chosen as

$$\vec{A} = \frac{1}{2} \vec{H} \times (\vec{r}-\vec{R}) . \quad (1.39)$$

As long as the center of gauge is chosen at the center of the orbit in question, the quantum mechanical phase ϕ will evolve uniformly around the orbit. The problems arise with wave functions of electrons whose orbit centers are not coincident with the gauge center; the phase is found to evolve nonuniformly around the orbit in a manner which depends upon the choice of origin. Rather than disguise the inherent symmetry of the network, Pippard chose to compute the phase evolution around each orbit using the gauge centered on that orbit. The penalty imposed by this scheme is that each time an electron is Bragg reflected from one orbit to the next, the gauge is shifted from the old orbit center to the new orbit center. The effect of this gauge transformation is a phase shift δ' in the electron wave function which is assigned to the reflection junction in the manner illustrated in Fig. 10a. (The prime is used to distinguish phases from areas. The reason for this

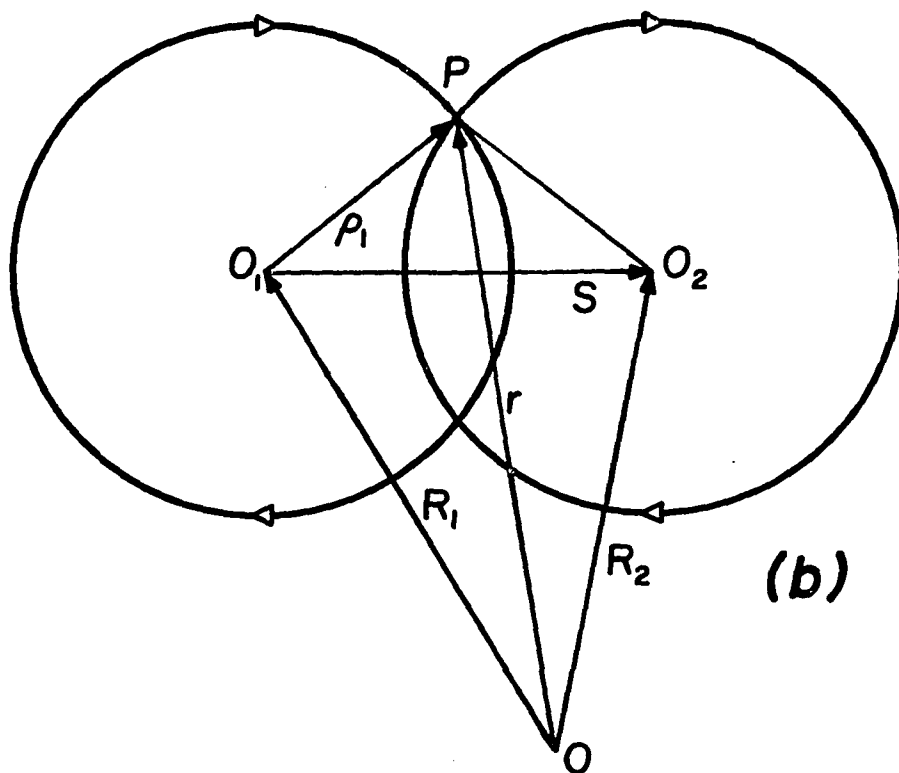
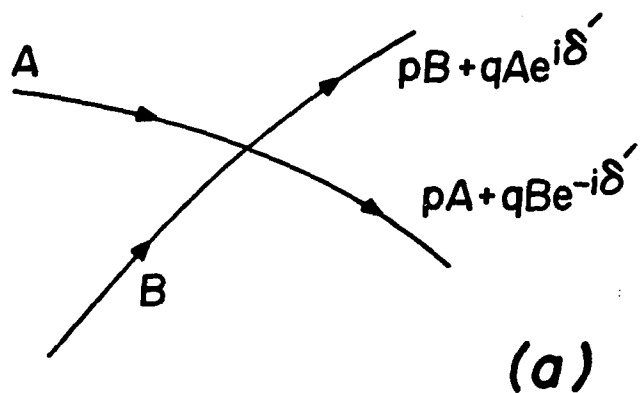


Fig. 10. The MB switching model: (a) amplitude and phase relationships at a junction, (b) the geometry of switching from orbit O_1 to orbit O_2 .

Both figures are from Pippard (1964).

convention will become more apparent below.) The electron of amplitude A that happens to tunnel the junction will emerge with amplitude pA . If the electron is reflected, the amplitude is phase shifted because of the necessity of switching gauge centers: the result is $qAe^{i\delta'}$. In general, p and q may be complex. Conservation of probability requires that they be related to one another and to P and Q , defined in the first section, by $p^*p+q^*q = P+Q = 1$. The phase shift δ' was found in terms of the vectors that define the shift in gauge

$$\delta' = \frac{1}{2} \vec{\alpha} \cdot (\vec{S} \times \vec{R}) \quad (1.40)$$

Vector $\vec{\alpha}$ is defined as in (1.7) with direction along \vec{H} . The vectors \vec{S} and \vec{R} are defined in Fig. 10b. By (1.40) δ' can be interpreted as α times the area of quadrilateral 00_1P0_2 ($\alpha A_{00_1P0_2}^{(r)}$ where the superscript refers to real space). This area can be further divided into an "internal" part $A_{0_1P0_2}^{(r)}$ that depends only upon the orbits involved and an "external" part $A_{0_100_2}^{(r)}$ that depends upon the choice of origin. In the special case where \vec{H} is chosen such that the area $A_{0_100_2}^{(r)}$ (equal to $\frac{1}{2} |\vec{S} \times \vec{R}_1|$ for \vec{R}_1 , in Fig. 10b) is an integral multiple of $2\pi/\alpha$, the external contribution to the phase shift vanishes. Indeed, \vec{H} can be chosen such that any polygon of orbit lattice (O-lattice) centers defines an integer $2\pi/\alpha$ area. For this benign choice of \vec{H} , the problem can be considered without further regard to the external part of the phase shift.

Pippard carefully examines the physical meaning of this dramatic reduction of the problem that occurs for special values of \vec{H} . The condition that O-lattice polygons have integer $2\pi/\alpha$ area is shown to

be sufficient to establish the orbit centers onto lattice sites of the underlying ionic crystal (I-lattice). Under these circumstances, all of the Bragg reflection junctions will also be fixed in their relationship to the I-lattice. Another way to say this is the phase of the fourier component of the lattice potential which is responsible for Bragg reflection at the network junctions is identical in the region of every junction. When I-lattice and O-lattice commensurability is lacking, this phase can be shifted from one junction to the next; and although the effect of this phase shift is thought to be small, it does ruin the rigorous translational invariance of the network. This issue of lattice commensurability will be brought up again later; for now we will follow Pippard and choose a value of \vec{H} for which the external part of the switching junction phase shift can be ignored. If the area $A_{0_1 P O_2}^{(r)}$ is relabeled δ as shown in Fig. 11, the associated switching phase shift is $\delta' = \alpha\delta$. Similarly, if the areas 2ξ and 2η are defined as shown in the figure, then the phase shift associated with a long segment propagation is $2\xi' = 2\xi\alpha$, and correspondingly, the phase shift associated with a short segment propagation is $2\eta' = 2\eta\alpha$.

The foregoing paragraphs have been concerned with a single switching event. These ideas can now be incorporated into a description of the electron on the entire network. The description begins by assigning a complex amplitude to the wave function at the center of each segment of a typical orbit (Fig. 12a). Because the network is assumed to be rigorously periodic, Bloch's Theorem may be invoked to require that the wave functions be invariant to within a phase factor

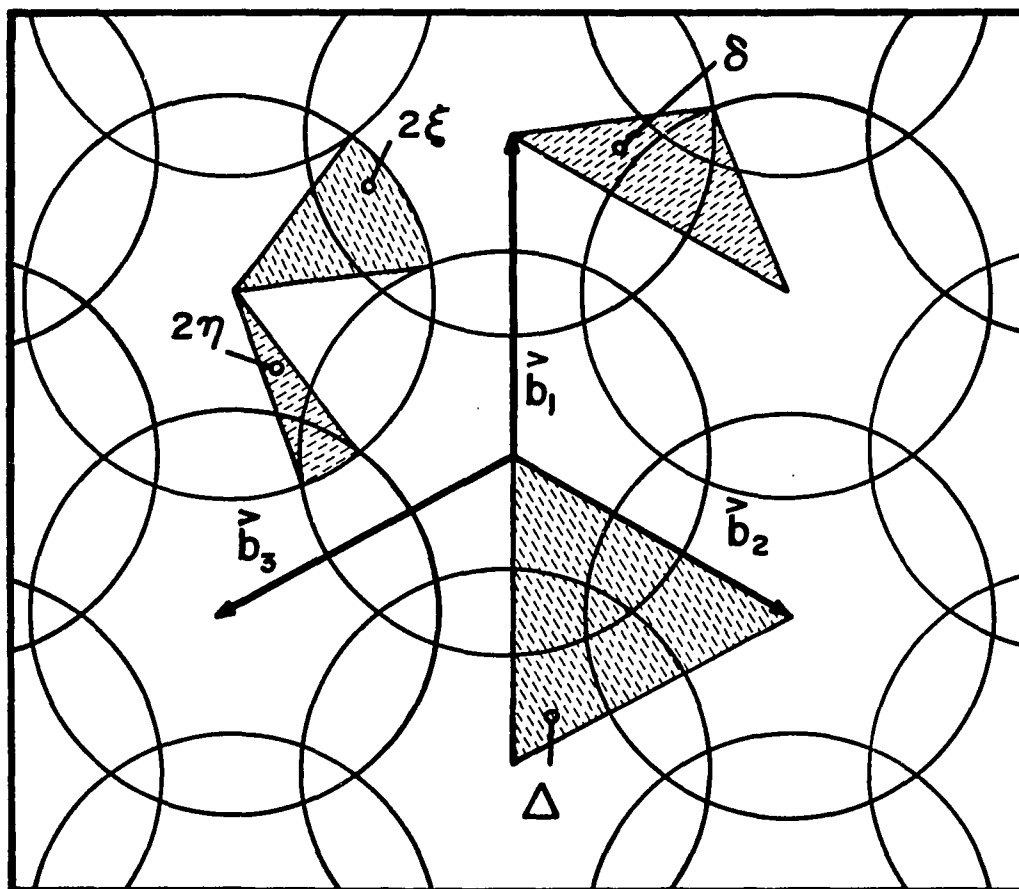


Fig. 11. The hexagonal network, showing areas 2ξ , 2η , δ , and Δ .

Also shown are the three \vec{r} space vectors \vec{b}_1 , \vec{b}_2 , and \vec{b}_3 that are used to define the network. The figure is taken from Pippard (1964).

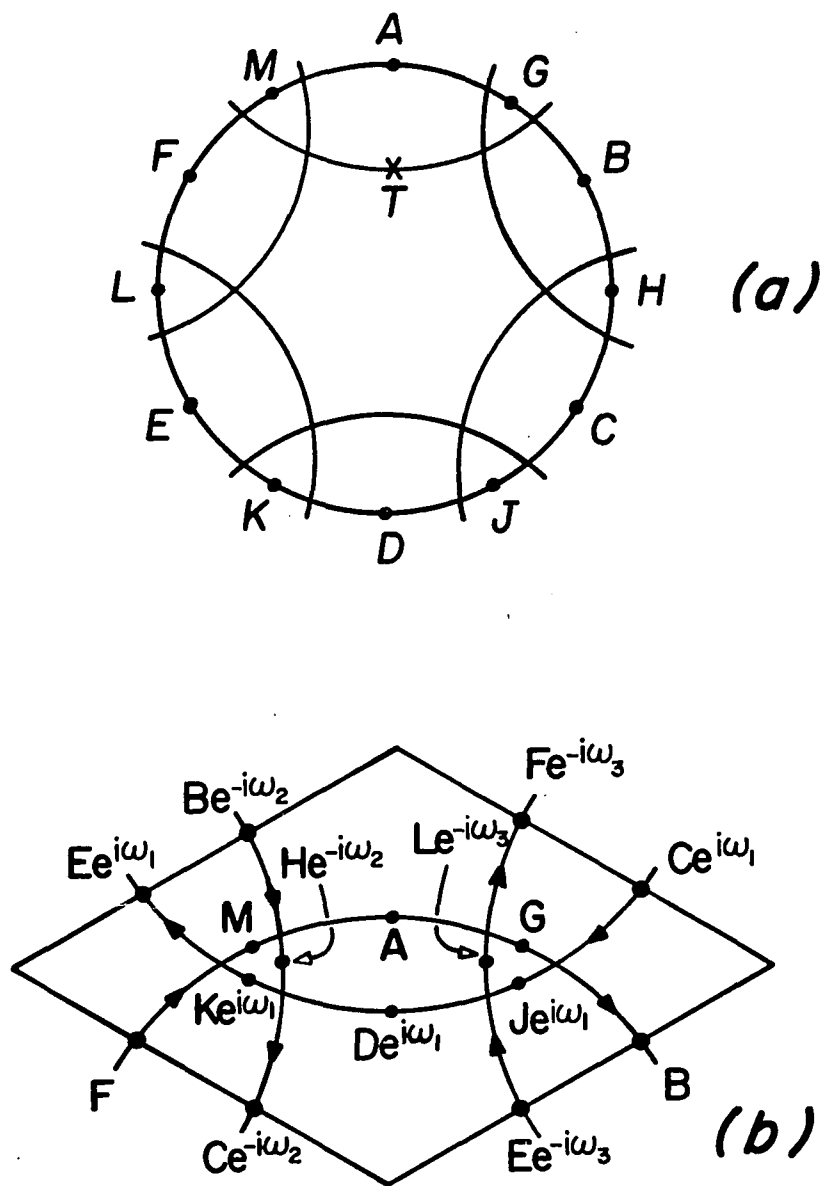


Fig. 12. Assumed amplitudes on the network: (a) around one orbit, (b) in the unit cell.

The phases assumed in (b) reflect the application of Bloch's theorem. Both figures are from Pippard (1964).

when translated through one of the vectors which define the lattice (any vector $n_1\vec{b}_1+n_2\vec{b}_2+n_3\vec{b}_3$ where \vec{b}_1, \vec{b}_2 and \vec{b}_3 are as shown in Fig. 11, and n_1, n_2 and n_3 are integers). For example, the wave function at point T (Fig. 12a) can be expressed in terms of the amplitude D by $De^{i\vec{k}\cdot\vec{b}_1}$. The factor $e^{i\vec{k}\cdot\vec{b}_1}$ is the Bloch component that expresses the delocalized nature of the electron state in a periodic system. As usual, the wave vector \vec{k} determines the energy associated with the additional degree of freedom available to the delocalized electron. With the aid of Bloch's Theorem, it is possible to translate the wave function amplitudes defined in Fig. 12a into a unit cell shown in Fig. 12b. The quantities ω_i are defined by $\omega_i \equiv \vec{b}_i \cdot \vec{k}$. This cell is identical to every other cell in the network. The problem has been reduced to a single set of coupled equations which expresses the relationships among the amplitudes within the cell. These relationships are determined by ξ' , η' , and δ' and are given by

$$\begin{aligned}
Ee^{i(\omega_1-\xi')} &= pKe^{i(\omega_1+\eta')} + qFe^{i(\xi'+\delta')} & , \\
He^{-i(\omega_2+\eta')} &= pBe^{-i(\omega_2-\xi')} + qMe^{i(\eta'+\delta')} & , \\
Ce^{-i(\omega_2+\xi')} &= pHe^{-i(\omega_2-\eta')} + qDe^{i(\omega_1+\xi'+\delta')} & , \\
Je^{i(\omega_1-\eta')} &= pCe^{i(\omega_1+\xi')} + qGe^{i(\eta'-\delta')} & , \\
Le^{-i(\omega_3+\eta')} &= pEe^{-i(\omega_3-\xi')} + qJe^{i(\omega_1+\eta'-\delta')} & , \\
Fe^{-i(\omega_3+\xi')} &= pLe^{-i(\omega_3-\eta')} + qAe^{i(\xi'+\delta')} & , \\
Me^{-i\eta'} &= qKe^{i(\omega_1+\eta'-\delta')} + pFe^{i\xi'} & , \\
Ae^{-i\xi'} &= qBe^{-i(\omega_2-\xi'-\delta')} + pMe^{i\eta'} & ,
\end{aligned} \tag{1.41}$$

$$\begin{aligned}
Ke^{i(\omega_1 - \eta')} &= qHe^{-i(\omega_2 - \eta' + \delta')} + pDe^{i(\omega_1 + \xi')} , \\
Be^{-i\xi'} &= qCe^{i(\omega_1 + \xi' + \delta')} + pGe^{i\eta'} , \\
De^{i(\omega_1 - \xi')} &= qEe^{-i(\omega_3 - \xi' - \delta')} + pJe^{i(\omega_1 + \eta')} , \\
Ge^{-i\eta'} &= qLe^{-i(\omega_3 - \eta' + \delta')} + pAe^{i\xi'} .
\end{aligned} \tag{1.41}$$

When the unknowns are eliminated from this system of equations, the result is found to be

$$\cos\omega_1 + \cos\omega_2 + \cos\omega_3 = \tag{1.42}$$

$$\frac{\sin 6(\xi' + \eta') - 2q^3 \sin 6(\xi' + \frac{1}{2}\delta') + q^6 \sin 6(\xi' - \eta' + \delta') - 3q^2(1 - q^2)^2 \sin 2(\xi' - \eta' + \delta')}{2q(1 - q^2)[q \sin 2(\xi' - \eta' + \delta') - \sin 2(\xi' + 2\eta' - \frac{1}{2}\delta')]}$$

The phases on the right hand side can be expressed in terms of the area Δ (Fig. 11) as well as the areas enclosed by the simple closed orbits G , H , γ , and A that were defined in the first section. These relationships are:

$$\begin{aligned}
6(\xi' + \eta') &= \frac{1}{2}\alpha A_G^{(r)} = \alpha \left(2\Delta + A_\gamma^{(r)} - \frac{1}{2}A_H^{(r)} \right) , \\
6(\xi' + \frac{1}{2}\delta') &= \alpha \left(3\Delta - \frac{1}{2}A_H^{(r)} \right) , \\
6(\xi' - \eta' + \delta') &= \alpha \left(4\Delta - A_\gamma^{(r)} - \frac{1}{2}A_H^{(r)} \right) , \\
2(\xi' - \eta' + \delta') &= \alpha \left(\frac{4}{3}\Delta - \frac{1}{3}A_\gamma^{(r)} - \frac{1}{6}A_H^{(r)} \right) , \\
2(\xi' + 2\eta' - \frac{1}{2}\delta') &= \alpha A_A^{(r)} .
\end{aligned} \tag{1.43}$$

The meaning of Eq. (1.42) becomes more apparent if the phases on the right hand side are expressed in terms of energy. In the analysis that follows, the necessary relationships are derived in a manner different from that given by Pippard. The reason for doing this will be discussed later.

The relationship between area and energy of the free-electron-like orbit G is established without difficulty. Because the dHvA effect is sensitive only to electron orbits in the vicinity of the Fermi surface, it is appropriate to expand the energy dependence of the orbit area about its value at the Fermi energy:

$$A_G^{(r)}(\mathcal{E}) = A_G^{(r)}(\mathcal{E}_F) + \frac{\partial A_G^{(r)}}{\partial \mathcal{E}}(\mathcal{E}-\mathcal{E}_F) + \dots \quad (1.44)$$

or if the zero of energy is chosen such that $\mathcal{E}_F=0$ then

$$A_G^{(r)}(\mathcal{E}) = A_G^{(r)}(0) + \frac{\partial A_G^{(r)}}{\partial \mathcal{E}} \mathcal{E}. \quad (1.45)$$

From the definition of the effective mass (Eq. 1.11)

$$\frac{\partial A_G^{(r)}}{\partial \mathcal{E}} = \frac{2\pi}{\alpha} \frac{m_G^*}{\hbar^2}. \quad (1.46)$$

Combining (1.45) and (1.46) and multiplying by α yields

$$\alpha A_G^{(r)}(\mathcal{E}) = \frac{A_G^{(k)}(0)}{\alpha} + \frac{2\pi c m_G^*}{e \hbar} \mathcal{E} \quad (1.47)$$

where $A_G^{(r)}(0)$ has been replaced by the \vec{k} space equivalent $A_G^{(k)}(0)/\alpha^2$. An expression like this one can be produced for each area $A_A^{(r)}$, $A_Y^{(r)}$, and $A_H^{(r)}$ involving the effective masses m_A^* , m_Y^* , and m_H^* , and these masses can then be expressed in terms of the free-electron-like mass M_G^* . The area enclosed by the free-electron-like orbit G can be expressed in terms of areas ξ and η

$$A_G^{(r)} = 12(\xi+\eta) = 12(1+\gamma_p)\eta, \quad (1.48)$$

where the parameter $\gamma_p \equiv \xi/\eta$ has been introduced. Rearranging (1.48)

yields

$$\begin{aligned}\eta &= \frac{1}{12} \frac{1}{1+\gamma_p} A_G^{(r)} , \\ \xi &= \frac{1}{12} \frac{\gamma_p}{1+\gamma_p} A_G^{(r)} ,\end{aligned}\tag{1.49}$$

from which it can be concluded that

$$\frac{\partial \eta}{\partial \mathcal{E}} = \frac{1}{12} \frac{\gamma_p}{1+\gamma_p} \frac{\partial A_G^{(r)}}{\partial \mathcal{E}} = \frac{1}{12} \frac{2\pi c m_G^*}{\alpha e \hbar} = \frac{1}{2\alpha} \frac{x}{\mathcal{E}} ,\tag{1.50}$$

where

$$x \equiv \frac{2\pi c m_G^*}{6(1+\gamma_p) e \hbar} \frac{\mathcal{E}}{H}\tag{1.51}$$

is Pippard's dimensionless energy variable. Similarly, it is found that

$$\frac{\partial \xi}{\partial \mathcal{E}} = \frac{\gamma_p}{2\alpha} \frac{x}{\mathcal{E}} .\tag{1.52}$$

The effective mass of γ can be written in terms of $\partial \eta / \partial \mathcal{E}$:

$$m_\gamma^* = \frac{\hbar^2}{2\pi} \frac{\partial A_\gamma^{(k)}}{\partial \mathcal{E}} = \frac{\alpha^2 \hbar^2}{2\pi} 6 \frac{\partial \eta}{\partial \mathcal{E}} = 3\alpha \frac{\hbar^2}{2\pi} \frac{x}{\mathcal{E}} .\tag{1.53}$$

This result can be used in the expression for the energy dependence of

$$\alpha A_\gamma^{(r)}(\mathcal{E}) = \frac{A_\gamma^{(k)}(0)}{\alpha} + 3x .\tag{1.54}$$

Similarly, for $A_H^{(r)}$ and $A_A^{(r)}$:

$$\begin{aligned}\alpha A_H^{(r)} &= \frac{A_H^{(k)}(0)}{\alpha} - 6\gamma_p x , \\ \alpha A_A^{(r)} &= \frac{A_A^{(k)}(0)}{\alpha} + 2(\gamma_p + 2)x .\end{aligned}\tag{1.55}$$

Using (1.43) these results may be included in (1.42) to yield

$$C(\vec{\kappa}) = \frac{\sin[\phi_1^0 + 3(\gamma_p + 1)x] - 2q^3 \sin[\phi_2^0 + 3\gamma_p x] + q^6 \sin[\phi_3^0 + 3(\gamma_p - 1)x] - 3q^2(1-q^2)^2 \sin[\phi_4^0 + (\gamma_p - 1)x]}{2q(1-q^2) \{q \sin[\phi_4^0 + (\gamma_p - 1)x] - \sin[\phi_5^0 + (\gamma_p + 2)x]\}} \quad (1.56)$$

where

$$\begin{aligned} \phi_1^0 &= \frac{1}{\alpha} \left(2\Delta^{(k)} + A_Y^{(k)}(o) - \frac{1}{2} A_H^{(k)}(o) \right) , \\ \phi_2^0 &= \frac{1}{\alpha} \left(3\Delta^{(k)} - \frac{1}{2} A_H^{(k)}(o) \right) , \\ \phi_3^0 &= \frac{1}{\alpha} \left(4\Delta^{(k)} - A_Y^{(k)}(o) - \frac{1}{2} A_H^{(k)}(o) \right) , \\ \phi_4^0 &= \frac{1}{\alpha} \left(\frac{4}{3} \Delta^{(k)} - \frac{1}{3} A_Y^{(k)}(o) - \frac{1}{6} A_H^{(k)}(o) \right) , \\ \phi_5^0 &= \frac{1}{\alpha} \left(\frac{1}{2} A_A^{(k)}(o) \right) , \end{aligned} \quad (1.57)$$

and $C(\vec{\kappa})$ is defined

$$C(\vec{\kappa}) \equiv \cos\omega_1 + \cos\omega_2 + \cos\omega_3 . \quad (1.58)$$

Since the variable $C(\vec{\kappa})$ is defined in terms of the wave vector $\vec{\kappa}$, and x is a function of the energy, Eq. (1.56) can be seen to define the band structure $\mathcal{E}_\rho(\vec{\kappa})$ of the coupled orbit system. Despite the compactness of this function, unusual for a band structure, it resists easy comparison with experiment without recourse to a large digital computer. One can, however, make some qualitative statements under the condition of fixed \vec{H} . If \vec{H} is constant, then the terms ϕ_i^0 amount to constant phase factors in the sine arguments, and these can be dropped without material effect. The result is

$$C(\vec{k}) = \frac{\sin[3(\gamma_p+1)x] - 2q^3 \sin[3\gamma_p x] + q^6 \sin[3(\gamma_p-1)x] - 3q^2(1-q^2)^2 \sin[(\gamma_p-1)x]}{2q(1-q^2) \{q \sin[(\gamma_p-1)x] - \sin[(\gamma_p+2)x]\}} \quad (1.59)$$

This is identically Pippard's result. The terms ϕ_i^0 were never displayed explicitly in Pippard's presentation and were only referred to briefly as constants that had been dropped. The present argument has proceeded differently from that of Pippard in order to display these terms and to be able to point out that, although they may be dropped when H is constant, they must certainly be retained when discussing experiments which involve a changing field. In particular, this is true of dHVA experiments. Of course, it must also be true that a changing magnetic field necessarily reintroduces the question of lattice commensurability. Both of these issues will be discussed in more detail in Chapter 4, but for now we will go ahead and drop the H dependent ϕ_i^0 terms and examine the form of the band structure.

Pippard showed that the range of allowed values of \vec{k} lies within the Brillouin zone corresponding to the O-lattice and that the number of \vec{k} states within that zone correctly corresponds to the degeneracy of the Landau levels. In other words, the number of allowed \vec{k} states within the O-lattice Brillouin zone is correctly interpreted as the number of states in a single band. Furthermore, since \vec{k} has been completely isolated on the left hand side of (1.59), the contours of constant $C(\vec{k})$ in \vec{k} space are also contours of constant energy. These contours are shown inside the O-lattice Brillouin zone in Fig. 13 and

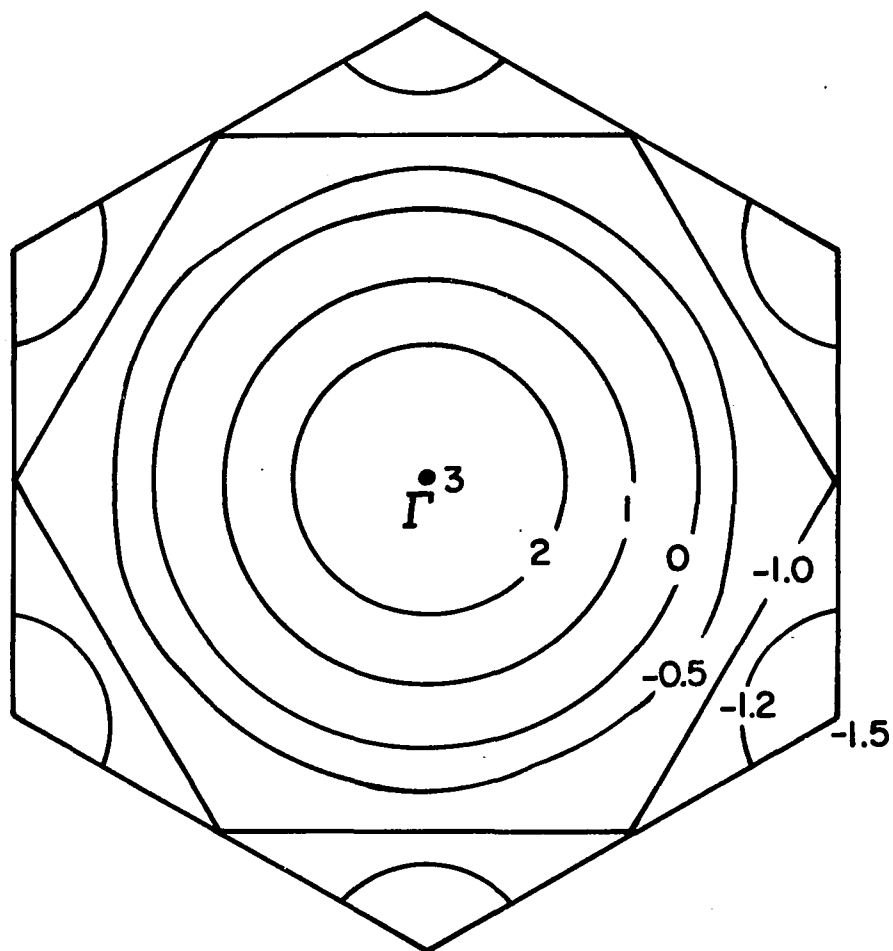


Fig. 13. The O-lattice Brillouin zone, showing contours of constant $C(\vec{k})$.

The figure is from Pippard (1964).

are the same as in the hexagonal tight binding calculation. Note that $C(\vec{\kappa})$ only takes on values between 3 and -1.5 within the zone. These values of $C(\vec{\kappa})$ define the region within a given band. A map of the entire band structure can be generated quite simply with a digital computer by calculating the right hand side of (1.59) for every point on a rectangular grid of points (q_i, x_i) . If the result of the calculation for a given (q_i, x_i) pair is between 3 and -1.5, then the point is within a band; otherwise it is not. The parameter q ranges from 0 to 1, while x is typically allowed to range over one repetition period of the band structure. This period is a function of parameter γ_p ; for $\gamma_p = 31/5$ (the appropriate value for magnesium) the repetition period is $\Delta x = 10\pi$.

Figure 14 shows a computer generated display of 1/6 of repetition period of the band structure given by Eq. (1.59) for $\gamma_p = 31/5$. A number of points about this figure are worthy of emphasis. The region near $Q = 0$ shows exactly the behavior that was anticipated in Fig. 8; the levels are sharp and spaced by $\hbar\omega_G$ in energy. These levels correspond to the free-electron-like G orbit that dominates the lattice at low q . When q approaches 1, the levels again narrow down, but on this side two distinct periodicities are evident. The long period is 14.4 times the period for G while the short period is 1.16 times as long. These ratios verify the discrete levels on the right to be the triangular γ and the hexagonal H orbits since $m_G^*/m_\gamma^* = 2(\gamma_p + 1) = 14.4$ and $m_G^*/m_H^* = (\gamma_p + 1)/\gamma_p = 1.16$ ($\gamma_p = 31/5$). This is the behavior expected since γ and H are the only allowed orbits on the network when $q = 1$. Finally, in the intermediate region of q , the figure clearly indicates that the local band broadening is profoundly influenced by the relative positions

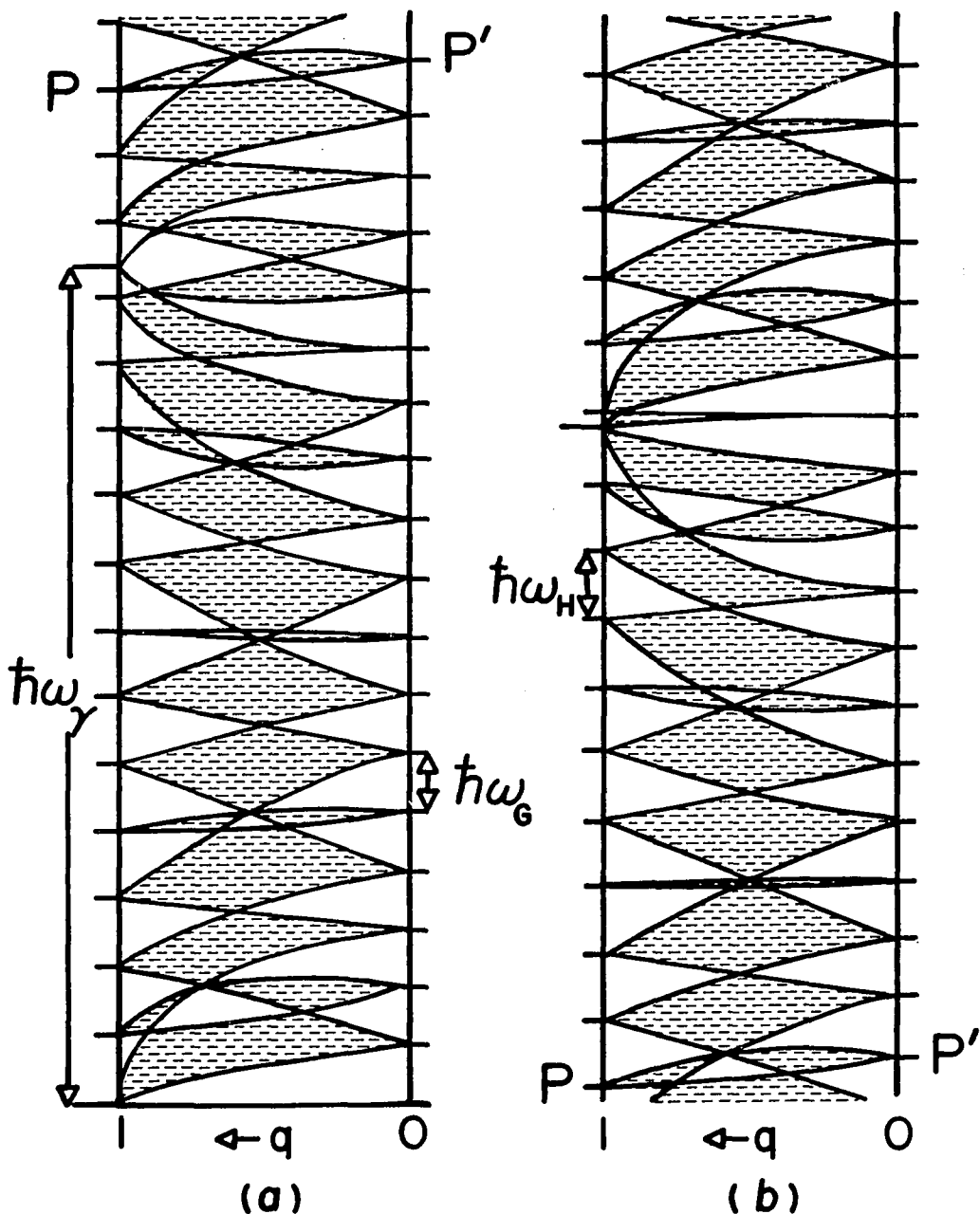


Fig. 14. Energy band structure for hexagonal network $\gamma_p = 31/5$.

Section (b) is a continuation of (a). Points P and P' are common to both to show how they run together. The sharp levels on the right are spaced by $\hbar\omega_G$ in energy and correspond to the G orbit. The entire pattern repeats every 216 G levels.

of the H and γ levels on one side and the G levels on the other. Any shifting of these relative positions could be expected to radically change the band structure in a given local region (for example, in the region of the Fermi energy). The terms ϕ_i^0 that were dropped in obtaining (1.59) will produce just this shearing effect on the levels whenever \vec{H} is varied. The effect of these "forgotten" terms will be a principal focus of attention in the data interpretation discussions of Chapter 4.

The Predictions of Falicov and Stachowiak

Falicov and Stachowiak (1966) analyze the coupled orbit problem differently from Pippard. They take a Green's function approach and begin by showing that the Green's function solution to the time dependent Schroedinger equation

$$i\hbar \frac{\partial G(\vec{r}, \vec{r}_0, t)}{\partial t} = H_{co} G(\vec{r}, \vec{r}_0, t) \quad (1.60)$$

(where H_{co} is the coupled orbit system Hamiltonian), which is subject to the initial condition

$$G(\vec{r}, \vec{r}_0, 0) = \delta(\vec{r} - \vec{r}_0) , \quad (1.61)$$

can be related to the system density of states by

$$\eta(\mathcal{E}) = \frac{1}{2\pi\hbar} \iint G(\vec{r}_0, \vec{r}_0, t) \exp[i\mathcal{E}t/\hbar] d\vec{r}_0 dt . \quad (1.62)$$

Falicov and Stachowiak (FS) point out that these equations are important both because they reformulate the problem into a quest for the correct Green's functions and because they are susceptible of physical

interpretation which provides considerable guidance for making the right choices. The wave packet $G(\vec{r}, \vec{r}_0, 0)$, which is initially ($t = 0$) ideally localized at some point \vec{r}_0 in the network, will spread throughout the network as time evolves (in the negative as well as positive direction) in the manner described by $G(\vec{r}, \vec{r}_0, t)$. Since the Green's function appears in Eq. (1.62) only as a trace over \vec{r}_0 , it can be concluded that the only contributions to $\eta(\mathcal{E})$ from the δ function initially at \vec{r}_0 will come from those parts of the spreading wave packet that remain at \vec{r}_0 or which leave and then return to \vec{r}_0 after some interval of time. This interpretation forms the basis of their theory.

In order to carry the analysis to the point of making specific predictions for dHvA experiments, FS make some simplifying approximations. If the z axis is defined to be along \vec{H} , the problem can be reduced to two dimensions by discarding $G(\vec{r}, \vec{r}_0, t)$ in favor of a two-dimensional version which will be written $G_{k_H}(\vec{r}, \vec{r}_0, t)$ but which is really only a function of x, y, x_0, y_0 , and t with k_H as a parameter. This Green's function can be used in a two-dimensional density of states $\eta(\mathcal{E}, k_H)$. This in turn is related to the total density of states by

$$\eta(\mathcal{E}) = \frac{1}{2\pi} \int \eta(\mathcal{E}, k_H) dk_H, \quad (1.63)$$

where the integral over k_H can be evaluated by the same Cornu Spiral substitution used to evaluate (1.23) in the previous section. The arguments applied in that context can be restated once again here to show that the only contribution to the oscillatory part of $\eta(\mathcal{E})$ will come from the G_{k_H} corresponding to an extremal section of the Fermi surface.

and whose amplitude and phase evolution are well defined on the network. In particular, they chose the wave packets developed by Pippard which were discussed in the previous section. This superposition permits FS to follow their own prescription and focus attention upon those parts of the spreading Green's function which return to \vec{r}_0 after some time interval. They write

$$G_{k_H}(\vec{r}_0, \vec{r}_0, t) = \sum_j Y_j e^{i\phi_j} \delta(t-t_j). \quad (1.64)$$

The sum is over all wave packets initially at \vec{r}_0 which return at some later time t_j with amplitude Y_j and phase ϕ_j . All of the closed orbits of the type shown in Fig. 15 will be included in this sum, as well as infinitely many others. In the formulation of FS, the return amplitude of a given wave packet will be diminished by the path dependent factor

$$R_j = (ip)^{n_{1j}} q^{n_{2j}}. \quad (1.65)$$

The exponents n_{1j} and n_{2j} count the number of broken down and the number of Bragg reflected junctions on a path j . The complex i expresses the fact that FS follow the convention established by Pippard (1962, 1964), who showed that the complex numbers p and q must differ in phase by $\pi/2$ and, in the absence of any detailed knowledge of their absolute values, assigned q to be real and p to be pure imaginary. Displaying this magnetic breakdown damping factor explicitly, FS write the Green's function as

$$G_{k_H}(\vec{r}_0, \vec{r}_0, t) = \frac{2m_0}{\hbar} \sum_j \frac{6m_j}{D_j \ell_j} K_j R_j e^{i\phi_j} \delta(t-t_j). \quad (1.66)$$

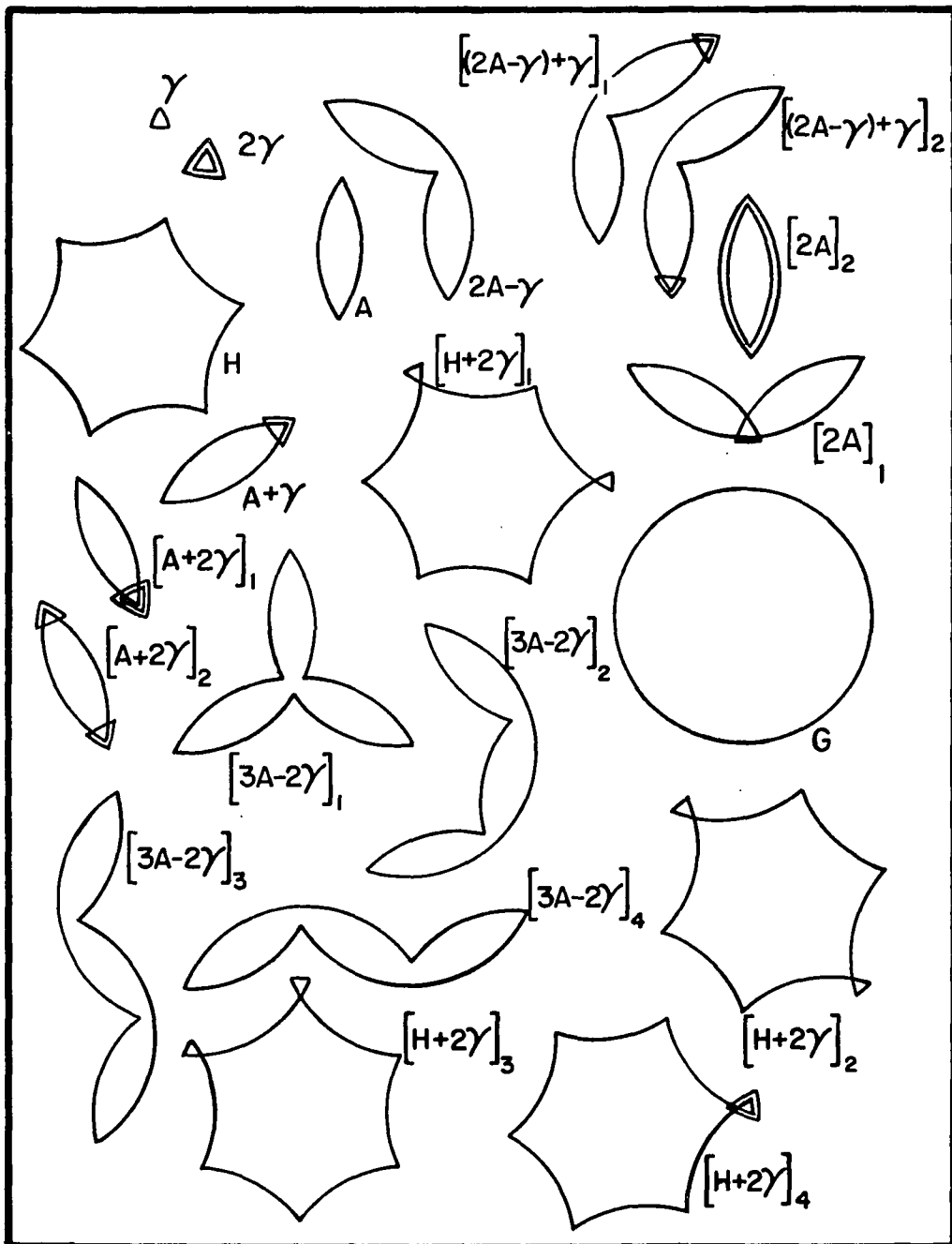


Fig. 15. Selected simple closed orbit trajectories.

Note that two orbits that enclose the same area can be quite dissimilar. A good example of this is the pair of orbits labeled $[2A]_1$, and $[2A]_2$.

The factor K_j is the Dingle factor defined in (1.24) or (1.25). The factor $6m_j/D_j \ell_j$ is a weighting factor which counts the amplitude contribution of all equivalent packets j . It is broken down into the effective mass of the fundamental orbit (m_j/ℓ_j) and the number of congruent, non-identical orbits that contribute to j , ($6/D_j$). The factor D_j is the rotational symmetry of the orbit. (For example, the A orbit has twofold rotational symmetry, and there are three congruent, nonidentical orientations of this orbit.) For a few selected orbits, the numerical factors of the MB term $(6m_j/D_j \ell_j)R_j$ are listed in Table I.

With the Green's function in hand, the density of states is obtained from the integrals in (1.62) and (1.63), and then the free energy is obtained from that result by further integration over energy in the manner described by Eq. (1.18). After these calculations have been performed, one obtains

$$f = \frac{2m_0}{\pi^2} \sum_j \frac{6}{D_j} (ip)^{n_{ij} n_{2j}} \frac{m_j^{-3/2}}{\ell_j} \left(\frac{eH}{\hbar c} \right)^{1/2} \left(\frac{eH}{2\pi m_0 c} \right)^2 K_j I_j \cos \left(\frac{2\pi F_j}{H} + \beta_j \right). \quad (1.68)$$

All the quantities which appear in this expression have been defined above or in the previous section. In their original paper, FS do not go beyond (1.68), but it is a simple matter to take the derivative with respect to H and arrive at a magnetization expression which can be compared directly with experiment. If all of the H dependence in the amplitude is ignored (as was done in the derivation of Eq. (1.33)), the magnetization is found to be

$$\vec{M} = \sum_j \vec{A}_j(\vec{H}) \sin \left(\frac{2\pi F_j}{H} + \beta_j \right), \quad (1.69)$$

TABLE 1. Symmetry properties of a few selected orbits.

Orbit Type	n_{1j}	n_{2j}	l_j	D_j
γ	0	3	1	3
2γ	0	6	2	3
A	4	2	1	2
A+ γ	4	5	1	1
[A+2 γ] ₁	4	8	1	1
[A+2 γ] ₂	4	8	1	2
[2A- γ]	6	3	1	1
[2A] ₁	8	4	1	1
[2A] ₂	8	4	2	2
[(2A- γ)+ γ] ₁	6	6	1	1
[(2A- γ)+ γ] ₂	6	6	1	1
[3A-2 γ] ₁	6	6	1	3
[3A-2 γ] ₂	8	4	1	1
[3A-2 γ] ₃	8	4	1	2
[3A-2 γ] ₄	8	4	1	2
H	0	6	1	6
[H+2 γ] ₁	4	8	1	1
[H+2 γ] ₂	4	8	1	2
[H+2 γ] ₃	4	8	1	1
[H+2 γ] ₄	2	10	1	1
G	12	0	1	6

where

$$\vec{A}_j(\vec{H}) = \vec{C}(\hat{H}) \left(\frac{e}{\hbar c} \right)^{3/2} \frac{6}{D_j} (ip)^{n_{1j} n_{2j}} \frac{2\pi F_j}{\ell_j} m_j^{-1/2} K_j H^{-1/2} k_B T [\sinh x_j]^{-1}, \quad (1.70)$$

and this is exactly (1.24) and (1.35) except for the MB factor. (The temperature-dependent factor I_j has been written out explicitly so that (1.70) may be more easily compared with (1.35).) The H dependence of these amplitudes is given by $[6m_j^{-3/2}/D_j \ell_j] (ip)^{n_{1j} n_{2j}} H^{1/2} F_j I_j$. A few of these have been calculated for selected orbits and are shown in Fig. 16. Note that the masses used to calculate these curves are those appropriate for Mg, the breakdown field H_0 was taken to be 5.8 kG (Eq. (1.5)), the Dingle lifetime was assumed to be infinite ($K_j = 1$), and the temperature was chosen to be 0.3°K.

Figure 16 will be very useful in making the comparison between theory and experiment, and so it is worthwhile to discuss some of its features. First of all, the G orbit dominates in the high field limit while the γ orbit is largest at low fields. This is the result anticipated by the discussions of the previous sections. The amplitude of the hexagonal orbit H is not shown because it never gets large enough to be included in the figure. (It is severely attenuated above 10 kG by the q^6 factor. At lower fields it is held down by a relatively large effective mass.) Another feature of Fig. 16 is that the more complex of two similar orbits usually has the lower amplitude. For example, 2G is never larger than G, 2A never larger than A, A+ γ never larger than A, etc. The orbits 2 γ and 2 γ +A are exceptions to this rule at fields above 13 kG.

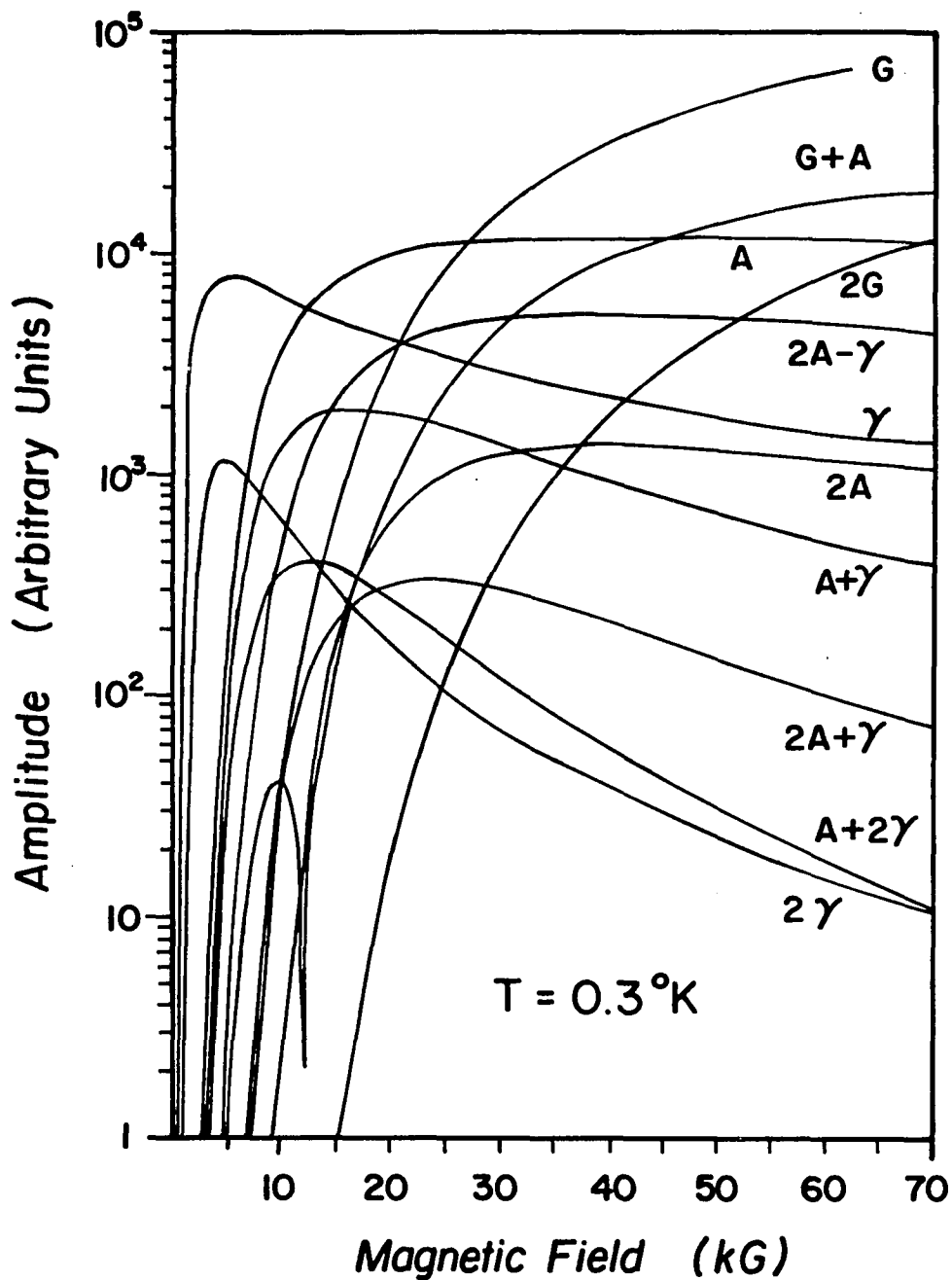


Fig. 16. The predicted magnetic field dependence of the amplitude of the oscillatory magnetization for a few selected simple closed orbits.

The parameters are chosen to be suitable for Mg. The lifetime τ is assumed to be infinite.

Perhaps the most surprising feature is the cusp that occurs in the curve labeled 2A. This amplitude corresponds to the sum of the individual contributions of the four orbits labeled $[2A]_1$, $[2A]_2$, $[(2A-\gamma)+\gamma]_1$, and $[(2A-\gamma)+\gamma]_2$ of Fig. 15. The amplitudes of all of these orbits are appropriately considered together as a single term for two reasons. First, each of these orbits encloses the same area in \vec{k} space and will, therefore, produce the same dHvA frequency (by the Onsager relation (1.21)). Second, each orbit is composed of an equal number of long and short path segments. The propagation time around the four orbits will be identical, and this implies equal effective masses (by Eq. (1.15)). The first two of these orbits involve eight tunnelings and four reflections each; the last two have six and six. As a consequence, the $(ip)^{n_{ij}}$ factor contributes a relative minus sign between the two amplitudes. The cusp occurs because the amplitudes cross in the vicinity of 12 kG, so the difference goes to zero. A final important point that can be made about Fig. 16 concerns what it does not show. There are no dHvA frequencies corresponding to $A-\gamma$, $A-2\gamma$, $G-A$, $G-\gamma$, etc. Simple closed orbits that enclose these areas are forbidden because they all require the wave packet to traverse at least one path segment in the reverse direction.

The predictions inherent in Fig. 16 can be summarized qualitatively by the schematic dHvA spectrum shown in Fig. 17. This spectrum represents what we might expect to see at 0.3°K and at moderate field (~ 30 kG). The γ frequency spike is the lowest, followed by 2γ (much smaller), A , $A+\gamma$, and on up to $3G-2A$ which is the highest frequency shown (note that the frequency scale is logarithmic). The spectrum can

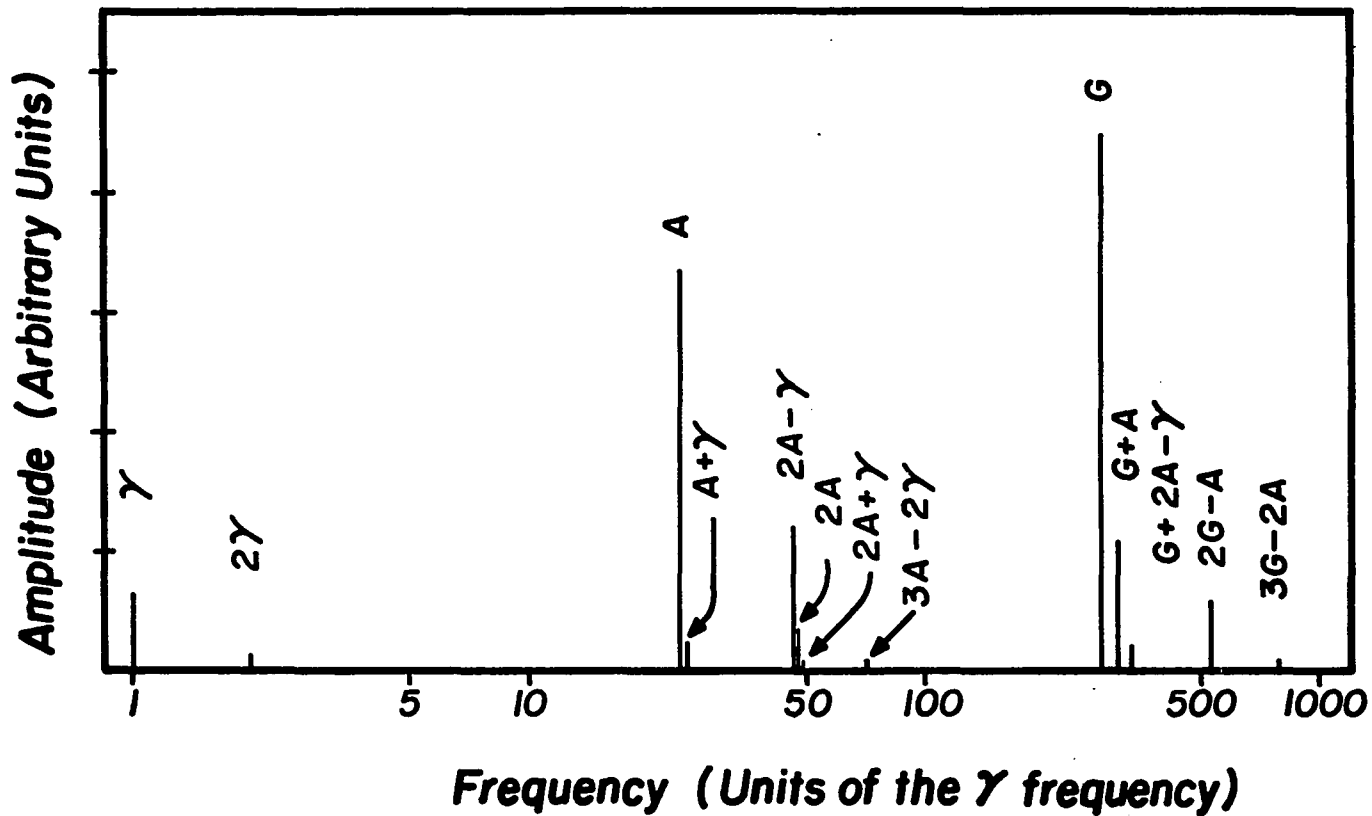


Fig. 17. Qualitative representation of a typical spectrum predicted by Fig. 16.

This spectrum corresponds to a field of approximately 30 kG. The horizontal scale is logarithmic. The relative amplitudes are approximate.

be thought of as consisting of three distinct series. The γ series consists of γ and 2γ that are shown; higher harmonics of this orbit would not be expected to be visible. Among the peaks that could be expected to be visible in the A series are A, $A+\gamma$, $2A-\gamma$, $2A$, $2A+\gamma$, and $3A-2\gamma$. The G series consists of G, $G+A$, $2G-A$, $2G$, $2G+A$, and $3G-2A$ that would be expected to be seen. One would certainly expect to see no frequencies immediately below either A or G. Such a peak would have to be a very high harmonic or the lower series and would be expected to have a very small relative amplitude. The basic structure of this spectrum will not change with higher temperature or with crystal imperfections. Both of these effects will tend to attenuate the higher frequencies relative to the lower but will introduce no new peaks immediately below A or G.

Figures 16 and 17 have been presented here so that they may serve as a reference for comparison when the results of the present experiment are discussed in Chapter 3. In that discussion, the dHvA data will be shown to differ qualitatively from the form predicted by these figures.

CHAPTER 2

EXPERIMENTAL TECHNIQUE

The discussion of experimental details divides naturally into three broad areas: the growth and handling of the magnesium crystal, the research cryostat, and the detection and processing electronics. These subjects are discussed in order in this chapter.

The Crystal and the Crystal Mount

The Mg single crystal used in this study was grown by the vapor sublimation technique developed by R. W. Stark. This method is well understood and routinely produces Mg crystals whose impurity concentration is well below .01 ppm (Reifenberger 1977). Having crystal purity thus under control, particular attention was given in this experiment to the prevention of lattice imperfections due to strain and dislocations. The consideration of strain determined both the choice of crystal and the mounting technique.

Crystal choice is an important part of the vapor sublimation growth technique. After a run, one is never left with just one single crystal. The growth region of the crucible is always a riotous jumble of crystals of many shapes, sizes, and orientations. In the past, the crystals chosen from this mass have tended to be large with well-defined and unblemished faces. Such a crystal normally yields many samples, each of which can be cut to convenient size and shape with a

string saw. Unfortunately, the larger crystals are more likely to have grown in close proximity to a neighbor or as part of a complex of adjacent crystals. These will invariably be oriented arbitrarily with respect to one another, and because of the anisotropy of the thermal expansion coefficients such crystals will experience forces during the cool-down phase of the sublimation. This will be true regardless of how slowly this is done. These forces can strain the crystals.

Attention to strain prompted us to change the normal strategy. Rather than search for a large crystal from which a sample of any shape could be cut, we looked instead for a small crystal grown in isolation on a whisker, and resolved to live with whatever shape it might have.

At length we were able to find one which was quite nice. It had a (0001) face with three characteristic 120° angles. The face was approximately 2 mm by 2 mm, and behind it the crystal had a 1 cm long taper to a narrow attachment point on another chunk of Mg. The arrangement was very convenient for low risk handling. Ultimately, the whisker had to be removed prior to preparation for mounting, but until that time the crystal was never touched. The whisker was severed by patient, repeated application of 5% HCL solution applied locally in very small droplets and with the aid of a microscope. No additional shaping was done. Removing the whisker left a crystal about $2\frac{1}{2}$ mm long. It is likely that the compact geometry of the crystal was critical for strain immunity during the handling processes which were then to begin.

Minimization of strain also determined the manner in which the sample was mounted in the sample holder. Rather than wedge or seal the irregularly shaped crystal into a cavity of complementary shape, we chose instead to use a solder mount on the (0001) face as the only point of contact. Our strategy was to avoid the unknown and uncontrolled risk of strain whenever the crystal was thermally cycled, and to accept instead the unquestionable risk of strain during the soldering process. In so doing we were going with our strength, relying on the expertise the group has developed from years of experience soldering electrical leads to delicate magnetoresistance samples. It is appropriate to mention, at this point, that this strategy appears to have worked. The dHvA signal ultimately obtained from the crystal was quite large and could be followed to quite high frequencies. We noticed no degradation in signal after numerous thermal cyclings of the sample.

The following is a brief description of the soldering procedure. The crystal was first etched in a 1% HCL solution and then placed on a copper plate with the mounting face uppermost. A 4 mil copper foil mask was placed on top of the sample so that a 3/64 in. diameter hole in the foil exposed the middle of the Mg surface. This assembly was placed in an rf sputtering apparatus. First, a reverse bias was applied to remove the oxide coating from the Mg, and then a 30,000 Å thick copper spot was sputtered onto the exposed surface. After the sample was removed from the sputtering apparatus, it was placed on a warming plate and held there with a piece of soft modeling clay. The copper spot was then tinned using Indalloy #8 solder with flux #5, both products of the Indium Corporation of America. Thermal

shock to the sample was held to a minimum by prewarming the crystal to a temperature somewhat below the 93°C melting point of the solder. After tinning, the warming plate and crystal were brought up close beneath the mounting post with a lab jack. The final joint was made under a microscope with a small hot wire.

After the clay residue was cleaned off with xylene, a machined epoxy cylinder with an outer diameter of .167 inches was fastened over the crystal with a copper nut on the mounting post. This assembly is shown in cross section in Fig. 18. Once this sleeve was in place, handling risk to the sample was essentially over since the crystal was completely protected except for a small X-ray window. Subsequent handling, described below, involved manipulations of the mounting post only.

The final step in the mounting procedure was orientation. This was made easy by the fact that the epoxy sleeve was designed to press fit gently into a back reflection X-ray camera as well as into the pickup coil assembly in the sample holder of the cryostat. After standard X-ray crystallography had established the orientation of the crystal in the camera, it was carefully removed and inserted into the pickup coil. A mirror glued to the mounting post was used as an optical lever to reestablish the correct alignment after the transfer. Alignment was important because the sample holder had only one rotational degree of freedom. The c-axis of the Mg crystal had to be made to lie in this plane of motion so that it could later be lined up along the magnetic field after the cryostat was fully assembled.

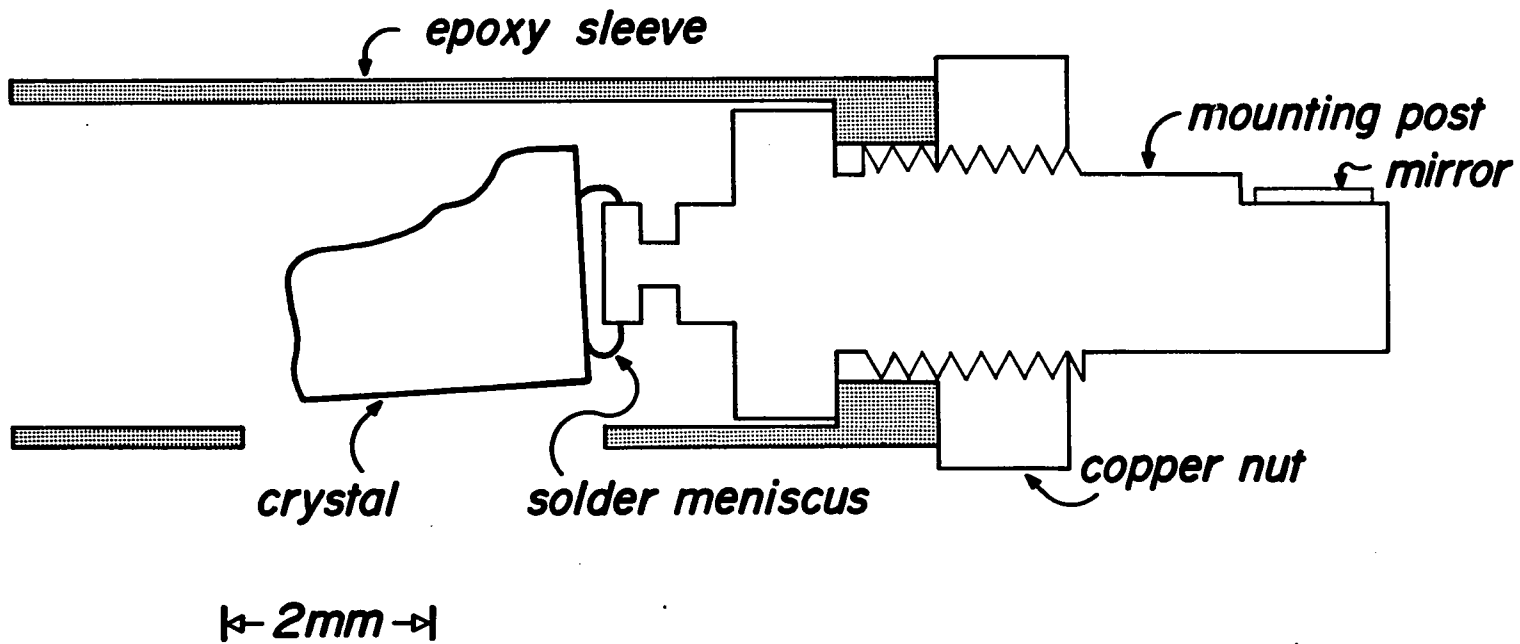


Fig. 18. Cross-section of the crystal mounting assembly.

The Cryostat

The dHvA effect is intimately involved with the expansion of magnetic-field-dependent Landau levels through the Fermi surface. This is conveniently detectable only when the kT width of the Fermi surface is smaller than the energy separation of the levels, and as a consequence, dHvA experiments are performed at low temperatures and high magnetic fields. In the case of this investigation, these demands were met by a $\text{He}^3\text{-He}^4$ dilution refrigerator and a superconducting magnet integrated into a cryogenic system which is capable of lowering the sample temperature to $.040^\circ\text{K}$ in the presence of a 50 kG magnetic field. This system is shown schematically in Fig. 19. In the paragraphs below, I will first describe the system geometry and then discuss the how and the why of its use.

To begin with, the main He^4 bath is held in the inner of two concentric stainless steel buckets labeled a and d in the figure. These are separated by a single vacuum space containing two heavy gauge copper heat shields labeled b and c. The outer copper shield is held at 77°K by a liquid nitrogen jacket above the helium bucket. The inner shield is held at 20°K by thoroughly heat exchanging the cold escaping helium gas on its way out of the cryostat. Each of the cylinders b, c, and d are wrapped with approximately 20 turns of aluminized mylar. Together, this configuration provides adequate thermal isolation of the He^4 bath from room temperature. The helium boiloff rate is level dependent, but we have found it to be as low as two liters per day when the liquid level was low in the bucket.

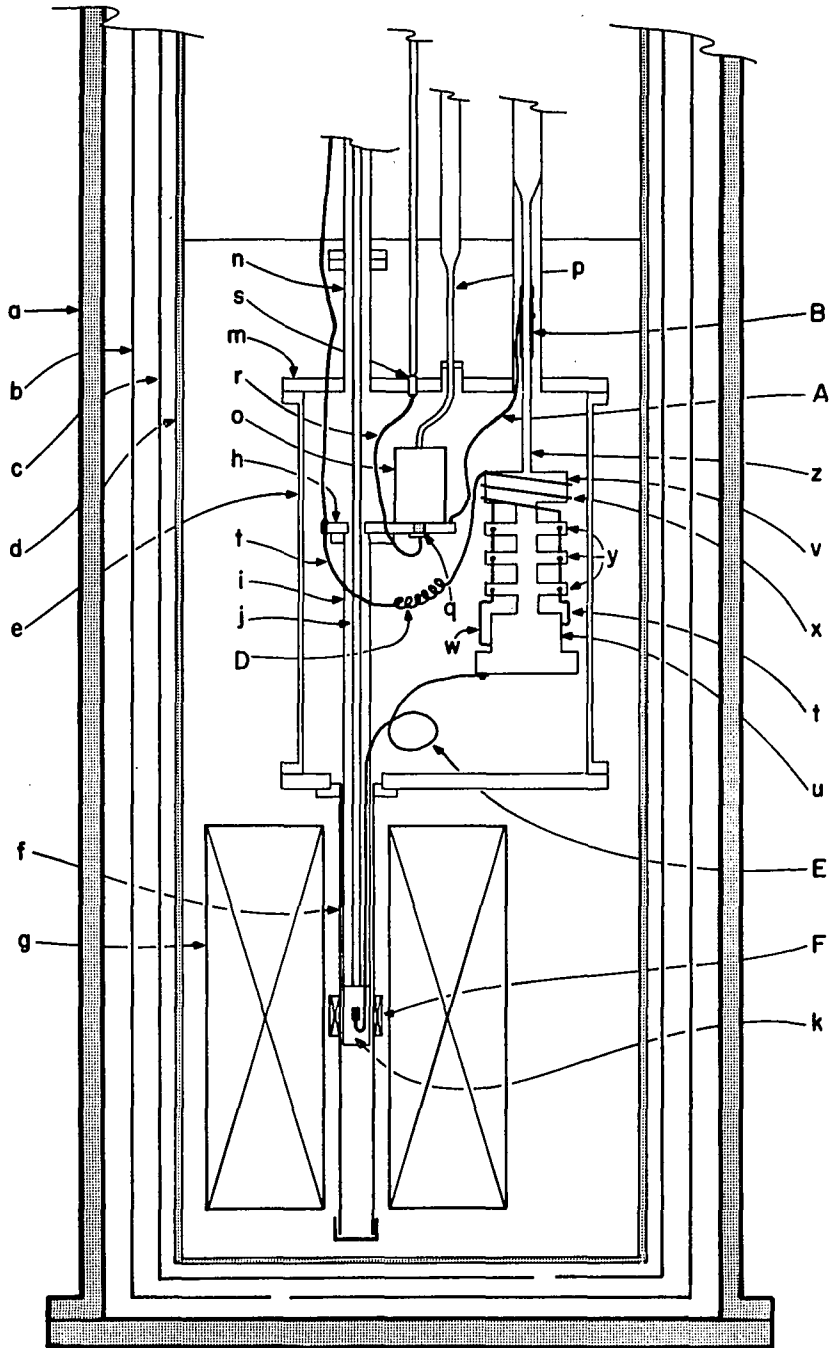


Fig. 19. The He³-He⁴ dilution refrigerator cryostat.

Turning now to the inside of the helium bucket, there is another smaller sealed copper cylinder (e) which is normally totally immersed in the helium and which provides the vacuum confinement necessary to shield the lowest temperature portions of the system from the "hot" bath. This cylinder has a stainless steel tail (f) at the bottom which extends the vacuum into the bore of the solenoidal superconducting magnet (g) suspended below. Inside the can a copper heat sink plate (h) is hung from the top flange (m) by three thin-wall stainless steel standoffs (not shown), and it is from this plate that the rotating sample holder (k) is itself extended into the tail. A 10-in. long, 3/4-in. o.d., thin-wall stainless steel tube (i) holds the sample in the magnetic field and provides thermal isolation from the heat sink plate. Inside this tube the drive shaft (j) for the rotating sample holder extends up into the vacuum can and then out of flange m on its way to a rotating o-ring seal held at room temperature at the very top of the cryostat (not shown). The drive shaft is isolated from the helium space by a vacuum-tight stainless steel sleeve (n) which extends from the flange to the seal.

Sharing space with all of these other items in the inner vacuum are the dilution refrigerator and an initial precool refrigerator which we call the Syphon. Physically, the Syphon is a 2-in. high, thick-wall copper can (o) that is soldered to the heat sink plate. There is a pumping port at the top from which a 1/8-in., thin-wall stainless steel tube (p) extends up and through flange m before widening to 3/8 in. on the way out of the cryostat. At the bottom of the

Syphon is a sintered copper plug (q), and from this plug a .010-in. capillary tube (r) extends back up to a needle valve (s) on the flange. A metered flow of helium can be syphoned from the main bath, through the capillary and into the small can. Once there, it is vigorously pumped out of the cryostat. The flash evaporation of liquid helium at the sintered copper plug produces cooling from two processes simultaneously: the vaporization of the liquid and the free expansion of the gas. We found that this strategy worked well to produce efficient cooling power inside the vacuum can.

The Syphon is typically run at 1.4°K , and the low-temperature heat sink thus provided is crucial to the operation of the refrigerator. Essentially, the refrigerator consists of two chambers that must be part of a closed He^3 pumping cycle, much of which is necessarily at room temperature. He^3 is pumped out of the evaporation chamber (v) and then compressed externally by a diffusion pump and a mechanical pump. It is then passed back into the cryostat where it flows down into the vacuum can, through a pressure-reducing flow impedance (D), and into the mixing chamber (u). This flow would quickly short the refrigerator to 4°K if these lines were not heat sunk to the lower temperature Syphon. The He^3 capillary (t) connects to a sintered copper plug attached to the Syphon. The 1.4°K plug not only further cools the He^3 gas but also liquifies it. The He^3 pumpout line (z) is thin-wall stainless steel with a short piece of copper tubing as an insert (B), and this is clamped at 1.4°K by a heavy copper wire (A) bolted to the plate.

Although they are not shown in the figure, there are also many electrical leads for thermometers, heaters, and the dHvA signal, which must also attach to the refrigerator. All of these are thoroughly heat sunk to plate h first.

It is important to note that careful control of heat flow does not stop at the heat sink plate but is a major factor in the structure of the refrigerator itself. When operating in the dilution refrigeration mode, the system must be able to sustain a temperature gradient between the evaporation chamber and the mixing chamber. The evaporation chamber typically runs at about 0.7°K while the mixing chamber can be well below 0.1°K . This gradient must be maintained in spite of the fact of a flow of He^3 between the two chambers. It is for this reason that the He^3 input capillary (t), which carries pure He^3 to the mixing chamber, is carefully heat exchanged with capillary w, which communicates the He^3 - He^4 dilute phase back up to the evaporation chamber. This occurs in a continuous, double-wall capillary heat exchanger (x), as well as in three copper-block step heat exchangers (y).

One final aspect of the refrigeration system is important, and that is the manner in which the mixing chamber is thermally coupled to the sample. The problem is made relatively simple by the fact that we have a mounting post soldered to the crystal, and, indeed, this is an important reason why this technique has been used. The thermal link (E) consists of a thick bundle of fine copper wires bolted to the mixing chamber on one end and soldered to a short .060-in. diameter indium wire on the other end. The indium wire is then soldered to the mirror

end of the mounting post with enough slack to allow sample rotation. The bundle of wires is designed to promote thermal contact between the refrigerator and the sample without allowing electrical contact. Thermal contact is mediated by Stycast epoxy which is used to bind the wires into the 10-in. bundle. Half the wires extend from one end of the epoxy matrix while the rest of the wires extend from the other end. Since there is no electrical contact among the wires, the refrigerator is electrically insulated from the sample.

Although there was no thermometer on the sample, the dHVA signal behavior reflected the temperatures indicated by the thermometer on the mixing chamber. The thermal link appeared to function at temperatures as low as 0.3°K . It is not clear at this time how well the link will behave at temperatures below 0.1°K .

The structure of this system was determined in large part by the demands of the dilution refrigerator, and so it is appropriate to include at least a brief discussion of how it works. For a more detailed description, the reader is directed to books by White (1968) or Lounasmaa (1974) and to the extensive lists of references those books contain.

Fundamentally, the process of dilution refrigeration depends upon the peculiarities of the solubility of He^3 in He^4 at extremely low temperatures. When the refrigerator is at operating temperature (below 0.8°K), a phase separation occurs in the mixing chamber, and this results in a He^3 liquid layer floating on top of another layer which is mostly He^4 but which contains some dissolved He^3 . The amount

of He^3 allowed in the lower phase is temperature dependent but remains in the vicinity of 6 to 8% for dilution refrigeration temperatures (Edwards et al. 1965). The He^4 in this phase is superfluid and essentially in its quantum mechanical ground state. The He^3 in solution is supported by the inert He^4 as if in a vacuum. The cooling occurs when He^3 dissolves across the phase interface. A rigorous treatment of this phenomenon is rather involved (see for example, Lounasmaa 1974), but for the purposes of this writing it is sufficient to note that the process is analogous to a "vaporization" of the He^3 at the interface. The refrigerator is made to run in a continuous cycle by conducting the dilute liquid to the evaporation chamber where the He^3 is preferentially driven off by heating with a resistance wire heater to approximately 0.7°K . The resulting concentration gradient causes transport of He^3 from the mixing chamber to the evaporation chamber, and He^3 will then continuously "vaporize" through the phase interface to replace that which is pumped out of the evaporator. The cycle is made complete when the He^3 that is pumped out is recompressed outside the cryostat and then returned to the He^3 liquid layer in the mixing chamber.

This refrigerator has attained temperatures as low as $.04^\circ\text{K}$ when operated in this manner, but at this point it should be said that the refrigerator was not used in the dilution refrigeration mode during the course of this particular experiment. An unfortunate accident resulted in the loss of an unknown amount of He^3 , and because obtaining lowest temperatures was not important to this study, we have not yet

reestablished the correct $\text{He}^3\text{-He}^4$ ratio to put the mixing layer where it belongs in the mixing chamber.

For this system it is a very simple matter to convert from dilution refrigeration to He^3 evaporation refrigeration. This is accomplished by simply turning off the resistance wire heater on the evaporation chamber, causing the temperature of that chamber to fall to the level appropriate to the vapor pressure sustainable by the external pumping system. In this mode the source of cooling is not the mixing chamber but rather the evaporation chamber, and so the He^3 flow must be counted on to bring the two chambers into thermal equilibrium. Although operating the system this way reduces its refrigeration power, it did produce temperatures as low as 0.29°K .

A few points about the operation of this system are worthy of mention. Unlike many cryostats, this one can remain in continuous use at any of its operating temperatures. This is true because the Syphon can remain in continuous operation. Ordinarily, the auxiliary cooling power needed to operate the refrigerator is supplied by pumping on a helium pot in the vacuum space. This reservoir will run dry eventually however large it is made. When it does run dry helium will have to be retransferred, and this will warm the reservoir to 4.2°K and thereby interrupt the operation of the refrigerator. With the Syphon system, we found that after a little practice the needle valve could be adjusted to the correct flow rate and then left completely alone for days at a time. Left in dynamic equilibrium this way, the Syphon required only that the main helium reservoir outside the vacuum be maintained

above the needle valve. This was found to be no problem since retransferring additional helium into the main bath had no influence at all upon the temperature of the Syphon or the refrigerator.

A second advantage of the Syphon is its small size. An enclosed helium pot will tend to be rather large to prevent frequent refilling. A large helium pot requires a large vacuum confinement, and this poses additional problems for the total system design. The Syphon relaxes that requirement. In this system we were able to cut the vacuum can in half (literally) when the Syphon was put in to replace the helium pot.

A second feature of this system is that it is easy to control once it has reached operating temperatures, but rather tricky during cool-down. Most of the skill required of the operator is involved with this initial phase. The problem arises because the refrigerator is not self-cooling until it has reached temperatures below 4.2°K when helium can be condensed into its chambers. Getting to 4.2°K is not as easy as one might at first suppose, since the same precautions that isolate the system from heat leaks tend to insulate against precooling mechanisms just as well. Because of this, the cool-down must be carried out in a number of specific steps taken in a well-defined sequence. The first of these begins even before any helium or nitrogen is transferred into the cryostat, since one cannot simply go ahead and fill the helium space and wait for the contents of the vacuum can to come to 4°K . The can is an adiabatic confinement; such a plan would take weeks. Rather than wait this long, the vacuum is broken with hydrogen gas so

that the refrigerator and sample systems are put into thermal contact with the copper walls. The walls are then cooled slowly by repeated short bursts of helium transferred with long intervening pauses. The inner systems must be allowed time to follow the walls down in temperature to about 15°K when the hydrogen vapor pressure in the can starts to go rapidly toward zero. Caution must be exercised to avoid ending up with a hot refrigerator hanging in a good vacuum with all of the hydrogen prematurely frozen out in the tail at the bottom of the cryostat. Once the hydrogen freezes out, the helium bucket can be transferred full of helium, immersing the vacuum can.

The cooling process is picked up at this stage by the Syphon. Although the heat sink plate is necessarily thermally isolated from the refrigerator itself, it is connected to the copper tubing in the He^3 pumpout line (B). This tubing is isolated from the refrigerator and from the bath by thin-wall stainless steel and so can be held at about 1.4°K even when the refrigerator is at 15°K . Simply filling this pump line with He^4 gas will cause the cold copper tube to begin cooling the refrigerator. The gas condenses in the copper tube and runs down into the hot evaporation chamber where it evaporates once more and flows back up. This refluxing cycle quickly cools the top of the refrigerator to less than 4°K . Once this has been accomplished, valves are opened outside the cryostat and He^4 is allowed to flow down the He^3 input capillary. This capillary is heat sunk to the evaporation chamber, and the flow of liquid spreads the lower temperatures to the rest of the refrigerator. In an hour or so the appropriate charge

of He^4 will have condensed into the refrigerator and the process can then be repeated with the He^3 . Once He^3 starts to condense, the system can be made to function as a He^3 evaporation refrigerator and the precooling process is complete.

The Electronics

The phenomenon studied in this experiment was the dhvA effect. The experimental problem was, therefore, the detection and interpretation of magnetization oscillations as a function of dc magnetic field. In broad terms, discussion of the experimental apparatus can be organized along these lines. First, there is a detection system designed to produce voltage analogs to the sample's quantum magnetization and to the magnetic field. Second, interpretation takes over when these analogs are presented to the data processing system on two input channels. Accordingly, in the following, I will first discuss the detection system, consisting of the analog electronics and the pickup coil, and then discuss separately the data processing system, consisting of the digital electronics and software.

The Detection System

In this experiment the magnetization oscillations were detected using the Large Amplitude Modulation Field technique of Stark and Windmiller (1968). In this method the sample is placed in a magnetic field given by

$$\vec{H} = \vec{H}_0 + \vec{h}\cos\omega t \quad (2.1)$$

where \vec{H}_0 is the magnetic field produced by the superconducting solenoid

and \vec{h} is the amplitude of a superimposed modulation field. The time dependence in \vec{H} produces a time dependence in the magnetization $\vec{M}(\vec{H})$, which can be displayed by writing $\vec{M}(t)$. The time rate of change of $\vec{M}(t)$ is sensed as a voltage induced in a pickup coil wound closely around the sample (Schoenberg and Stiles 1964). The pickup coil used for this experiment was wound on a cylindrical epoxy coil former which was .425 in. long with inner and outer diameters of .167 in. and .250 in. Three coil sections were machined into the epoxy. The central section was wound with 1000 turns of #52 gauge wire while the flanking sections were counterwound with 500 turns each. The fully wound coil was placed in a spatially-homogeneous, oscillating, magnetic field and trimmed with additional turns of wire until it was made to have less inductive pickup than a single turn. The coil was bucked this way to eliminate direct coupling between the large dc field \vec{H}_0 and the pickup coil (Stark and Windmiller 1968). If this coupling is not eliminated, any vibration of the sample holder will produce large emfs in the pickup coil which are unrelated to the magnetization of the sample. This noise will reflect the acoustic vibration spectrum of the system and will mask the signal. The three-in-line geometry was used so that magnetization related voltages induced in the central coil would not be bucked out. In this arrangement, the central coil is coupled closely to the sample while the flanking coils are not.

The modulation field was produced by a small field coil (labeled F in Fig. 19) wound on the stainless steel tail and held in the bore of the main magnet.

The modulation coil and the pickup coil are shown in relationship to the rest of the detection system in Fig. 20. This system is designed to take advantage of the effects of large amplitude modulation (amplitude greater than or equal to a period of oscillation in $\vec{M}(\vec{H})$) on the induced signal in the pickup coil. These effects were first understood by Stark and Windmiller (1968), and what follows is a brief summary of their explanation.

From Eq. (1.34) it is clear that the expression for the magnetization due to the i th sheet of the Fermi surface is

$$\vec{M}_i(H, \theta, \phi) = \vec{A}_i(H, \theta, \phi) \sin \left(\frac{2\pi F_i(\theta, \phi)}{H} + \beta_i \right). \quad (2.2)$$

The time dependence of H , given by Eq. (2.1), may be rewritten as

$$H = H_0 \left(1 + \frac{h}{H_0} \cos \omega t \right) \quad (2.3)$$

where the vector nature of \vec{H}_0 and \vec{h} has been dropped since \vec{H}_0 and \vec{h} are always parallel in this experiment. In Mg, $\vec{A}_i(H, \theta, \phi)$ is a much more slowly varying function of H than is $\sin(2\pi F_i/H)$ for all frequencies F_i and for all field strengths of experimental interest. We can therefore ignore the time dependence of \vec{A}_i , and to a very good approximation, the time dependent magnetization can be written

$$\vec{M}_i(t) = \vec{A}_i \sin \left(\frac{2\pi F_i}{H_0 \left(1 + \frac{h}{H_0} \cos \omega t \right)} + \beta_i \right). \quad (2.4)$$

For modulation amplitudes used in this experiment $h/H_0 \ll 10^{-2}$ and so this becomes

$$\vec{M}_i(t) = \vec{A}_i \sin \left(\frac{2\pi F_i}{H_0} - X_i \cos \omega t + \beta_i \right) \quad (2.5)$$

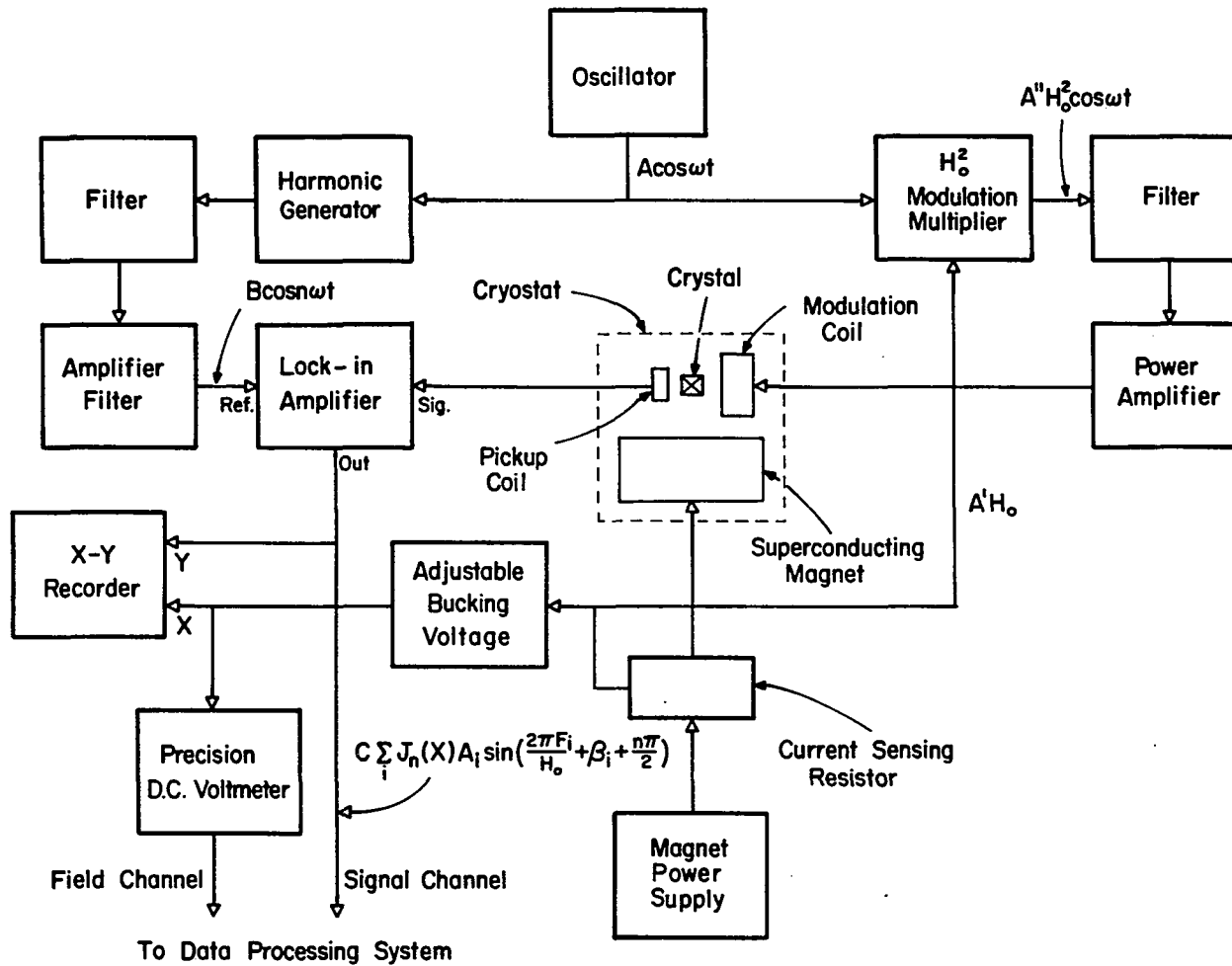


Fig. 20. The detection system.

where X_i has been defined such that

83

$$X_i = \frac{2\pi F_i h}{H_0} \quad (2.6)$$

The expansion of this wave form in a fourier series is well known. In terms of this expansion the magnetization becomes

$$\begin{aligned} \vec{M}_i(t) = & J_0(X_i) \vec{A}_i \sin\left(\frac{2\pi F_i}{H_0} t + \beta_i\right) \\ & + 2 \sum_{n=1}^{\infty} J_n(X_i) \vec{A}_i \sin\left(\frac{2\pi F_i}{H_0} t + \beta_i + \frac{n\pi}{2}\right) \cos(n\omega t) \end{aligned} \quad (2.7)$$

where $J_n(X_i)$ is the Bessel function of the first kind of order n . The voltage induced in the pickup coil is proportional to the time derivative of this quantity

$$V_i(t) \propto \sum_{n=1}^{\infty} n\omega J_n(X_i) A_i (\hat{M}_i \cdot \hat{u}) \sin\left(\frac{2\pi F_i}{H_0} t + \beta_i + \frac{n\pi}{2}\right) \sin(n\omega t) \quad (2.8)$$

where \hat{M}_i is the unit vector along the magnetization due to the i th sheet of the Fermi surface and \hat{u} is the unit vector along the axis of the pickup coil. For the purposes of further discussion this geometrical factor can be ignored because the entire experiment was done at a single crystal orientation of high symmetry. After initial alignment established the c -axis along the magnetic field, the sample was never rotated. Under these conditions the \hat{M}_i 's are all constant. Furthermore, when the magnetic field lies in a direction of such high symmetry, the unit vectors \hat{M}_i tend to lie along that same direction. Since the axis of the pickup coil is very nearly along the c -axis of the crystal, $\hat{M}_i \cdot \hat{u}$ will be very nearly one for all i . If we now choose to consider the contributions from all sheets of the Fermi surface, then the total voltage induced in the pickup coil will be

$$V_T(H_0, \theta, \phi, t) = C \sum_i \sum_{n=1}^{\infty} n \omega J_n(X_i) A_i(H_0, \theta, \phi) \sin\left(\frac{2\pi F_i}{H_0} + \beta_i + \frac{n\pi}{2}\right) \sin(n\omega t) \quad (2.9)$$

where the $\hat{M}_i \hat{u}$ terms have all been absorbed into the overall proportionality constant C .

The form of this expression has important implications for the design of the dHvA effect detection system. First of all, the time dependent induced voltage is composed entirely of harmonics of the modulation waveform. The output of the pickup coil is, therefore, ideally suited for the use of a lock-in amplifier. One may select any single term from the sum over n simply by generating a harmonic of the modulation frequency and using this for the reference channel of the amplifier. That is what we did. The detection system includes a harmonic generator and a lock-in amplifier as shown in Fig. 20. The voltage output of the lock-in is given by

$$V_n(H_0, \theta, \phi) = C' \sum_i J_n(X_i) A_i(H_0, \theta, \phi) \sin\left(\frac{2\pi F_i}{H_0} + \beta_i + \frac{n\pi}{2}\right). \quad (2.10)$$

As the magnetic field H_0 increases during a data sweep, this output will be the usual dHvA oscillations

$$\sin\left(\frac{2\pi F_i}{H_0} + \beta_i + \frac{n\pi}{2}\right) \quad (2.11)$$

except for the constant phase shift $n\pi/2$. On the other hand, the amplitude of each of these oscillatory components is no longer the conventional dHvA amplitude A_i , but is instead this amplitude modified by a multiplicative Bessel function in the manner

$$J_n(X_i) A_i(H, \theta, \phi) \quad (2.12)$$

It is fruitful to consider the effect of constraining the modulation amplitude h to remain proportional to H_0^2 as H_0 is slowly increased. We can express this constraint in the manner

$$h = \alpha H_0^2 \quad (2.13)$$

where α is a constant for a given data sweep. From Eq. (2.6) it is clear that

$$X_i = 2\pi\alpha F_i \quad (2.14)$$

Under these conditions J_n has become a function of dHvA frequency F_i only, $2\pi\alpha$ being a scale factor.

The easiest way to see what is going on here is with the aid of some pictures. Figure 21a shows a schematic dHvA frequency spectrum for a hypothetical metal. The dHvA amplitudes A_i are represented by the heights of the various peaks. If this metal were placed in a sweeping magnetic field under the experimental conditions described above, the output of the lock-in amplifier would be a sum of oscillatory components whose frequencies are represented in this figure. The observed amplitudes of these frequencies would be the product of the A_i 's with the appropriate Bessel function envelope. In Fig. 21b the same spectrum is shown again with a typical envelope drawn in upon it. The function shown is J_6 which is the envelope present when detecting on the sixth harmonic. Figure 22a shows the spectrum as it would be observed at the output of the lock-in. It has been heavily biased to the higher frequencies, but this can be changed by simply adjusting the scale factor α . Figure 22b shows the observed spectrum that results when α is replaced by 2α . The envelope J_6 has been compressed to the

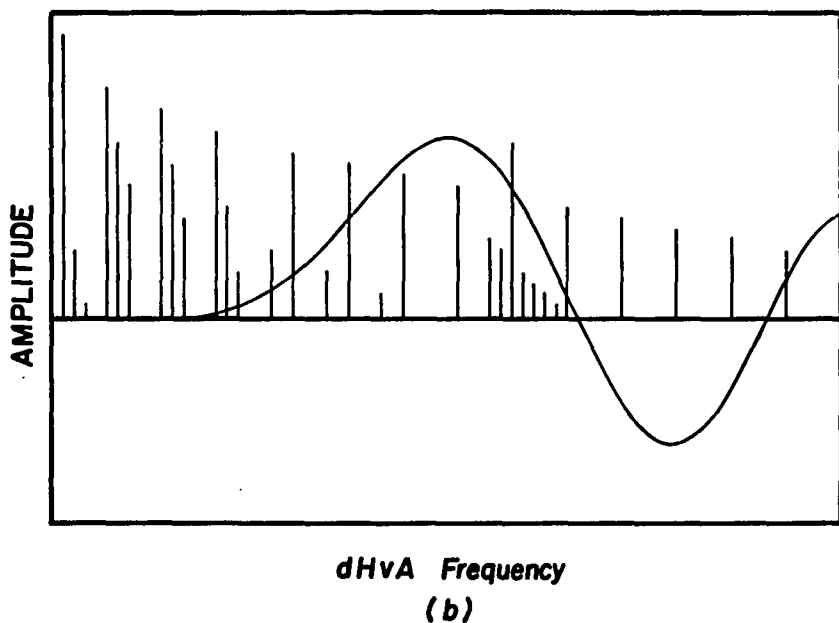
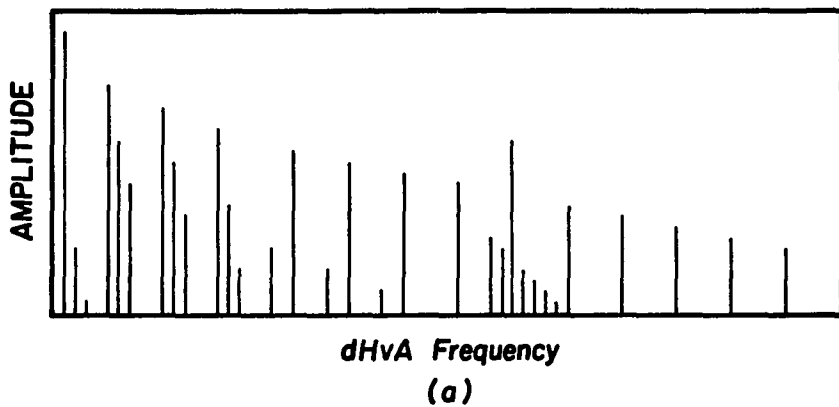


Fig. 21. Large amplitude modulation effects I.

Part (a) shows a schematic dHvA spectrum for a hypothetical metal. Part (b) shows the same spectrum with the Bessel function J_6 drawn in over it.

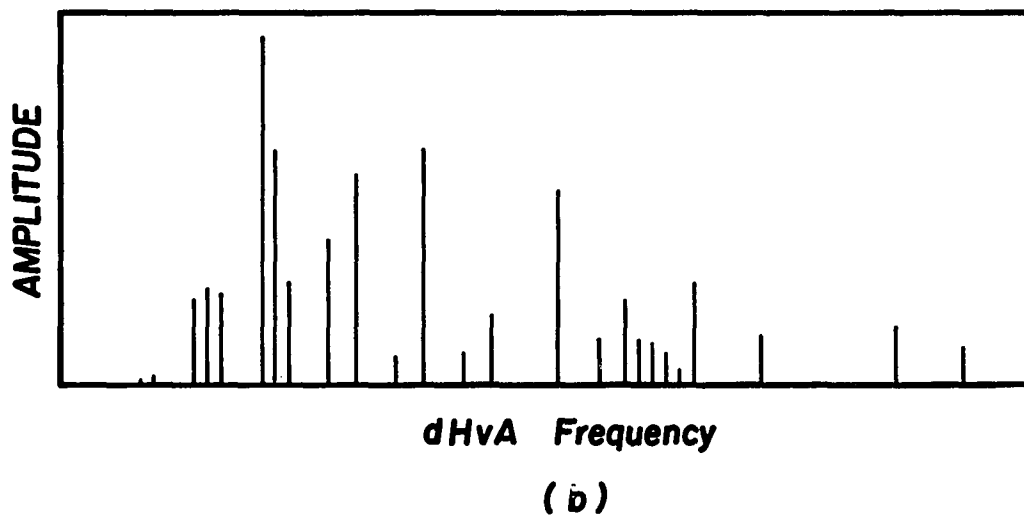
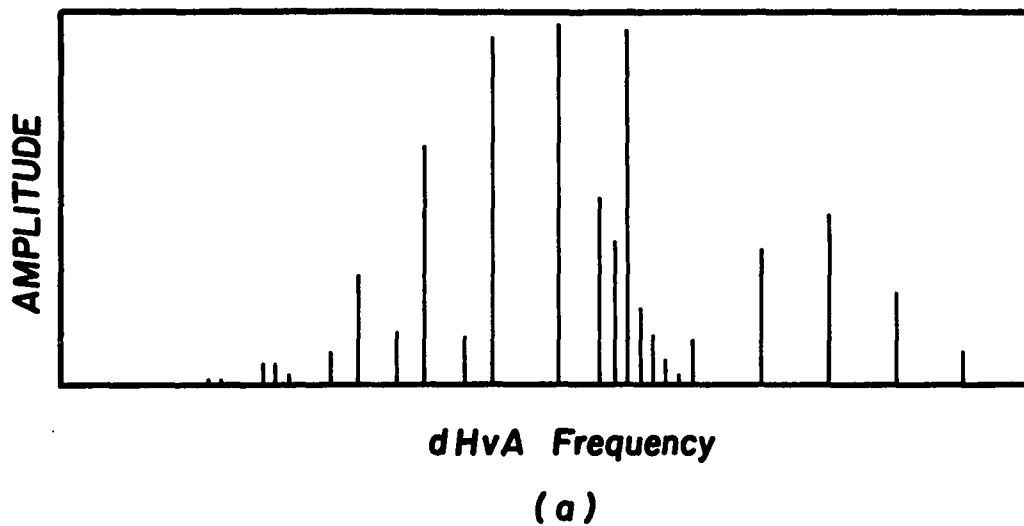


Fig. 22. Large amplitude modulation effects II.

Part (a) shows the effect of the J_6 envelope on the schematic spectrum of Fig. 21. Part (b) shows how the detected spectrum changes when the modulation amplitude is increased by a factor of two.

left by the increased scale factor. It is worth noting that the adjustment of α is not the only degree of tunability available to the experimenter using this system. The choice of Bessel function is also important since the higher order functions have their first maxima at higher frequencies. This means that for a given modulation amplitude one can favor the higher frequencies by detecting on a higher harmonic. It is also true that the system can be made to stay tuned on a given frequency by going to a higher harmonic and turning up the modulation amplitude at the same time. The higher the order of the Bessel function chosen, the more the modulation amplitude must be turned up to compress the scale factor sufficiently to hold the first lobe on the chosen frequency. This compression narrows the Bessel function lobes, and the effect is to narrow band on that frequency.

All of these considerations have been incorporated into the design of the detection apparatus. The system includes a box which accepts a voltage proportional to H_0 on one input channel and the modulation signal on a second channel. The output is a modulation signal whose amplitude is proportional to H_0^2 . This voltage is filtered and sent to the power amplifier which drives the modulation coil. The constant α can be adjusted by turning up the gain on the power amplifier or by similar adjustments on the H_0^2 drive box. These elements are shown in relationship to the rest of the system in Fig. 20. Note that the output of the lock-in is sent directly to the signal channel input to the data processing system and also to the y-axis of an x-y recorder.

The magnetic field sensing system is based on an $80\text{ m}\Omega$ temperature-controlled resistor placed in series with the superconducting magnet. The voltage produced across the resistor is sent to the H_0^2 drive box and also to a three-dial potentiometer. The potentiometer provides a stable, adjustable, dc bucking voltage which is used to subtract off almost all of the voltage proportional to the magnetic field. The millivolts that remain can be amplified by a sensitive dc voltmeter, which permits the accurate measurement of sweeps that are on the order of 20 G long at 40 kG. The amplified field voltage is sent directly to the field channel input of the data processing system. All of this is shown schematically in Fig. 20.

The Data Processing System

From Eq. (1.34) and the discussion of the previous section, it is clear that magnetization signal is an oscillatory function of the reciprocal magnetic field strength. It is also true that the signal is often very rich in harmonic content as is demonstrated by the sample data traces shown in Fig. 23. Data of this kind are ideally suited for processing on a digital computer; in fact, the data obtained in this experiment contain so many closely spaced frequency components that it could not have been analyzed without the aid of an on-line computer. Computers have been integrated into dHvA experiments in the past (see for example, Alles and Higgins 1975, Karim et al. 1978), but these have always tended to be minicomputer based systems. What is new about the present system is that it is based on a microcomputer and, therefore, represents one further demonstration of the inroads these new machines

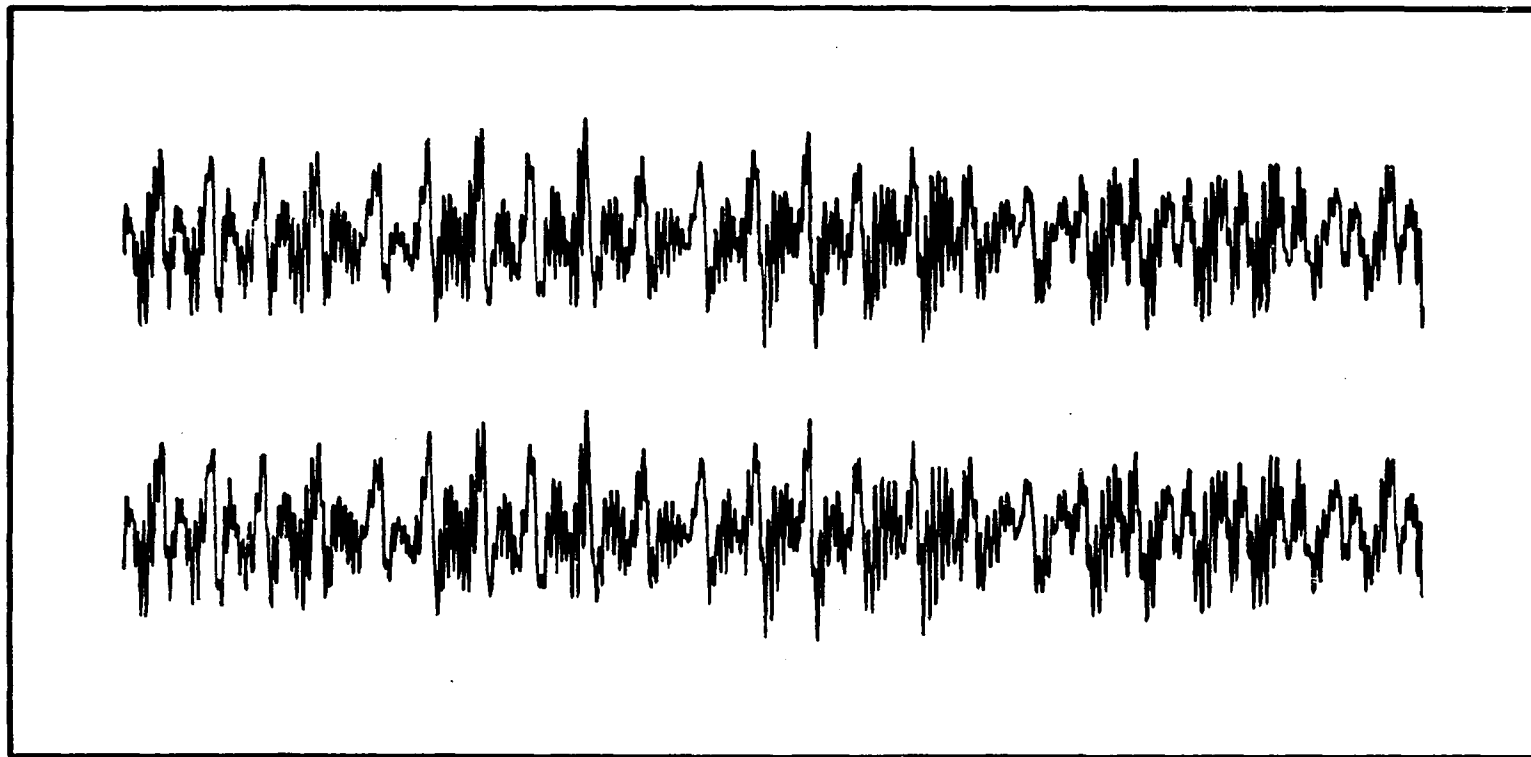


Fig. 23. Two field sweep dHvA spectral scans.

The two traces were taken with identical instrument settings 15 minutes apart to check reproducibility. There is very little noise in either trace. The sweep range is 48.25 kG to 49.31 kG. The temperature is 0.55°K .

are making into areas of serious research. Because it is new, the digital system will be described in some detail.

The principal component of the digital system is an Altair 8800b[®] microcomputer. The computer architecture together with the associated peripherals are shown in Fig. 24. The computer is based on the Intel 8080[®], a popular 8-bit microprocessor, and in the most minimal configuration, it consists of the central processing unit, 4096 bytes (8-bit words) of memory, the I/O controller, a teletype or an equivalent, and a means of mass data entry such as a paper tape reader/punch. The two most important hardware enhancements necessary to make the system viable were the expansion of computer memory to 61,440 bytes, and the addition of a fast access mass storage system in the form of two 8-inch floppy disk drives. Each disk has a storage capacity of 310,000 bytes (310 kbytes), a data transmission rate of 31 kbytes/sec., and a worst case access time of about one second. There is also a Read Only Memory (ROM) controller which was included to facilitate a fast startup. The permanent information stored on the ROM allows the system to "wake up" running a 24-kbyte version of disk based Basic in about four seconds. Operator control of the system is mediated by a Cathode Ray Tube (CRT) terminal with a data transmission rate of approximately 500 char./sec.

The system so far described is still rather elementary. It was further upgraded with a hardcopy printer/plotter, a floating point arithmetic processor, an analog-to-digital converter, and an acoustic telephone coupler. The printer is a medium fast (45 char./sec) character generator with a daisy wheel printhead. It produces text quality printed output, but the primary reason for choosing this printer is the fact

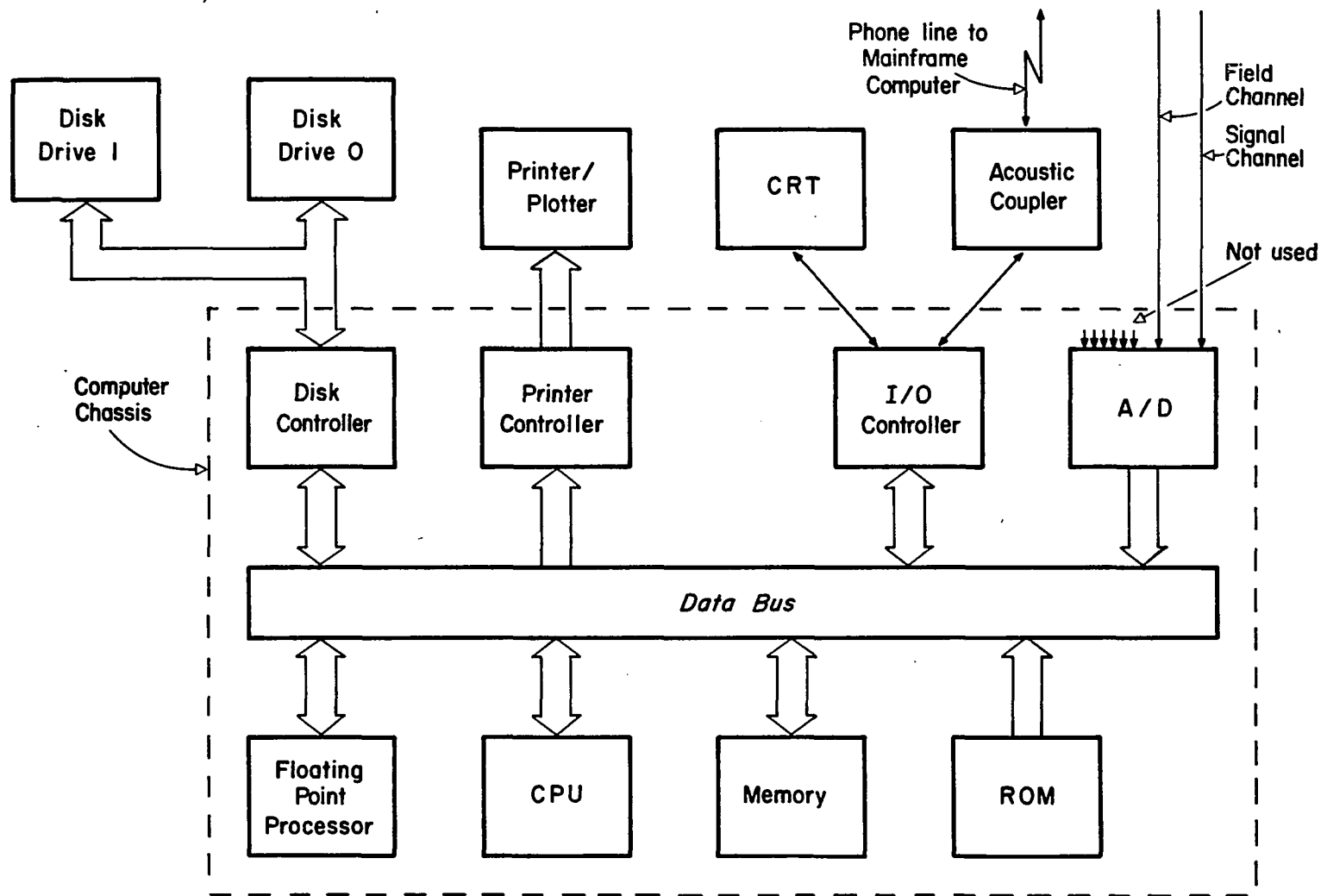


Fig. 24. Block diagram of the data processing hardware.

that the printhead position is software programmable to a resolution of 1/120 inch horizontally and 1/48 inch vertically. This feature allows the machine to be converted easily into a digital plotter capable of graphical displays of finished quality. It was typically used to generate dHvA spectrum scans that were five to ten feet long and would rarely take longer than two or three minutes to do so. The dHvA reproduced in this dissertation were all generated on this plotter.

The arithmetic processor is an important addition to a microprocessor based system if it is going to be used for numerical processing of data lists much longer than about 500 floating point numbers. The data lists generated in this experiment were typically 2048 points long. For such a list the hardware processor could perform a Fast Fourier Transform (FFT), of eight digits precision, in about four minutes. Without the processor, the same calculation would take about twelve minutes. This becomes an important difference when it is necessary to calculate 20 or 30 transforms a day.

The analog-to-digital converter (ADC) is, of course, essential to any data acquisition scheme. Ours was an eight channel multiplexed ADC with 12-bit resolution and an intrinsic conversion time of about 50 μ sec. Of the eight channels, only two were used, and these were connected to the signal and field channel outputs of the detection system.

The acoustic coupler was added to the system to permit interactive communication and data transmission over a phone line to the Digital Equipment Corporation DEC System 10[®] mainframe computer maintained at the University of Arizona Computer Center. This communication

was necessary because there were times when the data lists got to be as long as 8200 points. An FFT calculation on such a list is still well beyond the reach of a microcomputer. When operating in this mode, our system becomes an intelligent remote terminal, capable of digitalizing the data stream, storing it, coding it, and sending it to the mainframe computer. Once the data gets to the DEC10[®], all of the resources of a typical large computer (speed, storage capacity, high level software) can be brought to bear upon it. These resources are all manipulated from the small system CRT terminal.

It is important to note that the basic computer was designed to be easily enlarged. Furthermore, all of the additional equipment was of the plug-in-and-go variety, designed to be compatible with the computer. The system was purchased, partially in the form of kits, in 1977 at a cost of \$11,200. An equivalent system would most certainly cost less than \$10,000 today. A minicomputer-based system would cost much more.

Before discussing the software, it is appropriate to describe briefly the data processing tasks the system is required to handle. First, the dHvA oscillations are not periodic in H ; they are periodic in H^{-1} . If the intention is to transform the data stream into its Fourier spectrum, the signal channel must be digitalized in equal intervals of H^{-1} . One way to accomplish this is to sweep the magnetic field proportional to t^{-1} and then sample linearly in time. We chose instead to sweep the field linearly in time and sample in equal increments of H^{-1} . This is done by first entering into the computer the start and stop field values for a given sweep. Then the number of points in the

sweep is entered and all of these numbers are used to calculate field values spaced equally in H^{-1} between the sweep endpoints. This table is then converted to 12-bit binary. During the sweep, the field channel is continually sampled and compared with this "triggerpoint" table. Whenever a field conversion is found to be larger than a given triggerpoint entry, the signal channel is sampled, the result is stored over that triggerpoint, and the process is then continued with the next triggerpoint. At the end of the sweep, the 12-bit binary triggerpoint table has been entirely replaced by a binary table of signal voltages. The field channel is digitalized and compared at approximately 1 kHz. This means that for a typical sweep this channel is sampled 100 or more times for each sampling of the signal channel. As soon as the sweep is over, the stored information is immediately copied onto one of the floppy disks. This takes about 3 to 4 seconds. A single disk will hold 60 binary lists when each list is 2048 points long.

At this point, the data can be analyzed immediately or stored indefinitely for future analysis. Whenever the data is analyzed, the first step is to remove the excess bits. Because the ADC has 12-bit resolution, each digital conversion is packed into two bytes when stored in the computer memory. It is a peculiar artifact of our ADC that the unspecified bits are in the four lowest order positions of the 16-bit word. This means that the 12 meaningful bits must be right shifted 4 places and the 4 highest order bits set to zero. Once this has been accomplished, the entire list is converted to floating point numbers. Although the arithmetic processor can be initialized to carry out calculations to as many as 14 decimal digits, we normally restrict our

calculations to 8 digits to save time and memory space. (Even at only 8 digits precision a 2048 point binary list expands to 10,240 bytes when converted to floating point.)

After the list has been converted, it is multiplied by an envelope function to control the spurious sidelobes associated with the finite length of the sampling window. The window most generally used during this investigation was a \sin^2 profile applied to the first and last N points in the data list. N was treated as an adjustable parameter, but in most instances we found the sidelobes to be attenuated sufficiently when N was held at about 10% of the total list length. (This is a conventional choice, following Tukey 1967). After windowing, the list is fourier transformed using the standard Cooley-Tukey Fast Fourier Transform (FFT) algorithm (Cooley and Tukey 1965). There is a vast literature on this technique. The interested reader is directed to an excellent introductory text by E. O. Brigham (1974). After the transform is complete, the complex list is reduced to real numbers by taking the square magnitude, and this result is then scaled and displayed on the local plotter.

These are the kinds of tasks our microcomputer-based system was called upon to perform. Characterized most simply, they amount to heavyweight numerical calculations on a lightweight machine. These demands placed a heavy burden on our software; it had to be fast, compact, and flexible. This mandate required immediate abandonment of Basic. Basic is much too slow, and it requires 24 kbytes of memory to store the interpreter. Furthermore, it would have to be augmented

heavily with machine code drivers for all of the peripheral hardware it does not intrinsically support. A disk operating system with a macro assembler and Fortran would be much better, but there would still have to be a lot of assembly language programming to wed the software system efficiently to the hardware. Also, the compiler and the operating system are software black boxes. This can be a major disadvantage. A good way to see this is to imagine the problem one would have modifying the compiler to produce an object code that would support the floating point processor. In general, these high level languages are not very adaptable to hardware environments they were not designed for.

What is needed is a software system flexible enough to allow the experimenter sufficient freedom to select whatever hardware elements are appropriate for the experiment. One such system has been developed here in Arizona by Scott Tilden and Bonner Denton of the University of Arizona Chemistry Department. Their system is called Convers; it will run on any 8080-based machine (and possibly some others by now), and it is available upon request (Tilden and Denton 1978). Convers played a crucial role in the success of this investigation; the microcomputer was able to meet the demands of the experiment only to the extent that the inherent limitations of the hardware were not aggravated by additional limitations in the software overlay. Since Convers was important to the success of the experiment, and since it is new and has been written about so little, it is appropriate to include some description of it in this dissertation. On the other hand, Convers is difficult to describe in just a few words. A true understanding of the system must involve a rather detailed knowledge of the internal system structure

and also the specific system response to about 30 or 40 of the most basic commands. In addition, most of what Convers does in the context of our experiment is quite low level; any concrete description of this would be overburdened with 8080 processor details. Such a digression is not of general interest. In the following paragraphs, I hope to strike a reasonable compromise. Convers will be described in general terms with the hope of conveying a feeling for its compactness, speed, and flexibility. Some additional details and specific examples of its application to this experiment are given in Appendix A.

The irreducible kernel of Convers, as it is obtained from Tilden and Denton, consists of 1200 bytes of machine code. This list is arranged in the form of a dictionary, each entry of which has an identifier, a linking address, and an associated list of code which makes up that dictionary definition. When this kernel is loaded and running, it waits for a command to be typed on the input terminal; as soon as this occurs, the system conducts a fast, linked search through all of the dictionary entries until it finds an identifier which matches the typed command. When the identifier is found, the machine code that follows it is executed immediately and the system returns and waits for the next command. The commands that have been included in the initial vocabulary are all of those necessary for this minimal activity. There is an entry in the dictionary to accept characters from the input terminal, an entry to conduct the linked search through the dictionary, an entry to execute the associated code if a match is found, and so on. It is important to understand that whenever Convers executes a dictionary entry in response to a command typed in at the terminal, it is doing

this by sequential execution of other entries. (Even this sequential execution is determined by the execution of still another dictionary entry.) Convers is 100% dictionary. There is no external program operating the dictionary. This fundamental feature of the structure of Convers has powerful consequences. First of all, the minimal dictionary has been provided with the commands necessary to make new dictionary entries. The user simply informs the system that a new command entry is coming and then types the name of the new entry and then its definition. The definition can be in terms of machine code or any of the commands already in the dictionary. Convers automatically adds the entry to the end of the dictionary, complete with identifier and linking address. This new entry is structured identically in every way to those which precede it, and it will be searched for, and executed when found, just like any of the rest. Furthermore, any subsequent additional entries may contain this new command as part of their definitions. It is not difficult to see how this kind of command nesting can quickly give rise to powerful constructs, and to emphasize once more, these constructs have the same priority in the system as the most primitive command to input a single character from the terminal. This feature is exceedingly useful when dealing with peripheral equipment. A typical component of such hardware will generally have a small inventory of programmable functions, each of which will be controlled by a short sequence of machine code commands. A good example of this is our Analog-to-Digital Converter (ADC) which has only three functions: it can be initialized, it can be told which channel to activate, and it can be told to convert the voltage on a channel to a 12-bit binary

number. Each of these functions is controlled by short machine code programs specified by the manufacturer. In a Convers-based system, it is very easy to define three dictionary entries whose associated definitions are nothing more than these three specified sequences. One might call them A/D-INIT, PIKACHNL, and GRABA#. From then on, the experimenter could control the ADC, in any subsequent programs, simply by invoking these three commands; all the details of the machine code requirements could be forgotten. The ADC would be as fully a part of the system as the input terminal.

Two additional points about the system are worthy of emphasis. When Convers is being used to define a new dictionary entry, it is put into what is called the "compile" mode. When the system is in this mode, any commands typed after the name identifier of the new definition are assumed to be part of that definition. After each of these commands is typed, the dictionary is immediately searched for a match. However, once the correct entry is noted, and a call to that address is inserted into the new definition. This is important because it means that when the new command is eventually executed, no additional searches of the dictionary are necessary, even if that command consists of nothing but previously defined entries. All of the searching is done at the time the new command is defined. In a real sense, the user interactively compiles the new dictionary entries. This is why the creators of the system refer to it as an "interpretive compiler" (Tilden and Denton 1979). And this is why Convers can be very fast.

Finally, there are no software black boxes in Convers. This is due, in part, to the enlightened attitude of Tilden and Denton, who provide a complete listing of every byte in the kernel and a complete

explanation of what each command in the kernel does and how it does it. Just as important is the fact that the modularity and strict uniformity inherent in the system structure quickly provides the user with sufficient confidence to change even the kernel if necessary (possibly to change an I/O routine, for example). Every byte in the machine is accessible to the programmer. This is certainly not the case with Fortran or Basic.

CHAPTER 3

THE EXPERIMENTAL DATA

The experimental data presented in this chapter will be in the form of dHvA frequency spectra. These spectra are most often displayed as computer generated plots of fourier component intensity (square of the amplitude) versus frequency. Owing to the fact that dHvA oscillations are periodic in H^{-1} , the frequencies are measured in units of magnetic field, but for purposes of interpretation these have been converted into units of area in \vec{k} space (expressed in atomic units) via the Onsager relation (Eq. (1.21)). This is done so that the frequency spectrum peaks may be easily associated with Fermi surface cross sections. (Peaks will be referenced either by frequency or by associated \vec{k} space area. For example, a given peak might be said to have the frequency or the area of the A orbit.) The vertical axes of the various spectral plots are expressed in arbitrary units of spectral component intensity. No absolute scale is meaningful because of the many indeterminate gain factors that amplify the magnetization signal before it can be digitalized. The overall gain is, of course, held constant during a field sweep or during a series of field sweeps over which intensities are to be compared. A typical field sweep produced dHvA oscillations that look qualitatively like those displayed in Fig. 23 (with more or less harmonic content). During the course of the sweep, the wave form is sampled N times (usually $N = 2048$) between two well-defined

magnetic field values. These endpoints are used to determine the sampling period (constant in inverse H) which in turn is used to infer the frequency scale of the spectrum display that results from the FFT calculation. In the discussion that follows, the sweep lengths will be given in terms of the number of γ periods spanned. This is convenient because it specifies the resolving power of the sweep. The one γ period sweep would not resolve the two peaks associated with A and $A+\gamma$. The $\gamma/10$ sweep would not resolve A and $A+10$. Finally, the location of the first Bessel function maximum is specified on each spectrum plot so that the effect of this envelope may be taken into account when the spectrum is interpreted. The location of this maximum is inferred from the dc field strength and the modulation field amplitude and frequency. (See Chapter 2 for details relating to the Bessel function envelope.)

The first dHVA spectrum is shown in Fig. 25 and corresponds to a 2048 point digitalization of a field sweep approximately one γ period long that begins at 49.91 kG and extends up to 51.14 kG. (All sweeps were taken from low to high field.) The display has been split into two segments to more conveniently fit on the page. For this sweep, the first Bessel function maximum is off scale to the right of the bottom segment. The temperature was 0.32°K . The low frequency peaks lend themselves to easy interpretation since they are located at .155, .287, .431, and .575 a.u., respectively. These areas correspond to the A orbit (Stark 1967) and the higher multiples 2A, 3A, and 4A (5A appears to be barely discernable). This excellent agreement with previous results is probably somewhat fortuitous because of the coarse resolution of this display. Each peak position is determined no better than $\pm\gamma$

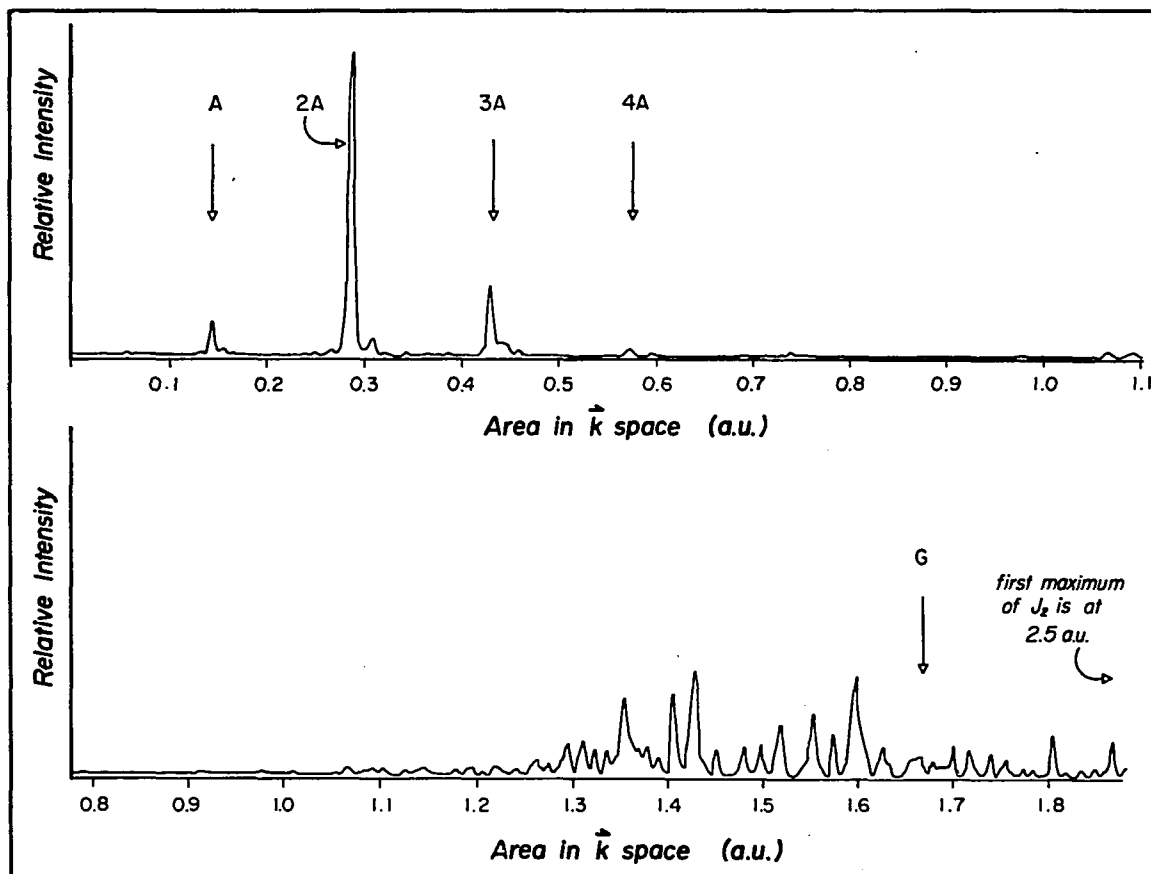


Fig. 25. Fourier transform of digitalized dHvA field sweep data.

The field sweep starts at 49.91 kG and is approximately one γ period long. The temperature is 0.32 $^{\circ}$ K and the first Bessel function maximum is at 2.5 a.u. The rather long spectral plot has been split in half to fit on the page.

$(A_{\gamma}^{(k)}) = .00598$ a.u., Stark 1967) and is represented by no more than one or two frequency points (which accounts for the jerky appearance of the line shapes). In addition, from the discussion of FS theory in Chapter 1, these A peaks are really expected to be complexes of two or more constituents separated by γ . Again, these are not resolvable for a sweep that is just one γ period long.

There is certainly nothing about these four evenly spaced A peaks that can be said to contradict FS. Even the fact that A appears to be much smaller than 2A can be attributed to the fact that the amplitudes of the two peaks are not well defined by the coarse grid and to the action of the Bessel function. In this case, the Bessel function is $J_2(x)$ since the lock-in amplifier was tuned to detect the second harmonic of the modulation frequency. In the low frequency limit, this envelope goes like x^2 so the intensity of 2A will be enhanced by a factor of 16 over the intensity of A. The peaks at the high frequency end of Fig. 25 are much more difficult to interpret. The expected position of the G peak has been drawn in and is found to be well above the "center of mass" of the entire complex. Areas cannot be assigned to these peaks for two reasons. First, the theory of FS does not predict any dHVA frequencies in this entire region (see Fig. 17). As emphasized in Chapter 1, there are no simple closed orbits corresponding to G-A, G-2A, G- γ , etc. Second, these peaks do not remain stable in amplitude or frequency even for small changes in the dc magnetic field strength, though they are quite reproducible for fixed starting field. This lack of stability is shown explicitly in Fig. 26.

Shown in Fig. 26 are the transforms resulting from two separate, short ($\gamma/10$) sweeps that were taken at 50.11 kG and at 50.25 kG (a little less than $\gamma/10$ apart). The sweep range was held short to focus attention on the high frequency components of the spectrum. Even though the field was changed by less than 1/2% between sweeps, the resulting spectra are remarkably different. The behavior is qualitatively what would be expected from a broad band of closely spaced peaks extending from below G all the way up to 2G, which are only very imperfectly resolved by the short sweep length and which are beating together to produce the dramatic shifts of spectral intensity. This broad band of frequencies is not anticipated in FS theory. The theory predicts no frequencies immediately below G and those between G and 2G ($G+A$, $G+2A$, $G+A+\gamma$, etc.) decline quickly in amplitude at the progressively higher frequencies. The spectral intensity is expected to be much more closely confined to peaks near G, 2G, 3G, etc. At the low frequency end of the spectrum, there is some change but nothing that cannot be attributed to poor resolution of the A, 2A, and 3A complexes. Proper resolution of these low frequencies require sweep lengths on the order of one γ period or longer.

Note that the transforms in Fig. 26 have a smoother line shape than that shown in Fig. 25. (The remaining step structure on the tall peaks is caused by the 1/48 inch minimum paper feed step increment of the printer plotter.) This is due to the fact that the Fig. 26 transforms were calculated from a 8192-point data list rather than a 2048-point list such as the one used for the earlier transform. The long list was composed of 1024 points of digitalized data followed by 7168 trailing zeros. The reason for doing this is to reduce the transform

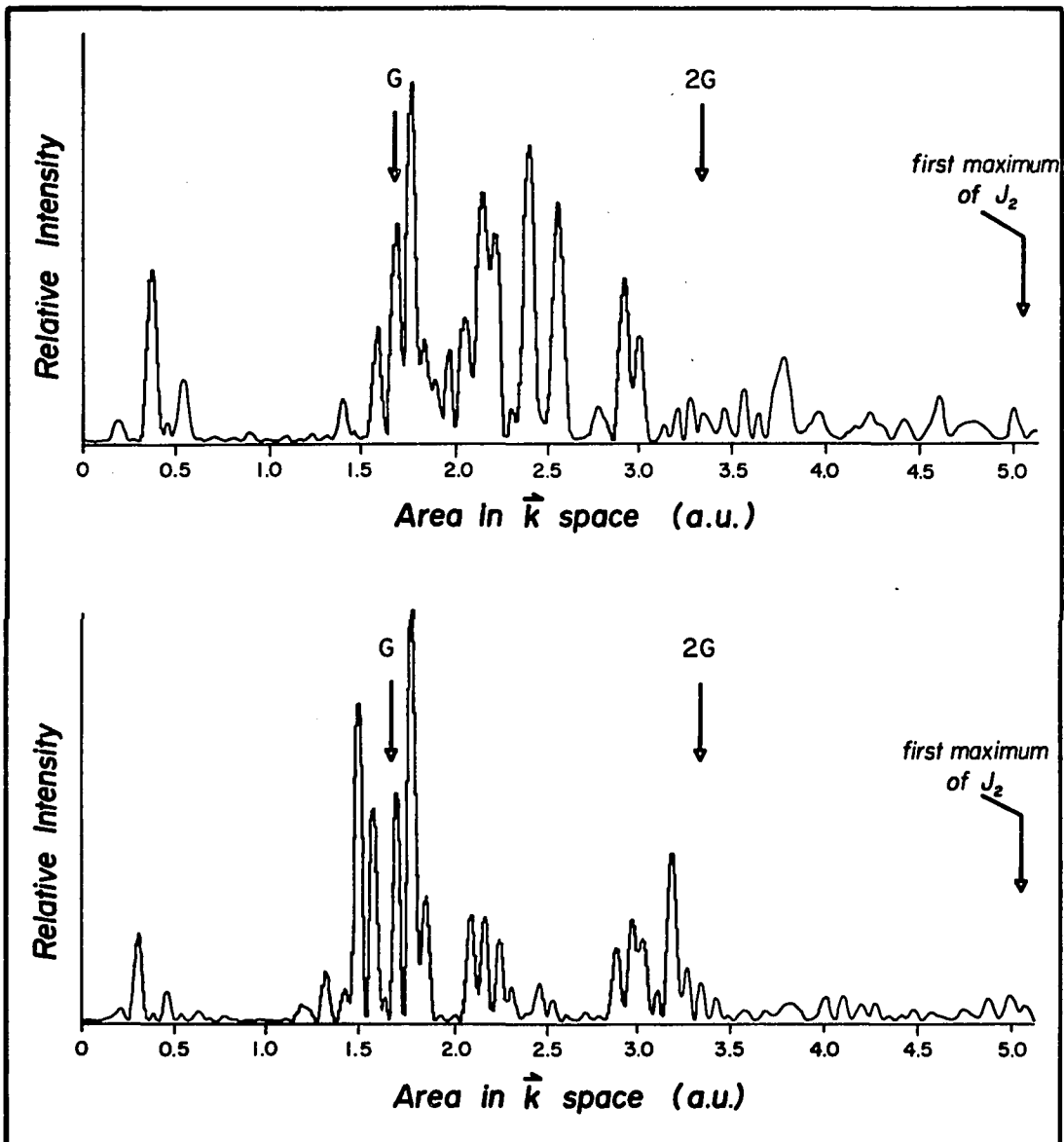


Fig. 26. Two Fourier transforms showing dHvA peaks in the high frequency regime.

The two data sweeps start at 50.11 and 50.25 kG and are each 0.1 γ period long. The temperature is 0.3°K. The horizontal and vertical scales are the same for the two plots. Note the dramatic change in appearance corresponding to a $\frac{1}{2}\%$ change in the magnetic field.

frequency step increment so that each peak is more completely displayed and each peak amplitude clearly defined. This technique was employed in all of the quantitative amplitude dependence studies.

The transforms shown in Figs. 27, 28, and 29 present the results of a systematic study of amplitude dependence upon field strength. The data sweeps are one γ period long and also spaced apart by one γ period. (The starting field of each is the same as the ending field of the previous.) The entire series was taken with the first maximum of J_2 held at 1.9 a.u. and with the temperature held at 0.3°K . The twelve starting fields are listed on the figures. The vertical scales have been adjusted so that the tallest peak on each transform is always the same height. This was done to display most clearly the relative intensities within a single transform and to show how these change from sweep to sweep. (The quantity I_{max} is the intensity of the tallest peak of a given transform.) The A, 2A, and 3A peaks are clearly visible in every transform and have been labeled at the top of the three figures. The average of the twelve frequency values for each peak is .147, .291, and .438 a.u. (all ± 0.003), respectively. There are other recurring features of these transforms. In seven out of the twelve, there is a clear indication of pairs of evenly spaced peaks on either side of each of the A-type peaks. These sidebands have been positively attributed to magnetic interaction effects, a subject that has not yet been addressed in this dissertation.

In all of the foregoing discussion, the electron response to the magnetic field has been expressed in terms of the applied field H . Because the conduction electron orbits extend over many cells of the real space lattice, it should be more appropriate to talk about response to

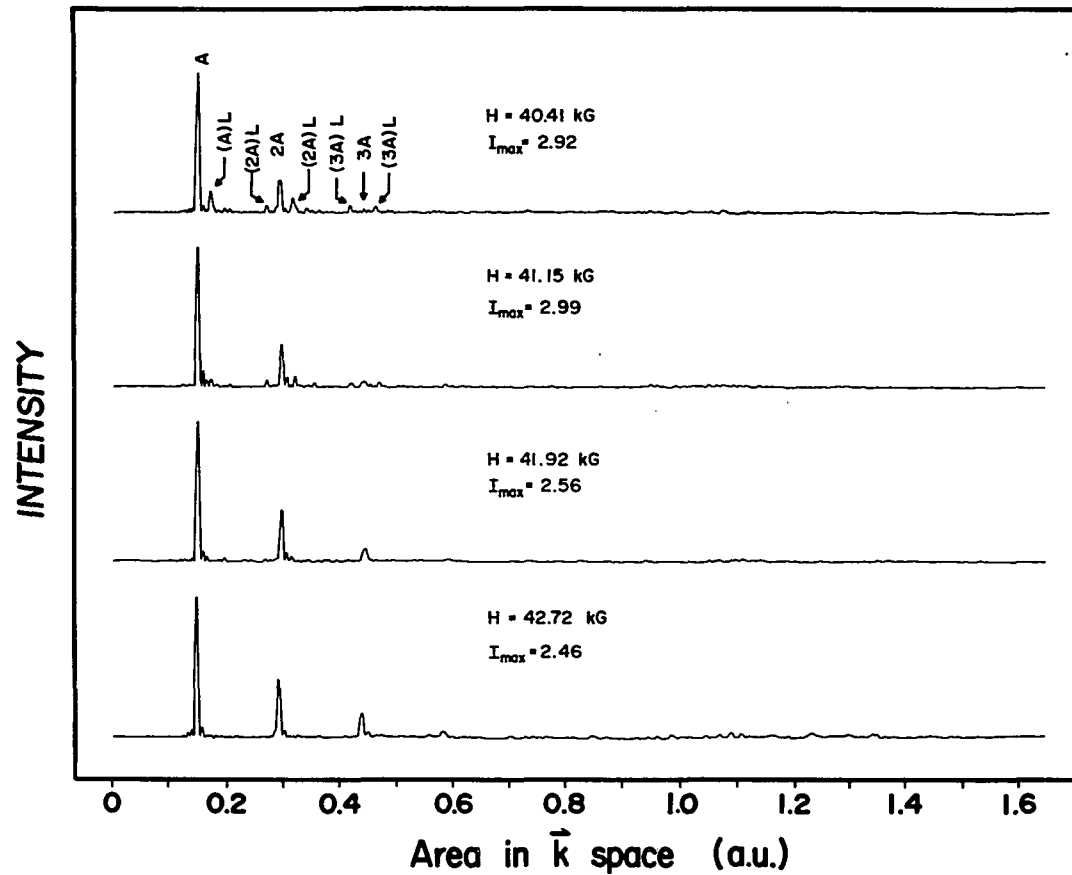


Fig. 27. Magnetic field dependence of coupled orbit dHvA spectra I.

These spectra are the results of Fast Fourier Transform of data produced by one γ period field sweeps and sampled 2048 times. The temperature is constant 0.3°K and the first Bessel function maximum is at 1.9 a.u.

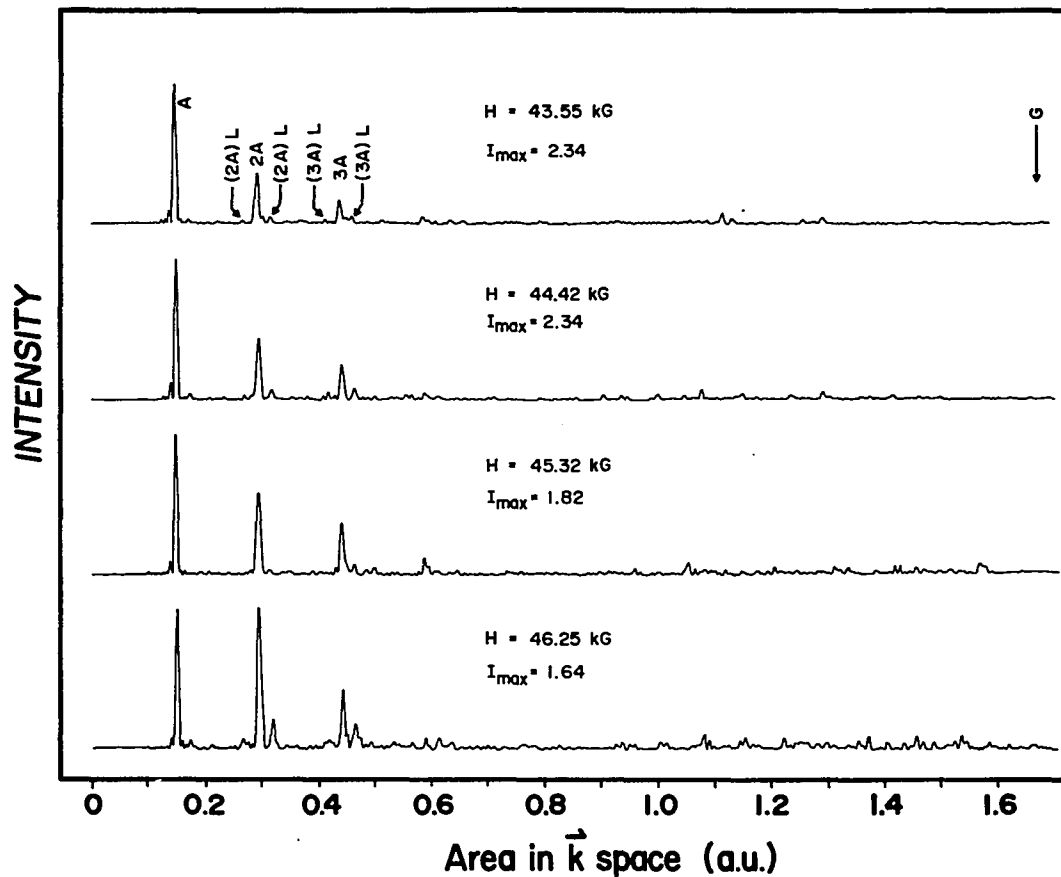


Fig. 28. Magnetic field dependence of coupled orbit dHVA spectra II.

These spectra are the results of Fast Fourier Transform of data produced by one γ period field sweeps and sampled 2048 times. The temperature is constant 0.3^oK and the first Bessel function maximum is at 1.9 a.u. This figure is a higher field continuation of Fig. 27.

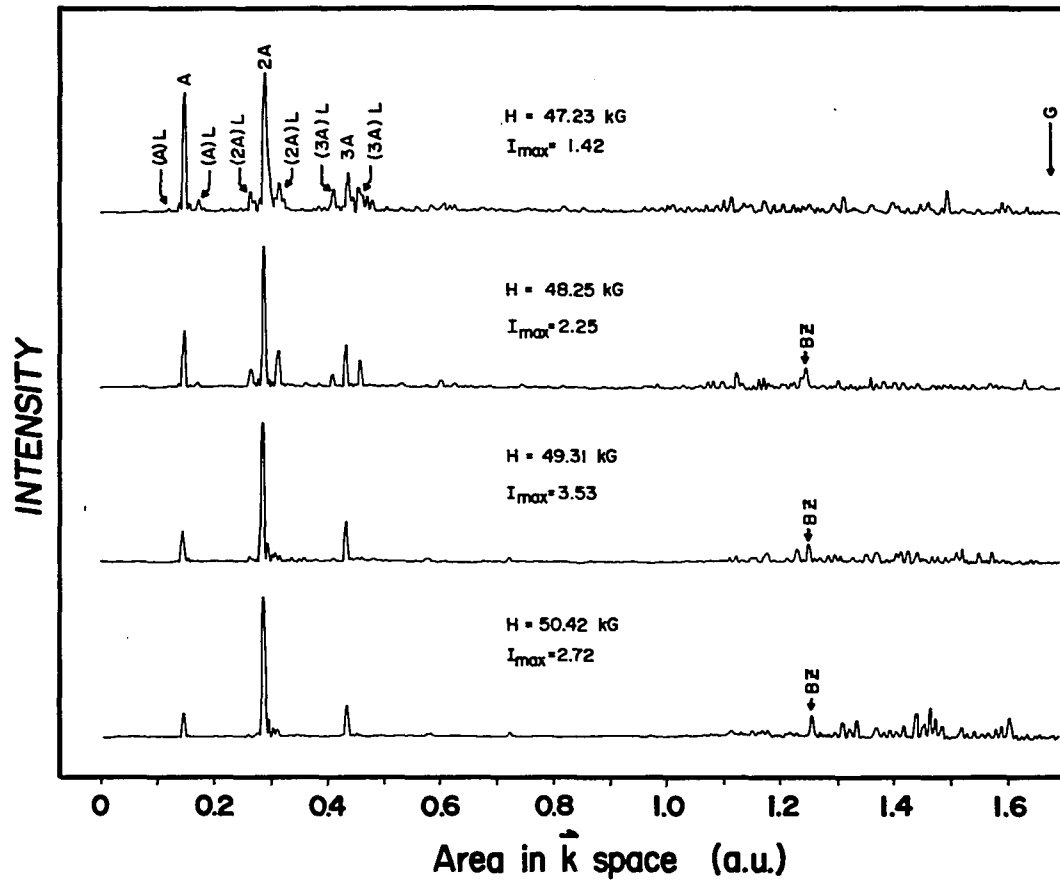


Fig. 29. Magnetic field dependence of coupled orbit dHvA spectra III.

These spectra are the results of Fast Fourier Transform of data produced by one γ period field sweeps and sampled 2048 times. The temperature is constant 0.3°K and the first Bessel function maximum is at 1.9 a.u. This figure is a higher field continuation of Fig. 28.

the total macroscopic average field \vec{B} . Schoenberg (1962) first pointed this out and suggested that it is not necessary to discard the Lifshitz-Kosevich theory of the dHvA effect in favor of a more general theory, but rather the results of the old theory might be modified to handle the case of large magnetic interactions simply by replacing H with B in the expression for the dHvA magnetization (Eq. 1.34). (This straightforward modification has since been justified by Pippard (1963) on theoretical grounds.) When H and M are parallel, the substitution is performed simply and the result is

$$\vec{M} = \sum_j \vec{A}_j(\vec{B}) \sin\left(\frac{2\pi F_j}{H+4\pi M} + \beta_j\right). \quad (3.1)$$

The expression for the dHvA magnetization has been transformed into a self-consistency condition which requires successive approximation methods for accurate solution. However, in situations where the magnetic interactions are small, adequate solutions can be obtained by truncating the iterative process after the first approximation. As an example, consider the interaction between two magnetization components M_a and M_b for which Eq. (3.1) becomes

$$M_a + M_b = A_a \sin\left(\frac{2\pi F_a}{H+4\pi(M_a+M_b)}\right) + A_b \sin\left(\frac{2\pi F_b}{H+4\pi(M_a+M_b)}\right) \quad (3.2)$$

when \vec{M} and \vec{H} are assumed parallel and constant phase factors β_a and β_b are dropped. The magnetization is never very large compared to H, so $4\pi M/H \ll 1$ and hence

$$\begin{aligned}
M_a + M_b = & A_a \sin \left(\frac{2\pi F_a}{H} - \frac{8\pi^2 F_a^2}{H^2} (M_a + M_b) \right) \\
& + A_b \sin \left(\frac{2\pi F_b}{H} - \frac{8\pi^2 F_b^2}{H^2} (M_a + M_b) \right).
\end{aligned} \tag{3.3}$$

To a first approximation, the B dependent magnetization $M(B)$ may be replaced in the sine arguments by the Lifshitz-Kosevich magnetization $M(H)$ and the result is

$$\begin{aligned}
M_a + M_b = & A_a \sin \left[x_a - y_a A_a \sin(x_a) - y_b A_b \sin(x_b) \right] \\
& + A_b \sin \left[x_b - y_b A_a \sin(x_a) - y_b A_b \sin(x_b) \right]
\end{aligned} \tag{3.4}$$

where

$$\begin{aligned}
x_a &= \frac{2\pi F_a}{H} \\
y_a &= \frac{8\pi^2 F_a^2}{H^2}
\end{aligned} \tag{3.5}$$

and similarly for x_b and y_b . If the field spacing of the dHVA frequency F_a is denoted by ΔH , then

$$\frac{F_a}{H} - \frac{F_a}{H+\Delta H} = 1 \tag{3.6}$$

and from this

$$\Delta H = \frac{H^2}{F_a + H} \approx \frac{H^2}{F_a} \tag{3.7}$$

since $F_a \gg H$ for all frequencies of interest. From this result, $y_a A_a$ is seen to be π times the peak to peak amplitude of the magnetization M_a measured in units of this field spacing. For weak magnetization

conditions, all four quantities of this type that appear in (3.4) will be sufficiently small to allow terms of order $(yA)^2$ or higher to be dropped. In other words, the sine arguments are both of the general form $\sin(b-s)$ where s is small compared to π . Expanding the sine yields

$$\begin{aligned} \sin(b-s) &= b-s - \left[\frac{1}{3!} (b^3 - 3b^2s) + \frac{1}{5!} (b^5 - 5b^4s) \right] + \dots \\ &= b - \frac{b^3}{3!} + \frac{b^5}{5!} + \dots - s \left[1 - \frac{b^2}{2} + \frac{b^4}{4!} - \dots \right] \\ &= \sin b - s \cos b . \end{aligned} \quad (3.8)$$

When written in these terms (3.4) becomes

$$\begin{aligned} M_a + M_b &= A_a \sin(x_a) - y_a A_a^2 \sin(x_a) \cos(x_a) - y_a A_a A_b \sin(x_b) \cos(x_a) \\ &\quad + A_b \sin(x_b) - y_b A_b^2 \sin(x_b) \cos(x_b) - y_b A_a A_b \sin(x_a) \cos(x_b) , \end{aligned} \quad (3.9)$$

and this can be written again in terms of the field H

$$\begin{aligned} M_a + M_b &= A_a \sin\left(\frac{2\pi F_a}{H}\right) + A_b \sin\left(\frac{2\pi F_b}{H}\right) \\ &\quad - 4\pi^2 \frac{F_a A_a^2}{H^2} \sin\left(\frac{4\pi F_a}{H}\right) - 4\pi^2 \frac{F_b A_b^2}{H^2} \sin\left(\frac{4\pi F_b}{H}\right) \\ &\quad - 4\pi^2 \frac{A_a A_b}{H^2} \left\{ (F_a + F_b) \sin\left[\frac{2\pi(F_a + F_b)}{H}\right] - (F_a - F_b) \sin\left[\frac{2\pi(F_a - F_b)}{H}\right] \right\} . \end{aligned} \quad (3.10)$$

The first pair of terms are the standard Lifshitz-Kosevich dHvA magnetizations. The second and third pairs of terms are the lowest order magnetic interaction contribution. If F_a is significantly larger than F_b , the peaks produced by the third pair of terms will appear as sidebands spaced F_b in frequency above and below the central peak at F_a . The higher frequency sideband is predicted to be slightly larger in

amplitude than the lower sideband. Also, for given amplitudes A_a and A_b , both sidebands will appear to be larger in relation to higher frequency central peaks. All of these characteristics are evident for the sidebands of the A-type peaks in each of the three figures. (The low-high pattern is exaggerated by the action of the Bessel function envelope.) The average frequency separation from the central peak is $.0244 \pm .003$ a.u. and this corresponds to the L orbit previously reported by Stark (1967) as 0.0234 a.u. The L orbit is not part of the coupled orbit system but related instead to an orbit on the third band butterfly and the fourth band electron pocket (see Fig. 2). The two surfaces are separated by small band gaps which are easily broken down to produce an elliptical path which might be best understood with reference to Fig. 1. These MB orbits give rise to dHvA frequencies which are the same as what would result from a sheet of the Fermi surface having the geometry of a convex lens centered on the $(10\bar{1}1)$ -type Brillouin zone faces. These are the six lens shapes visible in Fig. 1. Each will have extremal cross sections when sliced perpendicular to the field. When the field is oriented along the c-axis, the extremal cross section of each lens will be the same. But if the field is tilted somewhat, the various lenses will be sliced differently, depending upon the degree and direction of tilt, and they will each contribute a slightly different dHvA frequency. These frequencies will beat with one another, and since each lens makes the same contribution to the total dHvA signal, the L component will be observed to disappear with the beat period of the complex. As the L component disappears, so too will any magnetic interaction effects that result from this component. Independent data

taken at lower fields show the low frequency L peak to have a basic heat period of 10γ , and this agrees with the behavior of the sidebands of Figs. 27, 28, and 29. (There is a clear minimum of sideband intensity at the 41.92 kG as well as the 50.42 kG sweep.) All of this evidence is conclusive in requiring the assignment of the sideband peaks to magnetic interaction coupling between the A and L components in the dHvA signal. These peaks have been so labeled in the figures. (The notation A(L) has been used to distinguish frequency components that result from magnetic interactions from those that arise from combinations of closed orbits in the coupled orbit network. For example, the label $A+\gamma$ is used to denote a peak arising from the network orbit shown in Fig. 15 while $(A)\gamma$ denote the peak that results from magnetic interaction coupling between the network γ and the network A orbits.)

The angular variation of the L frequencies is well understood (Stark 1967), and consequently, it is possible to infer the degree to which the magnetic field is tilted with respect to the c-axis. The indication is that the crystal is misaligned by about one degree. The reason for this misalignment is not clear to us and is a disappointment since the x-ray and alignment procedures that were used usually result in alignment accuracies on the order of 0.1° .

What is particularly interesting about this series of spectra is not so much the identification of the various peaks, but rather the field strength dependent behavior of the intensities of the A and 2A peaks. This behavior is the focus of Fig. 30 which shows the amplitudes (square root of intensity) of A and 2A from 33.21 kG to 50.42 kG. The last twelve pairs of experimental amplitudes shown in the figure were

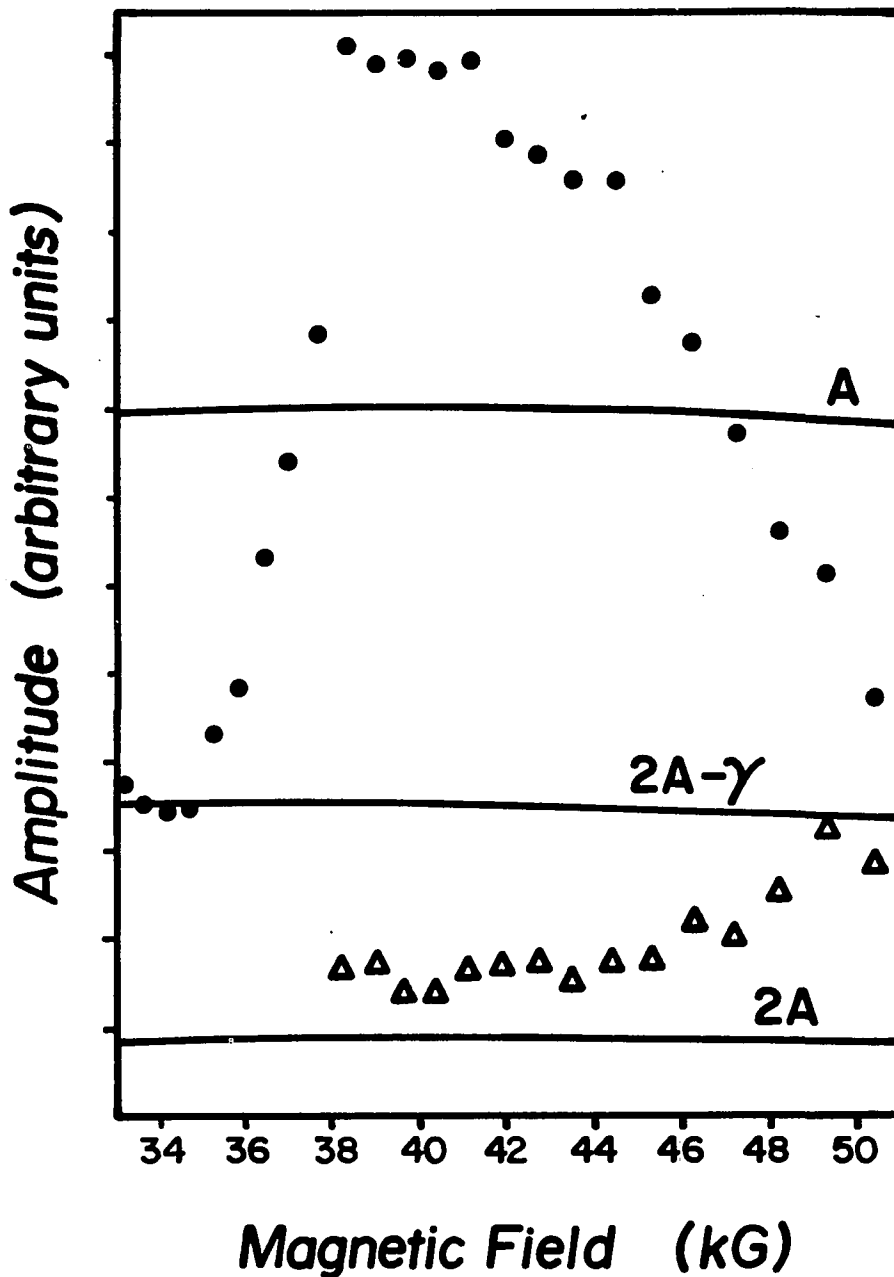


Fig. 30. Comparison of theory and experiment for the amplitude of the A peak.

The solid dots are the experimentally determined values for the amplitude of A. The open triangles are the 2A amplitudes. The theoretical predictions for the amplitude of A, 2A- γ , and 2A are represented by solid curves.

taken from the transforms in Figs. 27, 28, and 29. The effect of the Bessel function has been removed from the data. The theoretical prediction for the A, 2A- γ , and 2A amplitudes has also been included. The theoretical A curve has been normalized to run through the middle of the A amplitude data. The 2A- γ and 2A curves have been normalized with this same factor in order to preserve the predicted ratios with the A amplitude.

It is quite clear that the experiment is in qualitative disagreement with the theory. Unfortunately, quantitative comparison is prevented by the magnetic interaction effects that are undoubtedly contributing. (Henceforth, magnetic interaction effects will be referred to as MI effects.) The existence of the A(L) sidebands proves that MI is present and significant, but at the same time they also agree well with the predictions of (3.10), which is a clear indication that the small interaction analysis is valid for the interpretation of A-L coupling. Other data taken at higher modulation amplitudes (to make the lower frequencies visible) and at the same temperature and field range show the fundamental L peak to be somewhat larger than the A peak, and consequently, these same arguments apply to A-2A coupling. In the small interaction limit, it is possible that some of the growth in the 2A amplitude is attributable to the decrease in the A amplitude. Equation (3.10) shows a contribution to the second harmonic resulting from first order magnetic interaction component of 2A. The decrease in A might produce less destructive interference of the components in the 2A peak and result in a larger perceived signal. However, even if the coupled orbit component of 2A were fully as strong as the 2A- γ prediction in the figure,

in the small interaction limit no magnetic interaction sideband of a peak of this latter's amplitude could produce such a profound reaction in the much larger A peak.

The possibility of MI coupling of the A frequency to the low frequency components of the dHvA spectrum must also be considered. The four orbits with frequencies low enough to produce sidebands that are left unresolved by the one γ sweep are α , μ , T, and γ . (The first three of these are not part of the coupled orbit system. For discussion of these orbits, see Stark 1967.) Of these orbits, α , μ , and γ can be discarded as candidates since they are all quite small in this field range. On the other hand, the T orbit with a measured cross section $A_T^{(k)} = .00634$ a.u. (Stark 1967), slightly larger than the cross section of γ , has an amplitude that is quite strong in this field range. (Stark observed T to dominate γ for fields above 15 kG.) A significant sideband component (A)T would cause beating at the frequency of T. Since the sweep length in this series is one γ period, the beat waist would appear to move across the sampling window from one sweep to the next. The difference between the γ and T areas is 3.6×10^{-4} a.u., and so the waist would move entirely across the window with a period equal to 16.6 periods. This explanation of the A amplitude behavior shown in Fig. 30 can be effectively ruled out. First, the period of oscillation of the A amplitude in the figure is at least 24γ . Second, the sweep length is almost exactly one T period. This means that the entire beat cycle is sampled on each sweep, and hence the position of a beat waist in the window cannot have much effect. Third, nothing resembling such a

sliding beat waist is visible in the data. The profound amplitude fluctuation of A in Fig. 30 cannot be attributed to MI sidebanding with T.

As easily ruled out is the suggestion that this surprising amplitude behavior can be attributed to a Bessel function effect. The position of the envelope was held constant for the entire series of sweeps, and even if some drift were to have occurred, the effect of this would not be to enhance 2A relative to A. Instead, the two peaks would move up and down together since both are on the x^2 tail of $J_2(x)$.

Further light is shed upon the question of composition of the various peaks by investigation of their effective masses. For this purpose a second series of one γ sweeps was taken at the 48.25 kG starting field. The field was swept repeatedly over this range while the temperature was varied in twelve increments from 1.02°K down to 0.36°K . The temperature dependent amplitudes were then fit to the Lifshitz-Kosevich temperature dependence factor (Eq. (1.26)) with the effective mass as an adjustable parameter. The best fit masses were $m_A^* = .58 m_0 \pm .05$, $m_{2A}^* = .95 m_0 \pm .05$, and $m_{3A}^* = 1.17 m_0 \pm .06$ (m_0 is the free electron mass). Stark (1967) has previously measured the masses of the γ and A orbits and has reported them to be $m_\gamma^* = .100 m_0 \pm .002$ and $m_A^* = .55 m_0 \pm .02$. The present value for the mass associated with the A peak is consistent with that result, especially if the A peak is interpreted as being a composite consisting of mostly A signal with a small amount of $A+\gamma$ ($m_{A+\gamma}^* = m_A^* + m_\gamma^* = .65 m_0$). Furthermore, this measured mass is additional strong evidence that the A peak cannot be affected very much by MI from any of the sources discussed in the previous paragraphs. The largest MI-induced sidebands of 2A that might be contributing to A are $(2A)A$ and $(2A-\gamma)A$.

From Eq. (3.10), the amplitudes of these sidebands will be proportional to the product of the primary peak amplitudes, and so the Lifshitz-Kosevich temperature dependences of these two sidebands will be $I_{2A} I_A$ and $I_{2A-\gamma} I_A$. (I_r as in Eq. (1.26)). These products produce temperature dependences that correspond to masses of $1.35 m_0$ and $1.26 m_0$, respectively. These are much higher than the measured result, which is a clear indication that these contributions to the A amplitude are insignificant. Similar arguments apply to the (A)T MI peak. Stark (1967) has measured the effective mass of T and found it to be $m_T^* = 0.340 m_0 \pm 0.005$. Using this mass, the product $I_T I_A$ produces a temperature dependence at 48.25 kG that corresponds to an effective mass of $0.69 m_0$. This is sufficiently above the measured result to indicate that the MI-induced (A)T contribution is small compared to the dominant component in the A peak, and this constitutes further evidence that (A)T cannot be causing the remarkable amplitude behavior shown in Fig. 30.

The arguments of the previous paragraph, when applied to the analysis of the 2A peak, do not produce such unequivocal conclusions. The measured mass of the 2A peak was $0.95 m_0$. The predictions of FS theory are for a mass slightly greater than m_0 corresponding to a dominant $2A-\gamma$ amplitude ($m_{2A-\gamma}^* = 1.0 m_0$) with a small contribution of $2A$ ($m_{2A}^* = 1.1 m_0$). The expected mass for the major MI contribution is $0.86 m_0$ (corresponding to the best mass fit to I_A^2). Thus, the low measured mass of the 2A peak is not inconsistent with significant MI-induced contributions to its amplitude. Similarly, the measured mass of the 3A peak was $1.2 m_0$ which is close to the MI result $1.26 m_0$ for $(2A-\gamma)A$. The FS theory expectation is $1.45 m_0$ or somewhat larger.

One final significant feature of the one γ field dependent study that has not been mentioned until now is the high frequency peak that has been labeled BZ on the last three transforms of Fig. 29. This peak is exceedingly interesting for three reasons. First, it is the largest peak in the vicinity in each of the three transforms. Second, it is the only peak in the high frequency region that is stable in frequency and intensity. It is quite reproducible for data sweeps in the 48 to 52 kG range. (We can go no higher than 52 kG with the magnet that was used for this experiment.) Third, it has measured frequency corresponding to 1.246, 1.254, and 1.257 a.u. in the three transforms. In the first of these, it has merged with a second smaller peak of indeterminate origin, and the effect of this will be to move the position of the maximum slightly to lower frequencies. If we estimate this effect to be about 20% of the distance between the two peaks, then the measured area is corrected to 1.248 a.u., and the average of the three is 1.253 a.u. with an rms average of the three deviations of .004 a.u. This result is remarkably close to the area of the Γ KM cross section of the magnesium lattice Brillouin zone. The value of this cross section can be calculated from the length of the reciprocal lattice vector $\vec{G}_{10\bar{1}0}$. This length is 1.2039 a.u. and the corresponding area cross section is $A_{BZ}^{(k)} = 1.255$ a.u.

A Brillouin zone frequency would not be unexpected in magneto-resistance experiments (this will be discussed in Chapter 4), and our first presumption was that this peak was probably a manifestation of eddy currents induced in the sample by the modulation field. However, the signals produced by these effects are $\pi/2$ phase shifted from the

dHvA effects, and hence these can be discriminated against if a good phase null is obtainable on the lock-in amplifier. At 22.5 Hz (the modulation frequency at which all of these studies were done), the ratio of the "in-phase" to "out-of-phase" signal strength was 400. (Even at a modulation frequency of 165 Hz, the ratio was still 100.) We were quite conservative in using modulation frequencies that were sufficiently low to eliminate the possibility of eddy current problems. The high frequency peaks shown in Fig. 29 cannot be due to magnetoresistance effects.

The Brillouin zone frequency has never been seen in dHvA data and is not predicted by FS. Pippard, on the other hand, does anticipate the possibility of Brillouin zone type frequencies coming from the periodic attainment of commensurability between the I-lattice and the O-lattice (discussed in Chapter 1). Pippard reasons along the following lines.

In \vec{k} space, the G orbit circumscribes the basal plane cross-section of the Brillouin zone. If this hexagonal cross-section is transformed to real space in the same manner used for electron orbits (Eqs. (1.6) and (1.7)), the ratio of the two areas will be preserved; the real space free electron orbit will circumscribe the hexagon exactly as in \vec{k} space. This real space hexagon is a unit cell of the O-lattice, and hence, the area $(1/\alpha^2)A_{BZ}^{(k)}$ is the area of the unit cell. In the discussion following Eq. (1.40), it was shown that I-lattice and O-lattice commensurability was attained when every polygon of O-lattice centers encloses integer $2\pi/\alpha$ area. This condition is equivalent to the requirement that half the area of the unit cell is integer $2\pi/\alpha$ area since any polygon of centers can be constructed from elements

that have this area (the area Δ in Fig. 11 is half the area of the unit cell of the O-lattice). The condition for commensurability is thus

$$\frac{1}{2\alpha^2} A_{BZ}^{(k)} = \frac{2\pi n}{\alpha} \quad (3.11)$$

$$n = 1, 2, \dots$$

Solving for the field yields

$$\frac{1}{H} = 2\pi n \frac{e}{\hbar c} \frac{2}{A_{BZ}^{(k)}} \quad (3.12)$$

This is Eq. (1.19) and it can be interpreted similarly. Whatever the effect of incommensurability, the problem reduces to its simplest form in equal increments of H^{-1} given by

$$\frac{\Delta 1}{H} = 2\pi \frac{e}{\hbar c} \frac{2}{A_{BZ}^{(k)}} \quad (3.13)$$

On the basis of this periodic variation (of exactly the same form as that which was encountered in the discussion of the dHvA effect in Eq. (1.20)), Pippard speculated that a dHvA signal with the corresponding frequency

$$2\pi F_{BZ} = \frac{\hbar c}{e} \frac{1}{2} A_{BZ}^{(k)} \quad (3.14)$$

might be observable.

It is possible that the peak labeled BZ in the figure is attributable to this effect. On the other hand, we have not seen evidence of $\frac{1}{2} A_{BZ}^{(k)}$, only its second harmonic. Although there is no theory dealing

with commensurability in sufficient detail to yield a prediction for the ratio of the amplitude of $\frac{1}{2}$ BZ to BZ, it is most often the case in dHvA studies that the fundamental of a given frequency is stronger than the second harmonic.

An additional objection derives from the fact that commensurability simplifies the coupled orbit problem (and the resulting band structure) only because it defines the condition for which all of the various switching junctions are identical. In the case of a crystal misaligned by one degree, the junctions will never be identical, and it is likely that the degree of simplification associated with commensurability will be greatly reduced. In consequence, the amplitude of any associated dHvA signal would be reduced as well, and thus make it even less likely to be observable. These objections lead us to an alternative possible explanation for this peak which will be put forward in Chapter 4.

The temperature dependence of this peak was measured to fit to an effective mass even though there is little reason to suppose that a BZ frequency would follow the Lifshitz-Kosevich temperature dependence (Eq. (1.26)). The measured mass was found to be $1.64 m_0 \pm 0.2$.

The assignment of this peak to BZ is tentative. A firm conclusion about whether or not it is real awaits further experimental investigation.

All of the previous discussion of data in this chapter has been with reference to data sweeps which were too short to resolve frequency components separated by the γ frequency. Ideally, one would like to extend the sweep length over many γ periods and eliminate the

possibility of composite peaks, but the problem with this strategy is that the longer sweep lengths begin to average over field strength dependent changes in amplitudes. If these changes are not very large, then they will be interpreted by the transform as a beat cycle with the periodicity of the overall sweep length. The result will be a slight broadening of the affected peaks in the spectrum; the information regarding such amplitude changes will be lost. The field dependent study to be described in the following paragraphs was done with five γ period sweep lengths, and this appears to have been a good compromise choice.

Figures 31 and 32 show the results of a series of five γ period field sweeps, each of whose starting field is five γ periods above the ending field of the previous sweep. The temperature was $.3^{\circ}\text{K}$ throughout, and the first maximum of $J_2(x)$ was held at $.65$ a.u. (well off the display to the right). The display format is the same as for Figs. 27 to 29 in that starting fields and the maximum peak intensities are listed, and the vertical scales have been adjusted so that the largest peak on each transform is always the same height. The complex of peaks in the middle of each display is the A complex now greatly spread out by the increased resolution of the transform.

Probably the most striking feature about this series is the volatility of the A complex: once again we have behavior that is qualitatively different from the predictions of FS theory. The complex of peaks appears to spread apart and coalesce in a periodic manner. The maximum intensity is much larger when the complex is well localized in frequency. This periodic collapse onto a single frequency and the accompanying concentration of spectral power in a single peak is

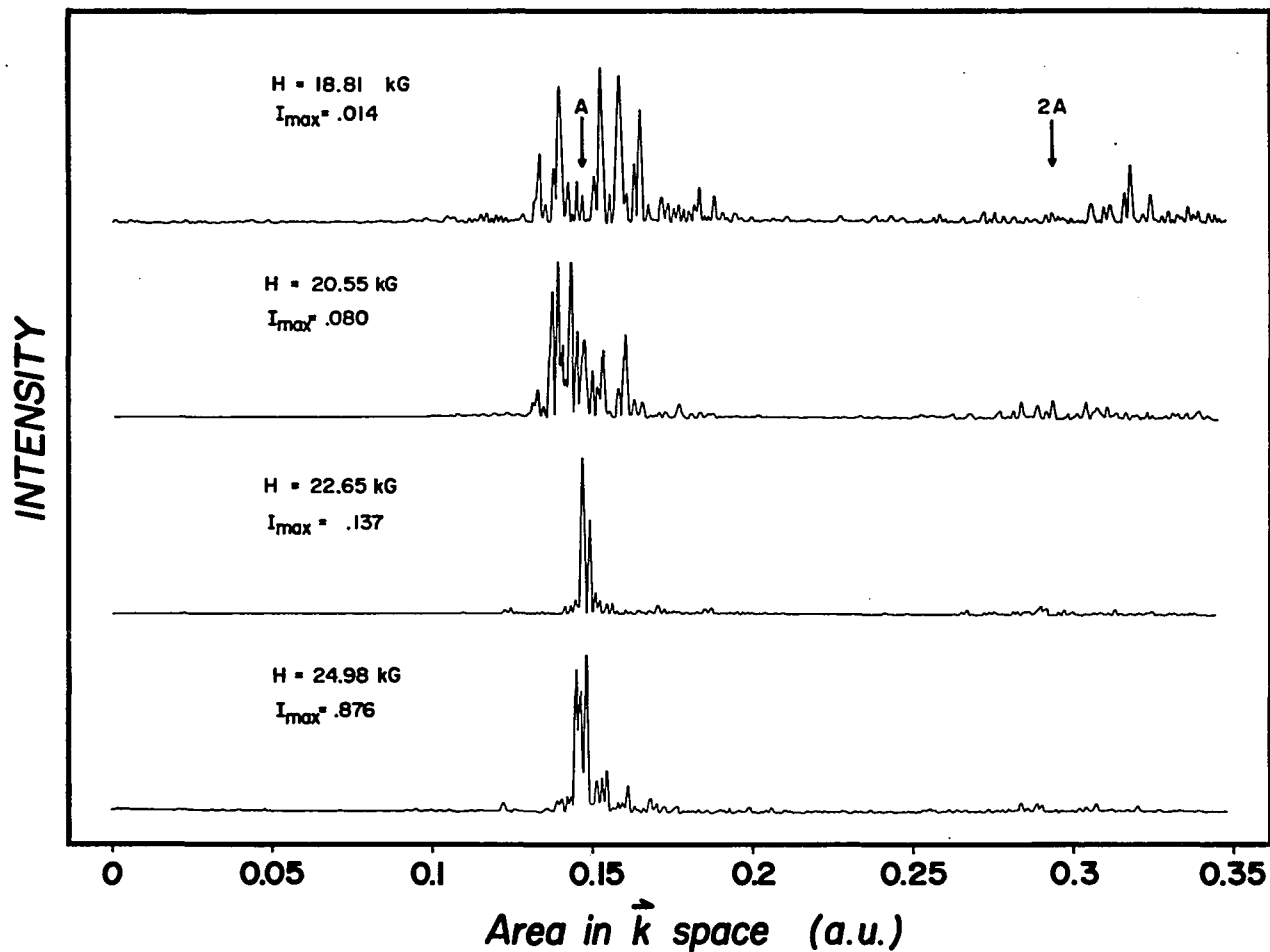


Fig. 31. Magnetic field dependence of coupled orbit dHvA spectra IV

These spectra are the results of Fast Fourier Transform of data produced by five γ period field sweeps and sampled 2048 times. The temperature is constant 0.3°K and the first Bessel function maximum is at 0.65 a.u.

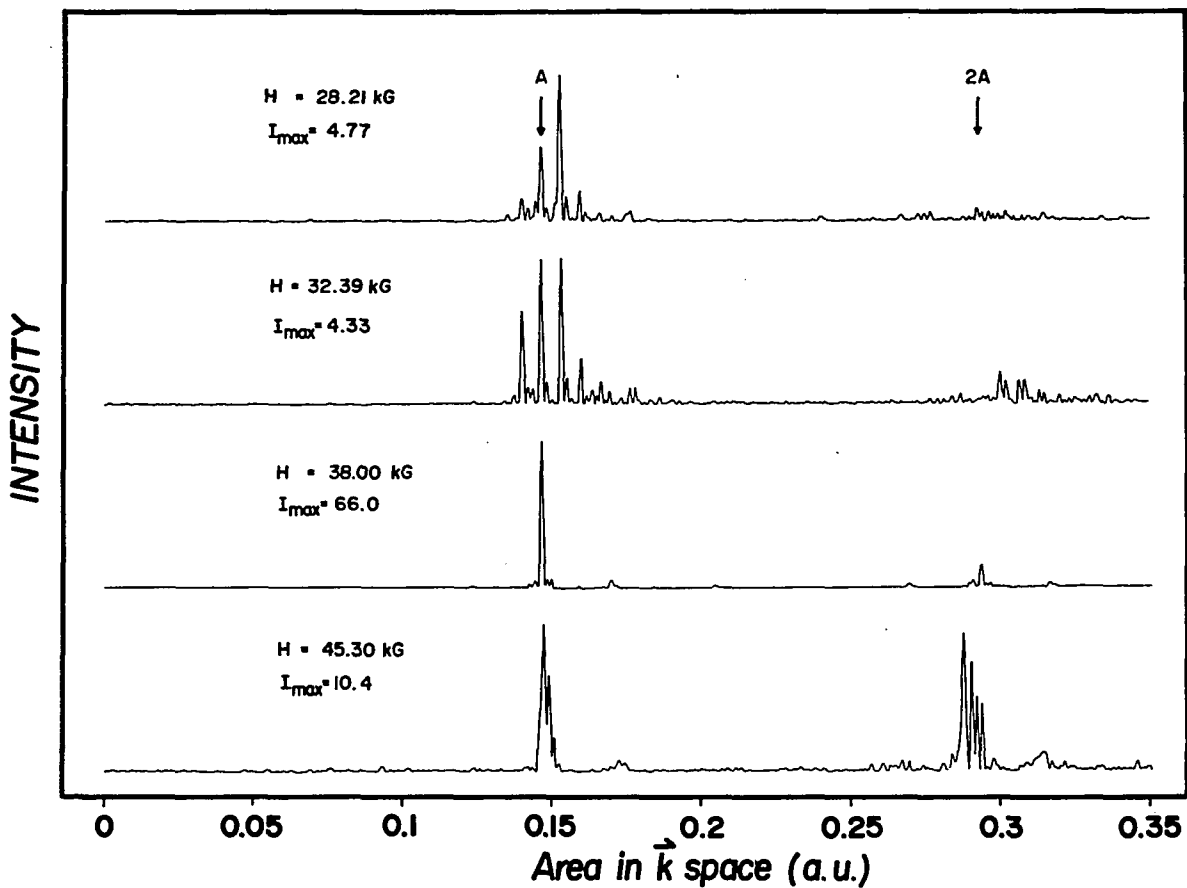


Fig. 32. Magnetic field dependence of coupled orbit dHvA spectra V.

These spectra are the results of Fast Fourier Transform of data produced by five γ period field sweeps and sampled 2048 times. The temperature is constant 0.3°K and the first Bessel function maximum is at 0.65 a.u. This figure is a higher field continuation of Fig. 31.

responsible for the amplitude behavior displayed in Fig. 30. In the last four sweeps of the series, the structure of the complex is quite well defined; one peak in particular is present at all four field strengths and is remarkably stable in frequency. On this basis, it can be attributed to the A orbit. The measured frequency of this peak is $.1463 \pm .0006$ a.u. In the 38.00 kG sweep, the multiple sidebands have totally disappeared, and it is possible to see the L sidebands on A and on 2A. The four small sidebands are spaced from the central peak by $.0232 \pm .0006$ a.u., and this corresponds very well with the previously measured result ($.0234$ a.u. from Stark 1967). The small (A)L sidebands are another indication of the scale of MI coupling between the A and L peaks.

Most of the structural change in the A complex is due to the coming and going of several equally spaced principal peaks. These are interesting not only because of the way they appear and disappear but also because they extend below A where no peaks are predicted by the theory. In the 18.81, 28.21, and 32.39 kG sweeps, there is clear indication of an A- γ peak for which there is no corresponding simple closed orbit. In the 18.81 kG sweep, there is what appears to be A-2 γ . These identifications have to be considered tentative because MI effects are playing a role. When the separation between the principal peaks is averaged for those sweeps where they are clearly defined, the result is $.00642 \pm .0006$ a.u. This is much closer to T than to γ , although the two cannot be resolved for this sweep length. MI coupling between A and T is probably contributing significantly to the A- γ peak, but this cannot

explain the periodic tendency to disappear since the T amplitude is found to be constant in the field range of the last four data sweeps.

Another feature of these data is the pronounced tendency for peaks whose spacing is significantly less than the γ frequency. In the 18.81 and 32.39 kG sweeps, these "extra" peaks are small sidebands of the principal peaks in the complex. These cannot be confused with windowing effects for two reasons. First, they are much too large. Sidelobes associated with the sampling window are much smaller, really only becoming visible when the spectra are displayed as amplitude rather than intensity. Second, the sidelobes are observed to grow and dominate the spectrum for certain values of the field. This is demonstrated clearly in the two neighboring field ranges at 22.65 and 24.98 kG. In the former transform, the A complex is dominated by peaks at .147 and .149 a.u., and in the latter transform the peaks are at .145, .146, and .148 a.u. This behavior is quite typical of the data in general. For example, some spectra we have obtained (not part of this particular series) show the A complex to be a series of equally spaced peaks all of approximately the same intensity but spaced in frequency by $\frac{1}{3}\gamma$ (similar in appearance to the A complex shown in the 32.39 kG transform only with the denser spacing). This cannot be an MI effect. The only dHvA frequency component low enough to produce $\frac{1}{3}\gamma$ MI sidebands is μ , and this component is too weak to be detected except in the low field limit (2 to 10 kG).

These shifts in spectral intensity are not the result of field sweep nonlinearity. Any departures from a strictly linear sweep would not show up in the data because the signal sample was triggered by repetitive sampling of the field. Any nonlinearity in the field

detection apparatus would not smear the frequencies in such a reproducible and field dependent manner. Spectra such as those shown in Figs. 31 and 32 were found to remain stable for 10 to 20 sweeps taken over several days as long as the magnetic field was returned to the same value. (The field was shut off completely every night.)

The frequency instability evident in Figs. 31 and 32 is characteristic of fourier transform interpretation of spectral components that are changing frequency during the sampled sweep. Any such interpretation conflicts fundamentally with the association of dHVA frequencies with simple closed semiclassical orbits on the coupled orbit system.

The data presented in this chapter do not agree with the predictions of the existing theory. There is ample qualitative evidence to support this conclusion even though MI effects have played a spoiler role in that they rule out more quantitative demonstrations. These effects can be brought under experimental control, and this will be actively pursued in a forthcoming experiment. One approach to the problem would be to take additional advantage of newly available computer control technology. If an independent sensor were placed sufficiently close to a regularly shaped Mg sample, it might be possible to infer the B field within the crystal. This information could be fed back into a computer which could be programmed to step the magnetic field in equal increments of B^{-1} rather than H^{-1} . Under these conditions, the MI effects would be eliminated at the source, and dHVA experiments involving systems with complicated spectra could be pursued to much lower temperatures.

The purpose of this chapter has been to report data that conflicts with the existing theory for the dHvA effect of the coupled orbit system. The next chapter will describe results of band structure model calculations which suggest possible explanations for the disagreement.

CHAPTER 4

INTERPRETATION OF THE DATA

In this chapter, a number of computer model calculations will be described and the results discussed. These calculations are based upon Pippard's band structure given by Eq. (1.56). They were undertaken for two reasons. First, the data produced by this experiment are in substantial disagreement with FS, and we wanted to know the extent of disagreement with Pippard, if any. Second, it is clear from Fig. 14 that the width of a particular band is critically dependent upon the relative positions of the local G and H levels and the proximity to the nearest γ level. Furthermore, every band associated with a G level on the right side of the diagram clearly associates with a particular H or γ level on the left side. Since each of these three series of levels evolves through the Fermi surface at a different rate (given by the three dHvA frequencies F_G , F_H , and F_γ) as the field is changed, there must be a consequent shearing of the bands as a given G level becomes disassociated with the opposite H (or γ) level and reassociated with the next level in line. This shearing effect will cause the bands to undergo dramatic changes in width that will occur very rapidly as the G levels approach exact alignment. Field dependent changes in the density of states of this kind would normally be expected to produce corresponding changes in the Fourier transform of the density of states. Since each Fourier component corresponds to an effective mass value, this would

indicate the possibility of field dependent intensities for the dHvA signals corresponding to these effective masses or, equivalently, to signals which do not correspond to simple closed semiclassical orbits. Such a field strength dependence is in conflict with FS theory and might be found to explain the "extra" peaks and strong field strength dependence observed in our data.

Before considering the effects of band shearing on the density of states, it is fruitful to consider first the special case, discussed in Chapter 1, where the field H is held fixed and the H dependent terms ϕ_i^0 given by Eq. (1.57) have been dropped. Under these conditions, the simpler Eq. (1.59) defines the band structure and Fig. 14 is a graphical display of its form. When H is fixed, q is constant ($p^*p+q^*q = P+Q = 1$ and Eq. (1.5)), and the density of states will correspond to a vertical cut through the Fig. 14 band structure at the chosen value of q . Since \vec{k} space is two dimensional for the coupled orbit problem, the number of \vec{k} states per unit area in \vec{k} space is the constant $A/(2\pi)^2$ where A is the area extent of the coupled orbit system (the cross-sectional area of the crystal). The density of states can thus be determined by calculating the amount of area in \vec{k} space which corresponds to the x interval x to $x+dx$. (The quantity x is defined in Eq. (1.51). It is the energy variable of Eq. (1.59).) This is accomplished through the intermediary quantity C defined in Eq. (1.58). The \vec{k} state Brilluoin zone (Fig. 13) is first divided up into a fine mesh of allowed \vec{k} states. Since $\omega_i = \vec{b}_i \cdot \vec{k}$ these can be used in Eq. (1.58) to calculate C for each value of \vec{k} and in this way count the number of \vec{k} states that correspond to values of C in the interval C to $C+dC$. This is a straightforward

computer calculation and the result is shown in Fig. 33. Most of the states within the Brillouin zone are concentrated in the vicinity of the contour corresponding to $C = -1.0$ shown in Fig. 13.

The C dependent density of states $\eta(C)$ can be used to calculate $\eta(\mathcal{E})$ for any \mathcal{E} (or equivalently x) simply by choosing a value of \mathcal{E} and computing the right hand side of Eq. (1.59). The result is a value of C . If this C is such that $3.0 \geq C \geq -1.5$, then $\eta(C)$ is used to determine $\eta(\mathcal{E})$. If C is outside of the interval, then the density of states for that value of \mathcal{E} is zero. It is convenient to parameterize the function $\eta(C)$ for easy reference by computer programs that calculate $\eta(\mathcal{E})$. The parameterization used in our programs was the result of a fit of $\eta(C)$ to a fifth degree polynomial in each of three regions. The polynomials were each of the form

$$\eta(C) = a_0 + a_1C + a_2C^2 + a_3C^3 + a_4C^4 + a_5C^5. \quad (4.1)$$

The a_i 's are given for each of the three regions in Table 2.

Figure 34 shows a section of the model density of states $\eta(\mathcal{E})$ that has been calculated in the manner just described. The characteristic profile of Fig. 33 is visible in most of the bands, although modified to a greater or lesser extent depending upon the individual band width. Each band must include the same number of \vec{k} states so each peak has been normalized to enclose the same area. The narrow bands that are only a few points wide begin to resemble δ functions.

In dHvA studies of the coupled orbit system, it has been traditional to associate the oscillatory magnetization signals with simple closed semiclassical trajectories. As a consequence, the theoretical

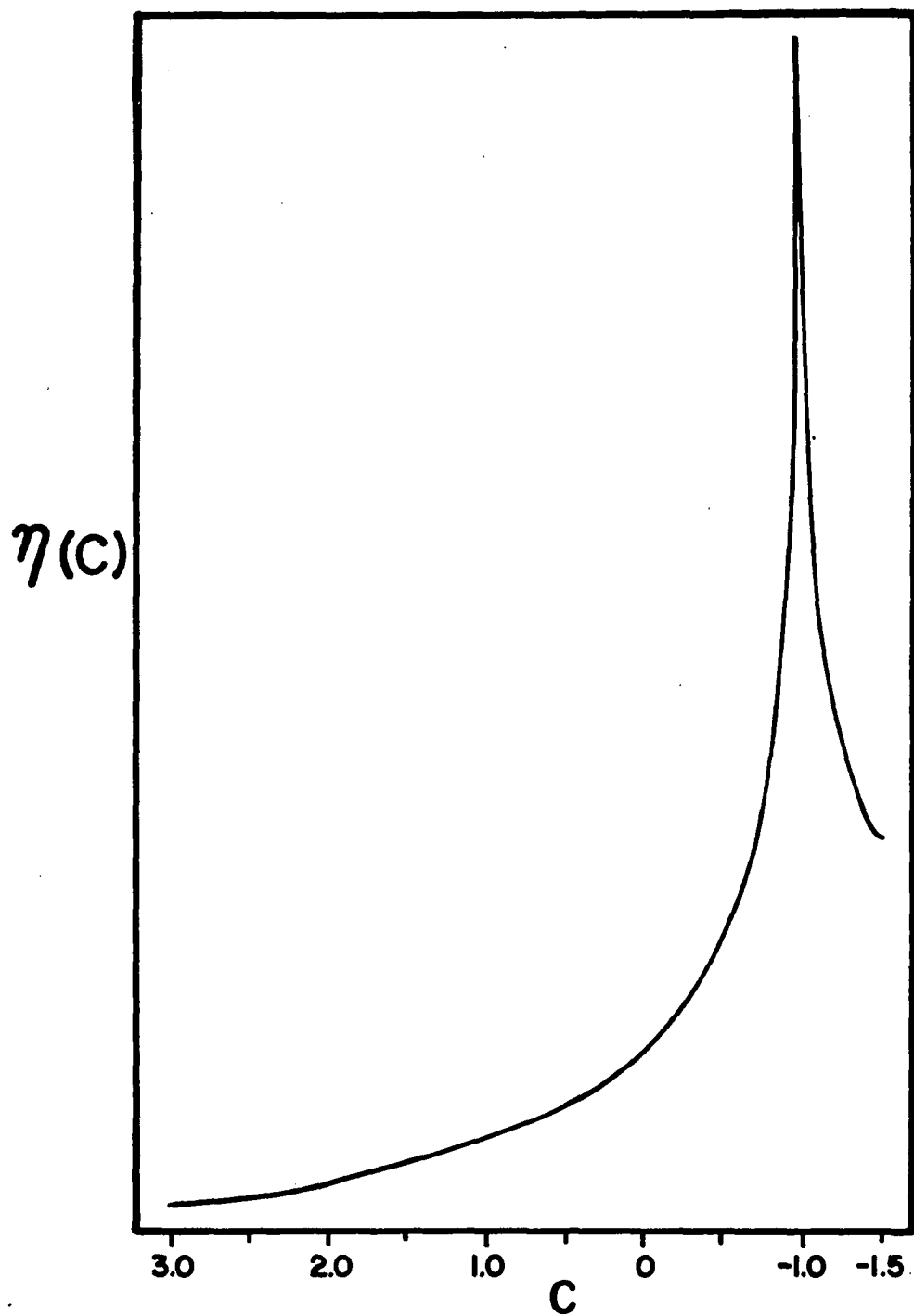


Fig. 33. The density of \vec{k} states $\eta(C)$ as a function of C within a single band.

TABLE 2. Fit parameters for three-segment fifth degree polynomial representation of $\eta(C)$.

Polynomial Coefficient	Range of C		
	$-1.5 \leq C \leq -1.0$	$-1.0 \leq C \leq .746$	$.746 \leq C \leq 3.0$
a_0	9.913	-2.3152440×10^4	4.3744822×10^5
a_1	-5.497	-1.7561777×10^5	1.7068321×10^6
a_2	3.682	-5.2353390×10^5	2.6603304×10^6
a_3	-1.931	-7.7045048×10^5	2.0686013×10^6
a_4	0.5667	-5.5965888×10^5	8.0220665×10^5
a_5	-0.06617	-1.6074411×10^5	1.2410438×10^5

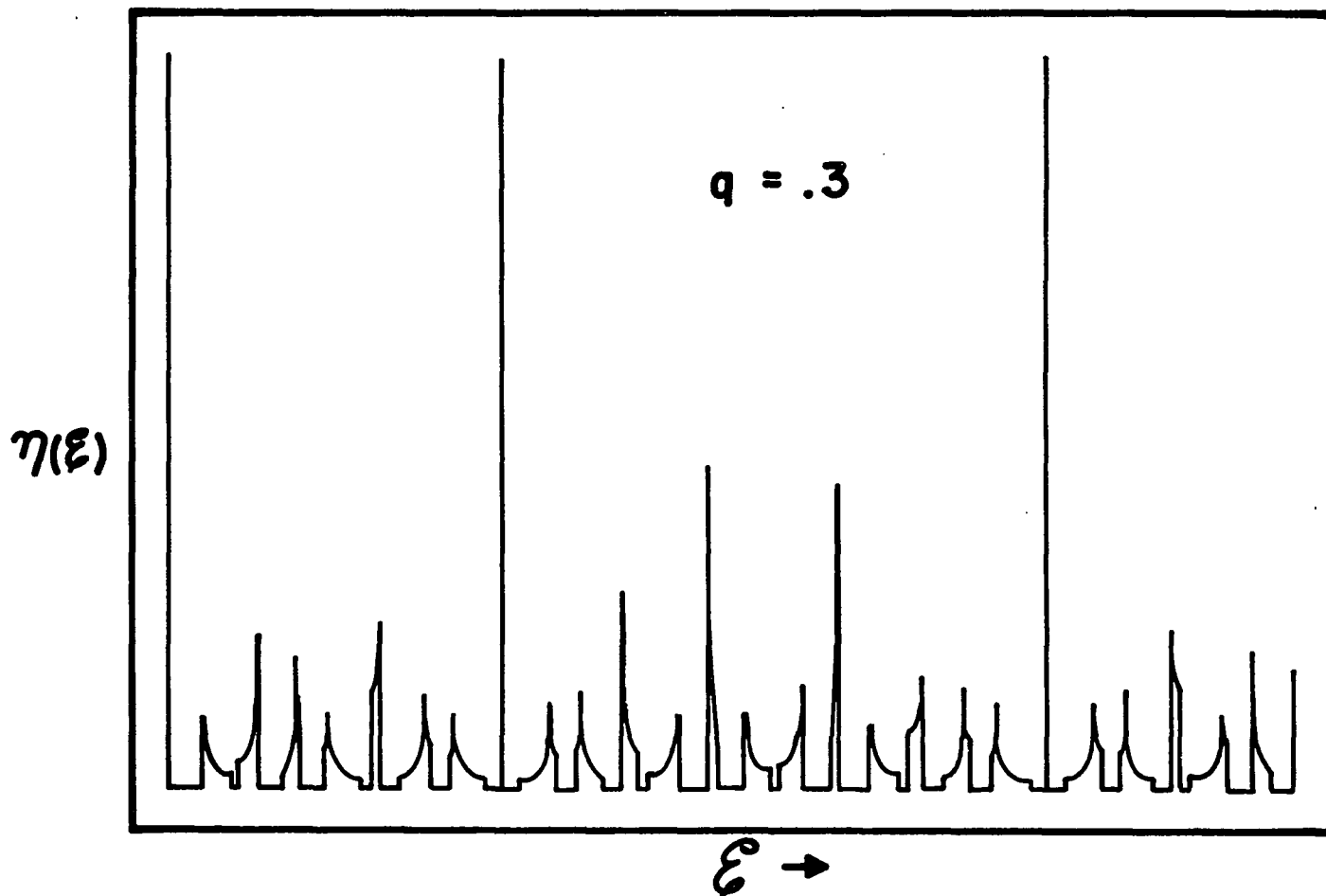


Fig. 34. The coupled orbit density of states calculated from Pippard's band structure. All of the bands have been normalized to enclose the same area. Each band represents the same number of states.

investigations of the system have tended to rely upon the behavior of one, or a select few, spectral components of the density of states, which correspond to such orbits, as an adequate test of validity. (Falicov and Stachowiak 1966, Ruvalds 1969.) Having the capability to perform broad band spectral analysis of experimental data, it is natural that we take a more general approach and apply these same techniques to the model band structure. The calculated Fourier transform provides all of the spectral intensities of the density of states and, therefore, constitutes a sound qualitative test of the agreement between the FS theory of simple closed orbits and the band structure theory of Pippard.

Figures 35 and 36 show the Fourier transform of the coupled orbit density of states for eight values of the Bragg reflection parameter q . The transforms corresponding to the limiting cases $q = 0$ and $q = 1$ are not shown since they are easy to infer. For $q = 0$, the density of states is a series of δ functions separated by $\hbar\omega_G$. Since $\hbar\omega_G = \hbar eH/m_G^*c$, the Fourier transform will be a series of δ functions spaced apart by $m_G^*c/\hbar eH$, or equivalently, there will be spectral components corresponding to m_G^* , $2m_G^*$, $3m_G^*$, The $q = .10$ display, shown at the bottom of Fig. 36, is clearly approaching this limit. For $q = 1$, the density of states is two series of δ functions spaced apart by $\hbar\omega_\gamma$ and $\hbar\omega_H$ (H and γ are the only possible orbits when $q = 1$), and the transform of this double series will have spectral components corresponding to m_γ^* , $2m_\gamma^*$, $3m_\gamma^*$, ... and m_H^* , $2m_H^*$, $3m_H^*$, Since the repetition period of the band structure corresponds to 186 H levels and only 15 γ levels, we expect the amplitude of the γ Fourier component to be down from the H Fourier component by the factor $15/186 = .081$. For the first transform in Fig. 35,

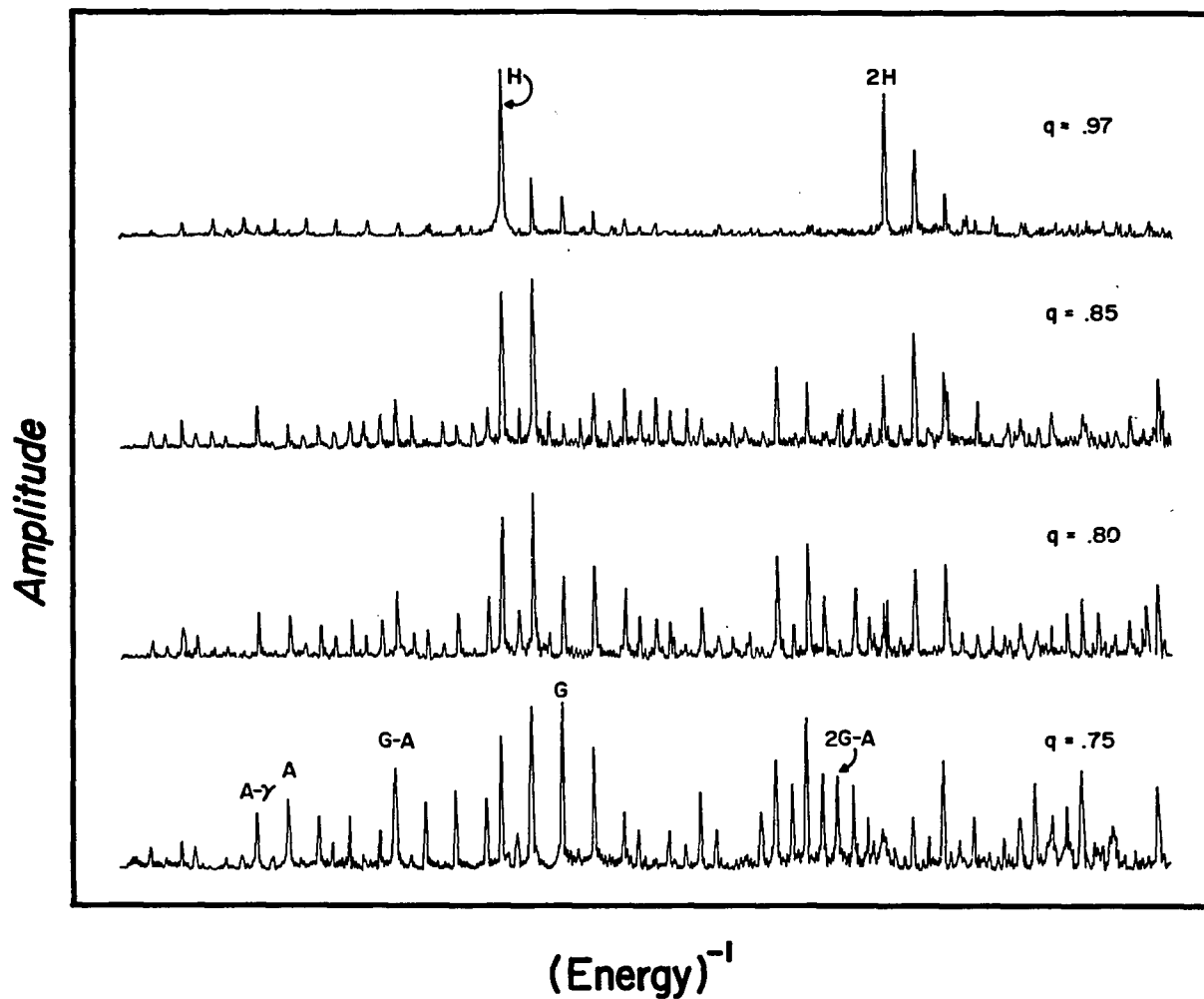


Fig. 35. Fourier transform of the model density of states $\eta(\epsilon)$ for high values of q .

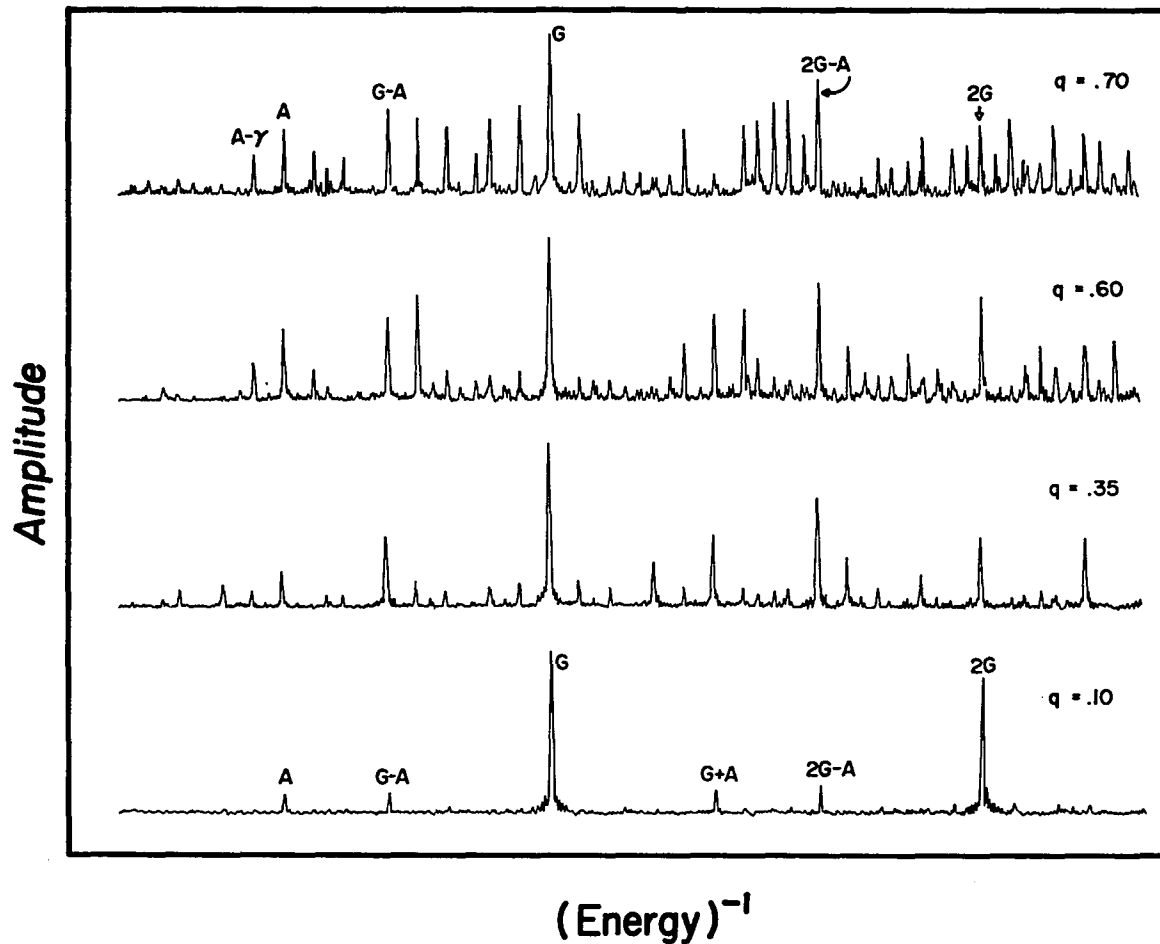


Fig. 36. Fourier transform of the model density of states $\eta(\epsilon)$ for intermediate and low values of q .
 This is a continuation of Fig. 35.

corresponding to $q = .97$, this ratio is .079 which is clearly approaching this limit.

Note that the peaks have been assigned orbit labels even though it would be more rigorously correct to label them as masses (m_H^* , $2m_H^*$, $m_{A-\gamma}^*$, etc.). In any case, the labels are often not unique. For example, the mass of orbit G is the same as the mass of $H+2\gamma$. (Each is made up of six long path segments and six short path segments. See Figs. 4 and 15.)

It is worthwhile to emphasize that these spectra are fundamentally different from those displayed earlier (for example, in Figs. 31 and 32) in that these deal with periodicities in energy whereas the earlier transforms displayed periodicities in H^{-1} . The discussion that follows will make references to both of these kinds of periodicity.

Finally, the spectra are displayed in amplitude format rather than as intensities. The small "noise" peaks that rise on either side of the larger peaks are due to the windowing effects that are much easier to see when the transform is displayed in this format.

Many of the spectral components in the various transforms correspond to masses that can be associated with simple closed orbits, but there are others that cannot. Among these are the peaks labeled A- γ and G-A. The first of these peaks represents the mass that corresponds to a propagation time appropriate for two long path segments and one short segment. There is no simple closed semiclassical orbit that can be constructed from these path segments. The same is true of the G-A peak corresponding to a propagation path consisting of four long segments and two short segments. The fact that there are Fourier components of

Pippard's density of states that do not correspond to effective masses that can be attributed to simple closed orbits is a clear indication that the FS theory and the model band structure of Pippard are in qualitative disagreement.

It is not obvious that an A- γ Fourier component in the density of states would give rise to an A- γ periodicity in the dHvA signal since it is not clear how fast the A- γ spectral component of the density of states would evolve through the Fermi surface as the field is changed. We no longer have the intermediary of a simple closed orbit to make the association between the energy periodicity (the path length around the orbit) and the rate at which the levels move to higher energy with changing field (the enclosed area of the orbit).

On the other hand, it appears likely that a propagator theory of the coupled orbit system that agreed with Pippard's band structure would include contributions from interfering propagators in the manner demonstrated in earlier work on the linear chain model of magnetoresistance quantum interference oscillations (Stark and Reifenberger 1977). If that approach is correct in the present context of the dHvA effect, then the mass associated with an interfering pair of orbits would be expected to correspond to the difference in their orbital path lengths. The area to use in computing the magnetic field periodicity would be the difference in their enclosed areas. A theory constructed along these lines would reestablish an association between path length and enclosed area in such a way that an A- γ spectral component in the density of states would produce a corresponding A- γ periodicity in the dHvA signal.

Figure 37 shows two simple, closed, semiclassical orbits (G and G+A- γ) and the interfering combination of these which would be expected to produce an A- γ dHvA frequency with an associated A- γ effective mass. In the FS theory, there can be no effects arising from interferences between orbits (a) and (b) even when they are spatially coincident over most of the length of the orbital path, as in (c). (There is a single closed orbit that resembles (c) consisting of a single long path that extends twice around G and once around the protruding part of A, but this corresponds to frequency and mass 2G+A- γ which are quite different from frequency and mass A- γ).

The fact that our data shows evidence of an A- γ frequency, as well as a general tendency not to cut off in spectral intensity immediately below A and G, coupled with the fact that these same features are also evident in the spectra of Figs. 35 and 36, is an indication of the direction that further theoretical work on this problem should take.

The question of compatibility with Pippard's model band structure was not overlooked by FS. They chose to compare the two theories on the basis of the q dependent behavior of a single spectral component of the density of states; they compared the predicted amplitudes of the G peak. Figure 38 shows the results that are obtained when we repeat this comparison. The black dots represent the G amplitudes derived from Pippard's band structure. The numbers were produced by simply recording the amplitude of the G peak on a series of full spectrum transforms like those shown in Figs. 35 and 36. The curve on the display represents the prediction of the FS theory. It can be calculated quite simply by adding up all of the MB terms of the form $(6m_j/D_j \ell_j)R_j$ for all of the

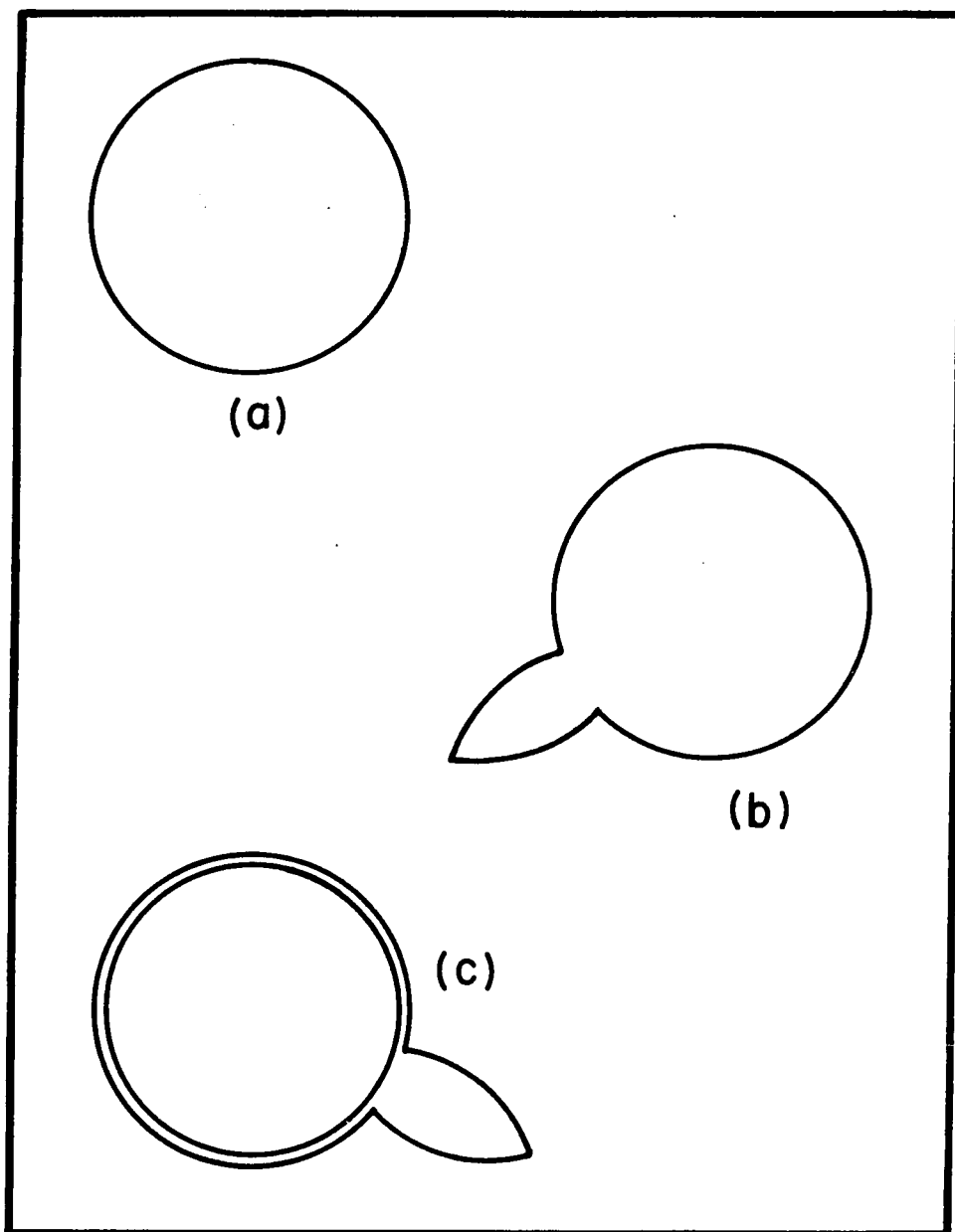


Fig. 37. Two simple closed orbits (a) and (b), and the interfering combination of these (c) which would be expected to produce an A- γ frequency and mass.

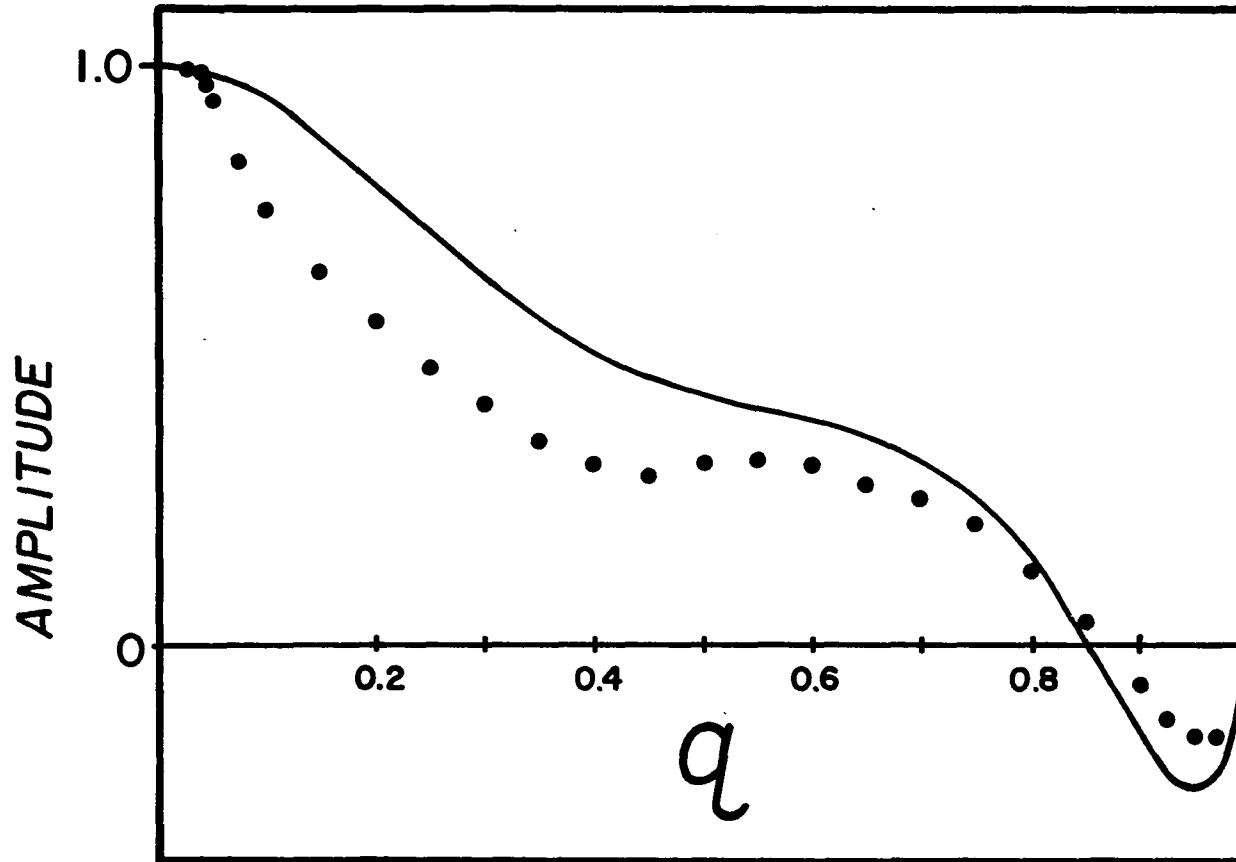


Fig. 38. The q dependence of the amplitude of the G peak in the coupled orbit density of states.

The dots represent the predictions derived from Pippard's band structure. The solid line represents the prediction of the FS theory.

closed orbits that have the mass of G . (This term was discussed in Chapter 1 after Eq. (1.64).) The closed orbits that have the mass of G are shown in Fig. 15. These are the orbits that are made up of six long and six short path segments, and they include four orbits of the type $3A-2Y$, four orbits of the type $H+2Y$, as well as G itself. (Note that these nine orbits will produce three different dHvA frequencies even though they all have the same mass. This is because the three types of orbit each enclose a different area.)

Figure 38 shows there is some degree of qualitative agreement between the predictions of the two theories for this single spectral component but certainly not to an extent that invites one to conclude that the two theories confirm one another. Since the foregoing discussion showed Pippard's band structure to produce spectral components that the FS theory did not, Fig. 38 is most reasonably interpreted as further evidence of quantitative disagreement between the two theories.

For the purposes of calculating the 25 amplitudes shown in Fig. 38, the density of states was represented by 4096 points. (Since there are 216 bands in the repetition period, this amounts to an average of about 19 points to represent each band.) If this number is increased to 8192 points, the results do not change very much. But when this is reduced to 1024 points (about five points for each band), the G amplitude is found to follow the curve much more closely. It is, perhaps, not surprising that FS found the two theories to agree quantitatively, since they made their comparison at a time when it was probably necessary to carry out the calculation on a coarse grid of points. (The Fast Fourier Transform algorithm was only invented in that year, and computers were

much slower.) In any case, the results of Fig. 38 are a further indication of disagreement between the FS theory and the band structure model of Pippard.

Although the theoretical models of the density of states are useful for comparing the two theories and, perhaps, conclusive in the determination that they are different, the more important comparisons occur at the level of predicting the harmonic content of the dHvA signal since this is what is measured in the laboratory. In the case of the FS theory, these predictions are already in hand (Fig. 16) since FS carried their analysis almost to a measurable result in their original paper. For Pippard's band structure model, the problem is not nearly so simple. In principle, the problem is straightforward. The density of states (Fig. 34) is calculated for many closely spaced values of the magnetic field, the result is integrated over energy to arrive at the free energy (Eq. (1.18)), and then that result is differentiated with respect to H to get the magnetization. The complications arise when a realistic H dependence is included in the density of states. The density of states shown in Fig. 34 was calculated from the band structure Eq. (1.59) and does not change form at all in response to changes in H . The only effect of increasing H is to cause the entire pattern to expand to higher energies. This H dependence would result in some kind of dHvA effect because the various peaks would evolve through the Fermi surface in order and, hence, contribute to an oscillatory free energy. However, this approximation does not really do justice to Pippard's model because it ignores an essential feature of the problem: the G levels do not move to higher energy at the same rate as do the H levels or the γ levels. If all of

the bands are assumed not to change form, then all of the spectral components of the density of states must be phase locked to one another and must move to higher energy at the same rate. If this is so, then they will each produce a dHvA frequency that is strictly proportional to their energy frequency, or in other words, proportional to their mass. This model would predict that the dHvA frequencies associated with any two orbits would have the same ratio as the associated effective masses. This is, of course, not true. (For example, the ratio $m_G^*/m_A^* = 2.64$ while the ratio of the frequencies corresponding to the G and A orbits is 11.6).

In order to derive a realistic dHvA effect from Pippard's model, it is necessary to include the shearing of the G, H, and γ levels. This means that the ϕ_i^0 terms that were dropped in going from Eq. (1.56) to (1.59) must be retained. The ϕ_i^0 terms are defined in Eq. (1.57). Using the Onsager relation (Eq. (1.21)), these may be rewritten in more convenient form.

$$\begin{aligned}
 \phi_1^0 &= \frac{2\pi}{H} \left(F_{BZ} + F_\gamma - \frac{1}{2}F_H \right), \\
 \phi_2^0 &= \frac{2\pi}{H} \left(\frac{3}{2}F_{BZ} - \frac{1}{2}F_H \right), \\
 \phi_3^0 &= \frac{2\pi}{H} \left(2F_{BZ} - F_\gamma - \frac{1}{2}F_H \right), \\
 \phi_4^0 &= \frac{2\pi}{H} \left(\frac{2}{3}F_{BZ} - \frac{1}{3}F_\gamma - \frac{1}{6}F_H \right), \\
 \phi_5^0 &= \frac{2\pi}{H} \left(\frac{F_A}{2} \right),
 \end{aligned} \tag{4.2}$$

where F_H , F_γ , and F_A are the dHvA frequencies associated with the H, γ ,

and A orbits, and F_{BZ} is the frequency corresponding to the basal plane cross-section of the Brillouin zone.

Figure 39 shows a series of four views of the density of states derived from Pippard's band structure when these H dependent terms have been included (Eq. (1.56)). The vertical scale is constant on the four plots; for display purposes, the narrow peaks have been cut off when they extend above the height of a single plot. The magnetic field has been increased by 1/10 G between each calculation. A number of the individual bands change width dramatically even for these very small changes in the magnetic field. This occurs when a G level on the $q = 0$ side of the band structure (Fig. 14) overtakes an H or γ level on the opposite side of the diagram. When a pair of levels approaches the point of being coincident in energy, the band between them can become very narrow and then widen once again as the resonance condition is passed. These changes can occur very rapidly as is demonstrated by the behavior of the band marked P in the figure.

The dHvA effect can be calculated directly from this field dependent sequence of density of states functions. Each numerical list of numbers is integrated as indicated in (1.18), and the result is the field dependent oscillatory free energy. This calculation has not yet been done. It will be an expensive calculation for a variety of reasons, and the amount of program development required would have carried the project beyond the possible bounds of this dissertation.

Without having done the complete calculation, it is difficult to be certain what effects the field dependent density of states shown in Fig. 39 will produce in the dHvA effect. However, the fact that the

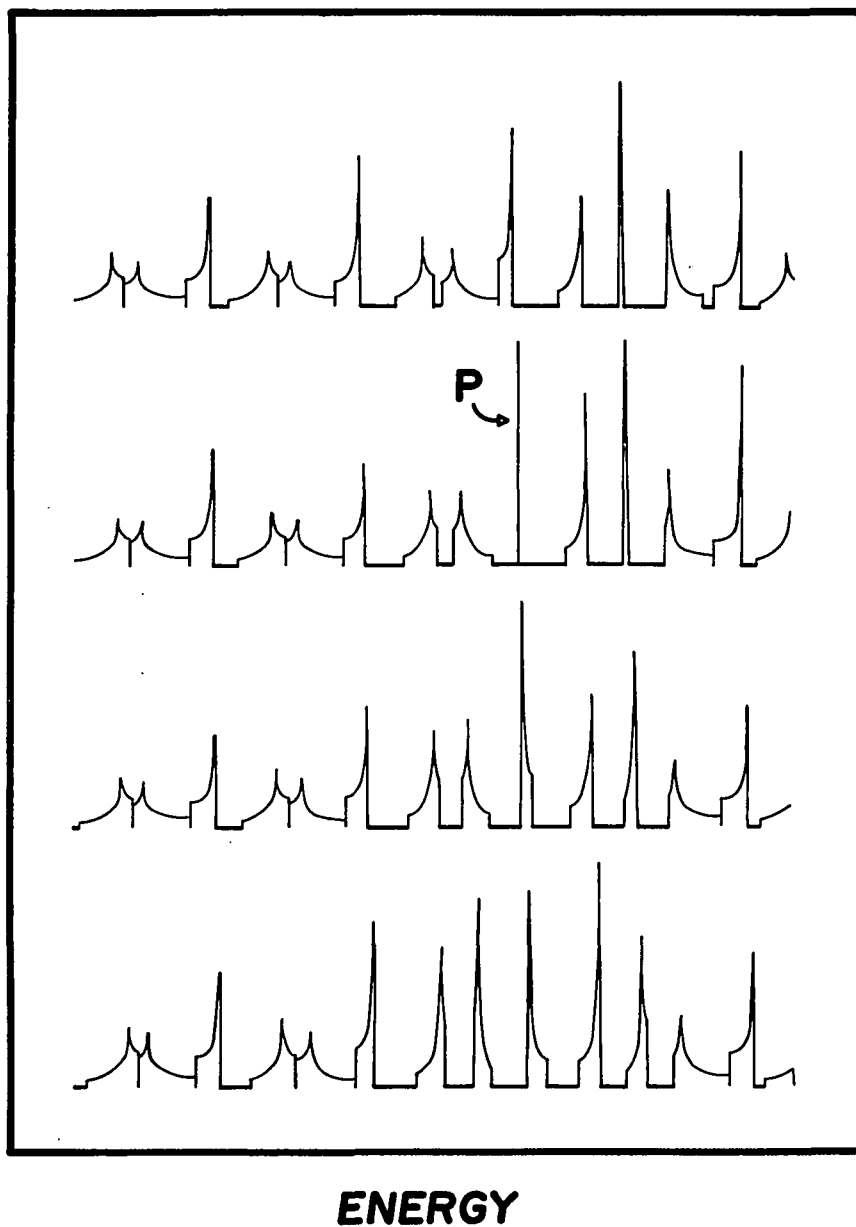


Fig. 39. A section of the model density of states $\eta(\epsilon)$ shown at four closely spaced magnetic field strengths.

The field has been stepped by $1/10$ G period between each snapshot. The vertical scales of the four segments are the same. The narrow peaks occur whenever G and H levels line up. These have been cut off for display purposes when they extend above the maximum height of a segment.

bands tend to become very narrow and broad again quickly, compared to the rate at which the G levels move to higher energy, is an indication that there ought to be rather strong high frequency components in the dHvA effect whenever this narrowing occurs near the Fermi surface. These frequencies should start to become observable when kT gets to be less than the band spacing (for example, about 2°K at 30 kG), and this would seem to indicate the possibility of high frequency magnetization oscillations with abnormally weak temperature dependence or, equivalently, abnormally low effective masses. This result would conflict with the FS theory since the mass must scale with the frequency for any single closed orbit. There has already been some experimental indication that these high frequencies exist. A number of years ago Stark (1977) observed frequencies as high as 10 to 12 G at 1°K . (We were able to find frequencies no higher than 4 G in this experiment, but this is not surprising due to the residual misalignment of the crystal.)

The model calculation and the experiment must both be pursued in the future. In the event that both confirm our present expectations, the evidence will be very strong that we have entered a regime of crystal purity where a band structure description of the coupled orbit system is necessary: where it is no longer possible to establish a one-to-one correspondence between the harmonic components in the dHvA signal and simple closed semiclassical orbits.

A last bit of evidence that seems to argue in favor of counting interferences between closed semiclassical orbits is the Brillouin zone peak discussed in the previous chapter. Although there is no single closed orbit that enclosed the Brillouin zone area, it is quite easily

obtained in a theory that counts interferences due to area differences between two orbits. A good example of this is the area difference between G and the orbit labeled $[3A-2\gamma]_2$ in Fig. 15. An objection to this interpretation is the fact that any number of frequencies in the vicinity of the BZ peak can be derived by taking similar differences between orbits. It is not immediately clear why the BZ area would give rise to a frequency component that was stronger and more stable than any of the rest of these. However, there may be an explanation for this.

Figure 40 shows the two difference paths that enclose the real space area $A_{BZ}^{(r)}$. (The area bounded by the two paths is the same as the unit cell area $A_{BZ}^{(r)}$ which is indicated by the dashed line hexagon.) It is useful to consider a pair of closed orbits which follow identical paths before point a and after point b but which separate as shown between the two points. If the amplitude and phase of the wave functions on the two orbits sum to unity at point a, then the amplitude and phase at point b will be given by

$$\psi_b = p^4 q^2 (e^{i\phi_1} + e^{i\phi_2}), \quad (4.3)$$

where ϕ_1 and ϕ_2 represent the two different phases picked up along the upper and lower paths, respectively. Since the lower path encloses the additional area $A_{BZ}^{(r)}$, the phase ϕ_2 will be related to ϕ_1 by $\phi_2 = \phi_1 + \epsilon$ where $\epsilon = \alpha A_{BZ}^{(r)}$. Hence we may write

$$\psi_b = p^4 q^2 e^{i(\phi_1 + \epsilon/2)} (e^{i\epsilon/2} + e^{-i\epsilon/2}) \quad (4.4)$$

and the intensity at point b will be given by

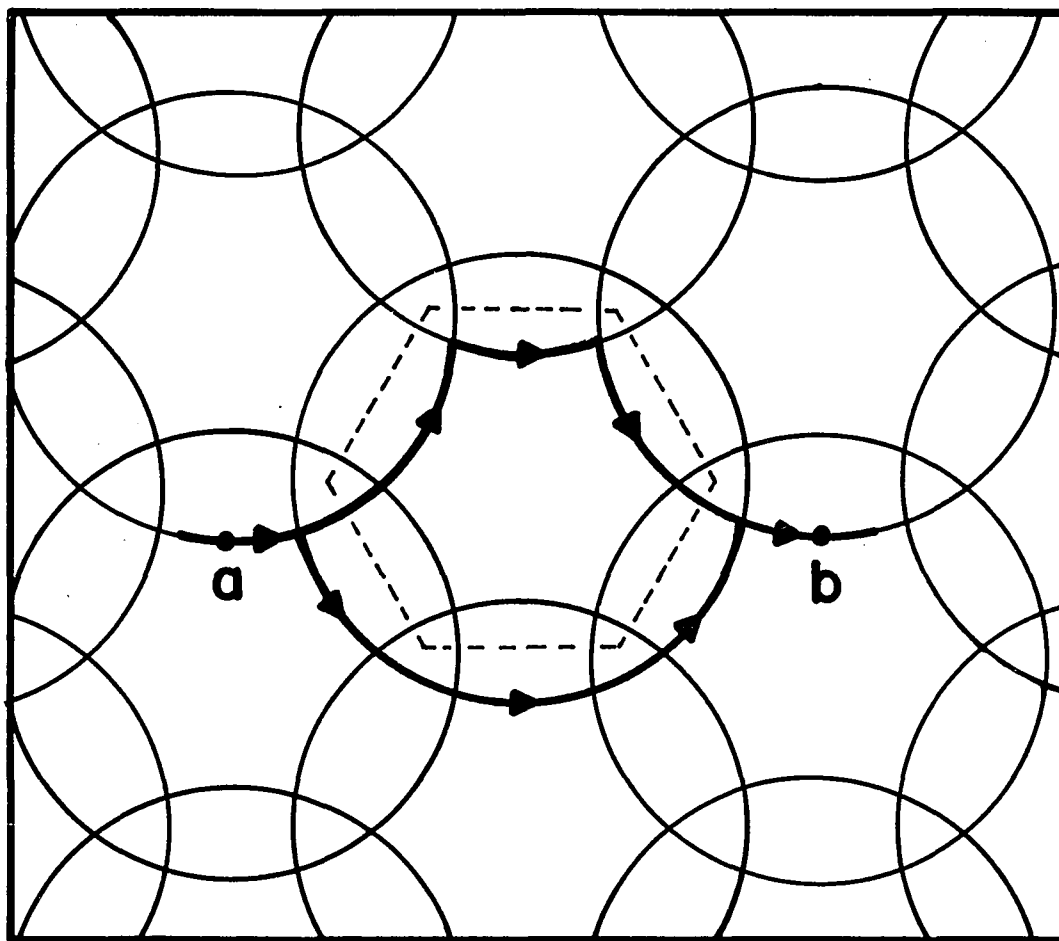


Fig. 40. Two difference paths that enclose the Brillouin zone area $A_{BZ}^{(r)}$.

$$I = \psi_b^* \psi_b = 4p^8 q^4 (1 + \cos \epsilon) \quad (4.5)$$

which can be rewritten

$$I = 4P^4 Q^2 \left[1 + \cos \left(\frac{2\pi F_{BZ}}{H} \right) \right] . \quad (4.6)$$

The intensity at point b will be modulated at the Brillouin zone frequency. For certain values of the field, the probability of traversing path b will be maximized, and at other values the probability will be zero. For a crystal with a finite electron state lifetime, there will be a somewhat enhanced probability for open orbits when the intensity at b is the greatest. When this intensity is maximized the average path length for closure back to 'a' will be greater, and there will be a greater likelihood of a quantum phase randomizing scattering event before the orbit can successfully close. Since the intensity at b is modulated at the frequency of the Brillouin zone, the tendency for open orbits will be modulated at that same frequency. Because open orbits contribute only to the constant (or zero frequency) background of the density of states, this background will also be found to oscillate at the Brillouin zone frequency, and this, in turn, will add an additional oscillatory component to the free energy.

If this interpretation of the peak labeled BZ in Fig. 29 is correct, then we have presented further evidence that a complete theory must include the effects of interference between closed semiclassical orbits.

CHAPTER 5

CONCLUSIONS

The preceding chapters have presented the results of an experimental dHvA study of the coupled orbit system in ultrapure, highly strain-free magnesium. The data collected was compared with the theory of Falicov and Stachowiak and was found to disagree qualitatively. The FS theory was also compared with Pippard's band structure model of the coupled orbit system, and the two theories were shown not to be equivalent. The FS theory is based upon the assumption that there exists a one-to-one correspondence between the harmonic components in the dHvA signal and simple closed semiclassical orbits on the network. The fact that this theory disagrees with Pippard's band structure description and with our experimental data is a strong indication that it is possible to grow crystals of sufficient purity and perfection to enter a regime of quantum coherence for which the electrons on the network can no longer be described in terms of these simple orbits. It appears necessary to invoke a band structure description appropriate to a more fully delocalized electron on the network.

The most useful result that has come out of this investigation is the guidance provided for further research. Two problem areas have been clearly defined as a result of this work. First, computer calculations must be undertaken to derive experimentally verifiable predictions from Pippard's band structure. One approach to this problem was outlined

in the previous chapter. The calculation is straightforward in principle, although there are a number of practical considerations that introduce complications. The second problem is experimental. The band structure regime appears to be intrinsically more difficult to study because the signal power is spread over so many frequencies. Even though the overall magnetization response of the crystal was quite large, the spectral intensity was spread over so many frequencies that the signal to noise ratio in any given frequency band was rather low. As a result of this, it was necessary to go to very low temperatures, and at that point the magnetic interaction effects became crippling. The MI effects will have to be brought under control before quantitative results can be obtained.

APPENDIX A

A CONVERS CASE STUDY

A good way to demonstrate the power and flexibility of Convers is to record an example of how it can be used to control peripheral hardware. Convers is very efficient in hardware control applications, and this was critically important for the purposes of this experiment. When the decision was made to abandon Basic, we were left with no operating system; the disk drivers and the printer drivers had to be entirely rewritten. Convers allowed us to recover quickly the use of these essential system components.

The example presented in this appendix is a software driver for the hardcopy printer. This is about as difficult an interfacing job as one generally has to deal with and will provide a good demonstration of Convers capabilities.

Before getting to the peculiarities of the printer, it is necessary to fill in at least a few additional details about Convers. To begin with, Convers provides the user with an area of memory for use as a scratch pad. This area is structured and controlled as a last-in first-out stack and is typically the means by which the results of a given operation can be left accessible to the user or to a subsequent operation. Numbers can be placed on the stack by typing them in on the input terminal. Any numbers entered this way will be placed on top of numbers already on the stack. The vast majority of Convers commands are designed to accept their arguments from the top of the stack and to

leave their results there when finished. This means that a large part of Convers programming consists of moving these numbers around on the stack so that they appear in the appropriate position at the appropriate time to be accepted as arguments by the command sequence. The user has been provided with a number of stack manipulation primitives to aid in this activity. Five examples of these are DUP, DDUP, SWAP, RL3, and DROP. The easiest way to convey what these commands do is by demonstration. Suppose that the following sequence of numbers was typed on the terminal: 6, 35, 21, 356, and 2. These numbers would be placed on the stack in the order shown.

Typed on the terminal	Stack
	2
	356
6 35 21 356 2	21
	35
	6

The effect of the DUP operation is to duplicate the top number.

	2
	2
	356
DUP	21
	35
	6

The effect of DROP is to discard the top number. This is used to prevent excessive accumulation of numbers on the stack.

	2
	356
DROP	21
	35
	6

SWAP is used to exchange the order of the top two numbers.

Typed on the terminal	Stack
	356
	2
SWAP	21
	35
	6

RL3 is a roll operation involving just the top three numbers.

	21
	356
RL3	2
	35
	6

Finally, DDUP is a double DUP. The effect of this command is no less intuitive.

	21
	356
	21
DDUP	356
	2
	35
	6

It is important to note that all of these manipulations treat the numbers on the stack as 16-bit integers, and each integer is actually stored in two bytes of computer memory. Some commands interpret these numbers as addresses (ranging from 0 to 65,535) while other commands treat them as signed integers (ranging from -32,768 to 32,767). Two operators that fall into the latter category are + and -. Again, the effect of each of these operators is easy to demonstrate. The - command would change the previous stack to that shown here.

Typed on the terminal	Stack
	335
	21
-	356
	2
	35
	6

A second application of - would result in a negative number.

	-314
	356
-	2
	35
	6

If the + were now invoked the result is this.

	42
	2
+	35
	6

Two operators which treat numbers as addresses are @ and !. The @ command is used to retrieve 16-bit numbers from memory. The effect of @ on the above stack would be to replace 42 with the contents of memory location 42 and 43. (Remember that each memory location is only 8 bits in the 8080 system.) The ! is the complementary operator, and the effect that it would have on this same stack would be to store a 16-bit 2 at locations 42 and 43. (A 16-bit 2 is a binary 2 with 14 leading zeros.) The 42 and the 2 are dropped from the stack in this process.

In addition to operators which store and retrieve numbers from memory, there are also commands to communicate with the registers in the 8080 processor. The command STKDE moves the top 16-bit number on the

stack into the D and E registers of the processor. STK-BC moves the top number into the B and C registers. The complementary operators are DE-STK and BC-STK. Note that there is no hyphen in STKDE while the other three names include one. The hyphen is left out of STKDE to allow Convers to see it as distinguishable from STK-BC. This is necessary because Convers stores only the first three characters and the total character count. For STKDE and STK-BC, these identifiers are 5STK and 6STK, respectively. This is an unfortunate limitation which very often results in awkward command names.

The stack system is very efficient for temporary storage of numbers as they are passed as arguments from one operator to the next, but numbers that are kept for longer periods and used only occasionally are better stored in some other manner. When the stack gets too long, the programmer wastes a lot of time shuffling numbers. Convers has provided the solution to this problem in the form of the VARIABLE command. VARIABLE allows the user to associate a name identifier with an address in the dictionary, and this permits convenient long-term storage of numbers. An example of the use of VARIABLE would be the command sentence

```
0 VARIABLE HPOS
```

which creates a new storage location named HPOS and stores a zero in that location as the initial value of the variable. Whenever HPOS is entered on the terminal the dictionary will be searched, and when a match is found, the associated storage address will be placed on the stack. Note that the address (not the value stored at that address) is placed on the stack so that the programmer has the opportunity to

retrieve the stored number with the @ command, or store a new number at that address with the ! command. The usefulness of this construct becomes clear with the aid of an example. Consider the problem of keeping track of the horizontal position of the printhead carriage on the hardcopy printer. When the printer is first turned on, it is initialized to location zero. HPOS will record the carriage position if it is also initialized to zero and then updated whenever the printhead is subsequently moved. Suppose the printhead is to be moved to the right by a distance indicated by the number on top of the stack. The command sequence

```
HPOS @ + HPOS !
```

will cause this change in printhead position to be recorded in HPOS. The succession of events proceeds in five steps. First, the address associated with HPOS is placed on top of the stack. Then the @ command replaces that address with the number stored there. The top two numbers on the stack are now the old printhead position and the move increment, and these are added together by the + command. HPOS then calls the storage address back onto the stack and ! uses the address to store the updated position. For a move to the left, the sequence would be similar.

```
HPOS @ SWAP - HPOS !
```

The - operator subtracts the top number on the stack from the number just beneath it. SWAP has been included so that when the printhead is moved to the left the move increment will be subtracted from the old printhead position.

These command sequences are sufficiently useful functions to warrant their own dictionary identifiers. This is done with the `:` and `;` commands. The `:` throws Convers into the compile mode of operation. After a `:` is entered, the next word typed is established as a new identifier at the end of the dictionary. All commands typed thereafter are located in the dictionary, as usual, but are not immediately executed. Instead, the address of the associated code is used to insert a call to that function into the new dictionary entry. The `;` is used at the end of the defining process to restore Convers to the execution mode. The printhead position sequences will serve as a good illustration. The first sequence can be called RHPOS to indicate that it will update HPOS whenever the printhead is moved to the right. The new definition is established quite simply.

```
      : RHPOS HPOS @ + HPOS ! ;
```

Similarly, the update function for a left carriage move can be called LHPOS.

```
      : LHPOS HPOS @ SWAP - HPOS ! ;
```

Having added these functions to the dictionary, it is no longer necessary to remember the longer sequences. If RHPOS or LHPOS are included in every command that moves the printhead, HPOS will always contain the correct updated position. It is worth stressing again that no dictionary searching is done when these commands are executed. The code that is entered after the LHPOS identifier, for example, would look like this:

```
5LHP CALL HPOS
      CALL @
      CALL SWAP
      CALL -
      CALL HPOS
      CALL !
      RET
```

When LHPOS is executed, each of these previously defined functions is called as a subroutine whose address had been inserted into the calling sequence when LHPOS was defined. The only time penalty associated with the execution of LHPOS is related to the modular structure of the code.

In many cases, it is necessary to create definitions which cannot be defined in terms of previous Convers commands. A good example of this is the lift ribbon function on the printer. The hardware manual stipulates that the printer will raise its typewriter ribbon into the position for printing when the following 8080 machine code sequence is executed.

```
76
372
323
67
```

These numbers are given in octal. Without worrying about the meaning of this list of numbers, it would be useful if a command could be defined to execute them, and thereby control the printer ribbon. Convers has provided this capability in the form of the CODE and RTN commands.

These are similar to the : and ; commands except they never throw Convers into the compile mode. After CODE is typed on the terminal, the system accepts the next word as a new name identifier and carries out the usual administrative details associated with adding a new entry to the

dictionary: But rather than waiting in the compile mode for Convers commands to compile into the dictionary, the system instead remains in the execute mode and waits for the user to insert machine code into the dictionary directly. This is done with the `1`, and the `,` (comma) commands. The first of these takes the lowest order byte of the top 16-bit number on the stack, appends that byte at the current end of the dictionary, and increments the dictionary pointer. The `,` command does exactly the same job, but the entire 16-bit number goes into the dictionary. `RTN` is used to close out the definition after all of the machine code has been inserted. Using these function, the lift-ribbon command would be defined like this:

```
CODE LIFT-RIBBON 76 1, 372 1, 323 1, 67 1, RTN.
```

Because the system is in the execute mode during the definition, each of the numbers entered on the terminal is pushed on the stack as a 16-bit integer, and once on the stack it is accessible to the `1`, command.

These kinds of definitions, which rely heavily upon direct insertion of machine code, are much harder to read and understand than the same definitions written in standard assembly code. The printer driver software will involve several such machine level functions. For the sake of readability, and as a further demonstration of Convers flexibility, I will digress briefly and define an abridged 8080 assembler. Table 3 lists the 8080 machine code that will be necessary for the character printer driver. The associated assembly code mnemonics and the meaning of the instructions are also listed. These mnemonics can be defined as assembly operators simply by using the `1`, command in the

TABLE 3. An abridged listing of 8080 assembly code.

Mnemonic	Machine Code	Meaning of Instruction
ADD A	207	Add the accumulator to the accumulator.
ANI n	346 n	And the following byte with the accumulator.
CMA	57	Complement the accumulator.
CMP B	270	Compare register B with the accumulator.
CMP D	272	Compare register D with the accumulator.
DAD H	51	Add register pair H and L to register pair H and L.
DCR E	35	Decrement register E.
IN n	333 n	Input to accumulator from port specified by the following byte.
INR E	34	Increment register E.
INX B	3	Increment register pair B and C.
INX H	43	Increment register pair H and L.
JNZ nn	302 n n	Jump if zero flag is not set to address specified by following two bytes.
LXI B,nn	1 n n	Load the following two bytes into register pair B and C.
MOV A,C	171	Move register C to the accumulator.
MOV A,D	172	Move register D to the accumulator.
MOV A,E	173	Move register E to the accumulator.
MOV A,M	176	Move to the accumulator the contents of the memory location specified by register pair H and L.

TABLE 3 - Continued

Mnemonic	Machine Code	Meaning of Instruction
MOV D,A	127	Move the accumulator to register D.
MVI A,n	76 n	Load the following byte into the accumulator.
MVI D,n	26 n	Load the following byte into register D.
ORA D	262	Or register D with the accumulator.
ORI n	366 n	Or the following byte with the accumulator.
OUT n	323 n	Output accumulator to port specified by the following byte.
RZ	310	Return if the zero flag has been set.
XCHG	353	Exchange register pair H and L with register pair D and E.
XRA A	257	Zero the accumulator.
XRI n	356 n	Exclusive Or the following byte with the accumulator.

compile mode. For example, the ADD A mnemonic can be defined as the operator ADDA.

```
: ADDA 207 1, ;
```

When a number is entered on the terminal, the reaction of Convers depends upon whether the system is in the compile or execute mode. When in the execute mode, the system reaction is simply to push the number on the stack. If Convers is in the compile mode, the number is treated as a literal and is compiled into the dictionary. When later that dictionary entry is executed, the number will then be pushed on the stack. Specifically, when ADDA is executed, the 207 will be placed on the stack and then the 1, will be executed, moving the 207 to the current end of the dictionary. Every execution of ADDA will place a 207 at the end of the dictionary. ADDA has become an assembly code operator. If such an operator is defined for every machine code possibility, we will have defined an assembler. Table 4 shows an abridged assembler corresponding to the mnemonics listed in Table 3. Note that the strict correspondence with standard mnemonics has been relaxed in the case of the MOV, MVI, INX, and CMP instructions. Each of these appears more than once in the list, and the names had to be reordered so Convers could distinguish among them.

With an assembler defined, the LIFT-RIBBON function can be re-defined in more transparent notation.

```
CODE LIFT-RIBBON AMVI 372 1, OUT 67 1, RTN
```

There is an obvious correspondence between this Convers command

TABLE 4. An abridged 8080 assembler defined in Convers code.

Standard Assembly Code Mnemonic	Convers Assembly Code Operator	Definition of Operator
ADD A	ADDA	: ADDA 207 1, ;
ANI n	ANI	: ANI 346 1, ;
CMA	CMA	: CMA 57 1, ;
CMP B	BCMP	: BCMP 270 1, ;
CMP D	DCMP	: DCMP 272 1, ;
DAD H	DADH	: DADH 51 1, ;
DCR E	DCRE	: DCRE 35 1, ;
IN n	IN	: IN 333 1, ;
INR E	INRE	: INRE 34 1, ;
INX B	BINX	: BINX 3 1, ;
INX H	HINX	: HINX 43 1, ;
JNZ nn	JNZ	: JNZ 302 1, ;
LXI B,nn	LXIB	: LXIB 1 1, ;
MOV A,C	ACMOV	: ACMOV 171 1, ;
MOV A,D	ADMOV	: ADMOV 172 1, ;
MOV A,E	AEMOV	: AEMOV 173 1, ;
MOV A,M	AMMOV	: AMMOV 176 1, ;
MOV D,A	DAMOV	: DAMOV 127 1, ;
MVI A,n	AMVI	: AMVI 76 1, ;
MVI D,n	DMVI	: DMVI 26 1, ;
MVI E,n	EMVI	: EMVI 36 1, ;

TABLE 4 - Continued

Standard Assembly Code Mnemonic	Convers Assembly Code Operator	Definition of Operator
ORA D	ORAD	: ORAD 262 1, ;
ORI n	ORI	: ORI 366 1, ;
OUT n	OUT	: OUT 323 1, ;
RZ	RZ	: RZ 310 1, ;
XCHG	XCHG	: XCHG 353 1, ;
XRA A	XRAA	: XRAA 257 1, ;
XRI n	XRI	: XRI 356 1, ;

definition and the equivalent assembly code macro.

```
13LIF MVI A, 372
      OUT 67
      RET.
```

It is now much easier to see that the way to lift the printer ribbon is to transmit a 372 to port number 67.

This simple assembler becomes quite powerful when used with the Convers COMPILE, HERE, and ' (apostrophe) commands. The ' command is used to look up the address of a previously defined Convers operator. For example

```
' DUP
```

would initiate a dictionary search for DUP, and when it was found, the starting address would be placed on the stack. When COMPILE is executed, the top 16-bit number on the stack is inserted into the dictionary after an 8080 machine code call instruction. COMPILE is usually used with '. The sequence

```
' DUP COMPILE
```

would append a call to the operator DUP at the end of the dictionary. This is how previously defined Convers operators can be included in CODE definitions. HERE is used to keep track of jump addresses within a CODE definition. When HERE is entered on the terminal, the address of the first byte beyond the end of the dictionary is placed on the stack. This address can later be inserted into a jump instruction that follows the HERE command in the defining sequence. Again, the best way to make

these things clear is by specific demonstration. A good example is provided by the Buffer-Ready function that will have to be included in the printer driver software. The hardware manual specifies that bit 7 of port 65 must go to zero before any move or print characters are sent to the printer. The following Convers command is defined to check this.

```
CODE BREADY HERE IN 65 1, ANI 200 1, JNZ , RTN
```

Port 65 is input into accumulator and masked for bit 7. If this bit is not zero, the jump is executed. Note that the address of the jump has been provided by the HERE command. This function is an endless loop as long as the printer buffer remains unready, and hence this routine would halt Convers if something should cause a problem with the printer (ribbon out, head move out of bounds, etc). To avoid this problem, an error recovery routine can be inserted into a redefined version of the function.

```
CODE BREADY LXIB 0 , HERE IN 65 1, ANI 200 1, RZ
BINX AMVI 300 1, CMPB JNZ , ' RETERR COMPILE RTN
```

In this version a counter is maintained in the B and C registers, and the function will continue to wait for a Buffer-Ready indication until the counter reaches a cutoff value (140000_8). When this happens, the function branches to RETERR which is an error recovery function that returns the system to operator control. Once again, there is a clear correspondence between this Convers definition and the equivalent assembler macro.

```
6BRE LXI B,0
HERE IN 65
      ANI 200
      RZ
      INX B
      MVI A,300
      CMP B
      JNZ HERE
      CALL RETERR
      RET
```

Furthermore, like the assembly code version, the Convers definition is completely relocatable even though the function includes an internal jump. As long as it contains no undefined functions, it will run correctly wherever it is placed in the dictionary.

Although the foregoing introduction to Convers has left out much more than it has included, the inventory of operators that has been discussed will be sufficient for the development of printer control software. This printer (the Altair Q70[®] printer manufacture by Qume, Inc.) is typical of hardware designed for computer environments in that all of its considerable capabilities can be reduced to just a few basic functions. The printer can be initialized, lift the ribbon, move the print-head, move the paper, and print a character. Also typical is the fact that each of these functions can be controlled by a well-defined command sequence that is provided by the manufacturer. In the discussion that follows, these command sequences will be absorbed into Convers definitions and then coordinated into a convenient, high level printer control system.

To begin, the printer must be initialized. The command sequence is provided in 8080 assembly code.

```

IOPTR  XRA  A
        OUT 60
        OUT 62
        OUT 64
        OUT 66
        OUT 65
        CMA
        OUT 61
        OUT 63
        OUT 67
        MVI A,44
        OUT 60
        OUT 62
        OUT 64
        OUT 66
        MVI A,374
        OUT 67
        RET

```

The printer is wired to computer I/O ports 60 through 67. This sequence readies these ports and then transmits the initializing bit pattern (374) to the printer. This function can be defined almost verbatim in Convers.

```

CODE PTR-INIT XRAA OUT 60 1, OUT 62 1, OUT 64 1, 66 1
65 1, CMA OUT 61 1, OUT 63 1, OUT 67 1, AMVI 44 1,
OUT 60 1, OUT 62 1, OUT 64 1, OUT 66 1, AMVI 374 1,
OUT 67 1, RTN

```

Horizontal movement of the printhead is controlled by the following command sequence:

```

6HMO   MOV  A,E
        DMA
        OUT 61
        MOV A,D
        CMA
        OUT 63
        XRI 100
        OUT 63
        ORI 100
        OUT 63
        RET

```

The move increment is loaded from the D and E registers into the accumulator and transmitted out to ports 61 and 63. Once that information has been latched into the data register of the printer, the carriage move is acutated by transmitting a 0 bit 6 to port 63. The end of the sequence is signaled by a 377 sent to the same port. Written in Convers, this function is

```
CODE HMOVE* AEMOV CMA OUT 61 1, ADMOV CMA OUT 63 1,
XRI 100 1, OUT 63 1, ORI 100 1, OUT 63 1, RTN
```

The move is to the right unless bit 3 of register D has been set to 1. A function is needed to set this bit whenever the move is to be to the left.

```
CODE LEFT AMVI 10 1, OTAD DAMOV RTN
```

Two functions can now be defined to move the printhead left or right by an increment specified by the top number on the stack.

```
: RMOVE RHPOS STDKE BREADY HMOVE* ;
: LMOVE LHPOS STKDE LEFT BREADY HMOVE* ;
```

BREADY has been included to insure that the printer data buffer is ready to accept a command. RHPOS and LHPOS will update the head position counter HPOS.

The paper movement instruction sequence is quite similar to what was given for carriage movement.

```

6VMO  MOV A,E
      CAM
      OUT 61
      MOV A,D
      CMA
      OUT 63
      XRI 200
      OUT 63
      ORI 200
      OUT 63
      RET

```

This sequence differs only in the last two bytes sent to port 63. An octal 100 was used to command a carriage move while a 200 is used here to move the paper. Again, the size of the move increment must be left in the D and E registers. In Convers this definition is written

```

CODE VMOVE* AEMOV CAM OUT 61 1, ADMOV CMA OUT 63 1,
XRI 200 1, OUT 63 1, ORI 200 1, OUT 63 1, RTN.

```

There is one hardware peculiarity associated with paper movement; the printer data register bit 0 is ignored. This means that the mover increment must be left shifted one place in the D and E registers before it is transmitted to the printer. This can be programmed separately.

```

: 1LSHFT SCHG DADH XCHG RTN ;

```

and included in the high level paper movement commands.

```

: FMOVE STKDE 1LSHFT BREADY VMOVE* ;
: BMOVE STKDE 1LSHFT LEFT BREADY VMOVE ;

```

Note that the LEFT command was used to signal backward feed of the paper. In this context, bit 3 of register D signals paper retard.

This printer is designed to allow the programmer to control the location of the printhead to 1/120 inch horizontally and 1/48 inch vertically. This feature allows the printer to be used in a wide variety of ways which would be impossible if the printhead were confined to large discrete movements like that of a teletype. However, there is a penalty to pay for this; the printer does not recognize many of the usual printer control characters such as space, carriage return, and line feed. The functions that have just been defined can easily be used to simulate these commands.

```
: FSPACE 12 RMOVE ;  
: BSPACE 12 LMOVE ;  
: LF 10 FMOVE ;
```

These are self-explanatory except to say that the space functions will move the carriage 1/12 inch while the LF command advances the paper 1/6 inch. (These are octal numbers and the basic move increments are 1/120 inch and 1/48 inch, respectively.) The carriage return is almost as easily constructed. The variable HPOS is used to specify the printhead move increment.

```
: CR HPOS @ LMOVE ;
```

The only printer function left undefined is the actual character printing. Again, the command sequence has been specified by the manufacturer.

```

11C-P  MOV  A,C
        ADD  A
        CMA
        OUT  61
        CALL WAIT
        MVI  A,337
        OUT  63
        ORI  40
        OUT  63
        RET

```

and again the Convers equivalent is easily derived from this list.

```

CODE C-PRINT** ACMOV ADDA CMA OUT 61 1, ' BREADY
COMPILE AMVI 337 1, OUT 63 1, ORI 40 1, OUT 63 1,
RTN

```

The BREADY function serves the same purpose as the WAIT subroutine defined by the manufacturer. C-PRINT** prints the character corresponding to the ASCII code left in the C register. This code can be easily moved there from the stack.

```

: C-PRINT* STK-BC C-PRINT** ;

```

It would be even more convenient to use a character printing function that expected an address on the stack. Such a function could be put in a loop and, by incrementing the address on each cycle, made to print character strings of arbitrary length. In addition, the function must intercept the ASCII code for space (octal 40) because the printer interprets this as a printable character. The following function answers both of these requirements:

```

: C-PRINT 1@ OPUSH DUP 40 - IF C-PRINT* ELSE DROP THEN ;

```

The 1@ command fetches the 8-bit byte located at the address left on the

stack, and OPUSH restores this number to a full 16 bits by pushing on a byte of leading zeros. This 16-bit number can then be duplicated and checked for octal 40. The IF-ELSE-THEN construct is defined to execute the code between ELSE and THEN if a zero is left on the top of the stack; otherwise, the code between IF and ELSE is executed. In this context if the character code is a 40, then the duplicate copy is dropped and the function does nothing. If the code is any other ASCII character, the duplicate is printed by C-PRINT*. Once the character printing function is defined in this form, it will fit easily into a string printing loop.

```
: STR-PRINT 1 DO DUP C-PRINT FSPACE 1 + LOOP DROP ;
```

The DO-LOOP construct is defined to repeatedly execute the functions that appear between DO and LOOP. The two top numbers on the stack at the time DO is encountered will determine the number of times the loop is executed. For example, the function DEMO defined as

```
: DEMO 5 1 DO 377 1, LOOP ;
```

will append 5 377 bytes to the end of the dictionary. STR-PRINT expects a number and an address on the stack. The number will be used to determine the length of the loop, and the address will be used to fetch a character and then be incremented each time the loop is executed. STR-PRINT becomes a line printing function if it is given the number of characters between carriage returns. The function LENGTH can be defined to provide this number.

```

CODE LENGTH ' STKDE COMPILE EXHG DMVI 15 1, EMVI 0 1,
HERE AMMOV HINX INRE DCOMP JNZ, DMVI 0 1, DCRE '
DE-STK COMPILE RTN

```

This function starts at a given address and counts locations until it finds a carriage return (octal 15). When a carriage return is found, the length of the line is left as the top number on the stack where it can be picked up by STR-PRINT.

```

: LINE-PRINT DUP LENGTH DDUP 2 + + RL3 RLs STR-PRINT CR LF ;

```

LINE-PRINT expects only starting address to be left on the stack. It will go to that address and print out whatever text is stored there until the first carriage return. It will then execute a carriage return, a line feed, and leave the starting address of the next line on the stack. If a page of output is desired, this command need only be placed in a loop which specifies the number of lines on a page.

With this function defined, the software support of textual output on the printer is essentially complete. Moreover, the simple system described above is sufficiently flexible to be used as a base for output problems that are quite different from text printing. For example, the problem of programming a plotting capability is simply a matter of getting the correct x and y move increments to the functions RMOVE, LMOVE, FMOVE, and BMOVE that have already been defined.

Software similar to this makes up the printer driver portion of our data processing system. But this system also contains the necessary software to control the disks, the floating point processor, and the analog-to-digital converter. In addition, there are program

functions to manipulate large lists of numbers, perform FFT calculations (with all of the associated sin-cos, bit flipping, and scrambling operations), and generate hardcopy spectrum displays. All of this processing power is in the computer simultaneously, and each of these functions is accessed by its associated single word command name. Because the entire system resides in less than 32 kbytes of 8-bit memory, there is enough storage space to perform calculations on 5000 point data lists to 8 decimal digit precision without a single disk access.

The best way to demonstrate the impact of this software system on the conduct of our experiment is to describe the system response to the single command 1/HSWEEP. The operator types this command after setting up the analog electronics for a particular experimental situation. The computer begins by requesting the sweep parameters which are different from default values. After these have been entered, the trigger point table is calculated and the computer asks for an operator signal that the sweep has begun. Once this signal is given, the computer will start accepting data when the field reaches the start sweep value. From then on the entire analysis process is under computer control. First, the sweep is digitalized and the resulting binary data copied onto disk storage. Then, the excess bits are stripped, the list is transformed into floating point code, and an FFT is calculated. After several minutes (how many minutes depends upon the length of the list), a header sheet is printed which displays a record of all of the experimental parameters for that sweep, and this is followed on the printer by a scaled spectrum plot displaying the results of the FFT.

REFERENCES

- Alles, H.G., and R.J. Higgins (1975). Rev. Sci. Instr. 46, 963.
- Ashcroft, N.W. (1963). Phil. Mag. 8, 2055.
- Blount, E.I. (1962). Phys. Rev. 126, 1636.
- Brigham, E.O. (1974). The Fast Fourier Transform, Prentice-Hall, Englewood Cliffs, New Jersey.
- Chambers, R.G. (1966). Proc. Phys. Soc. 88, 701.
- Cohen, M.H., and L.M. Falicov (1961). Phys. Rev. Lett. 7, 231.
- Cooley, J.W., and J.W. Tukey (1965). Math. Computation 19, 297.
- Dingle, R.B. (1952). Proc. Roy. Soc. A211, 500.
- Edwards, D.O., D.F. Brewer, P. Selignan, M. Skertic, and M. Yaqub (1965). Phys. Rev. Lett. 15, 773.
- Falicov, L.M., A.B. Pippard, and Paul R. Sievert (1966). Phys. Rev. 151, 498.
- Falicov, L.M., and Henryk Stachowiak (1966). Phys. Rev. 147, 505.
- Karim, D.P., J.B. Ketterson, and G.W. Crabtree (1978). J. Low Temp. Phys. 30, 389.
- Lifshitz, I.M., and A.M. Kosevich (1956). Soviet Phys. -- JETP 2, 636.
- Lounasmaa, O.V. (1974). Experimental Principles and Methods Below 1K, Academic Press, New York, pp. 17 ff.
- Pippard, A.B. (1962). Proc. Roy. Soc. A270, 1.
- Pippard, A.B. (1963). Proc. Roy. Soc. A272, 192.
- Pippard, A.B. (1964). Phil. Trans. Roy. Soc. A256, 317.
- Priestley, M.G. (1963). Proc. Roy. Soc. A276, 258.
- Priestley, M.G., L.M. Falicov, and G. Weisz (1963). Phys. Rev. 131, 617.

- Reifenberger, R. (1977). *J. Low Temp. Phys.* 26, 831.
- Reitz, J.R. (1964). *J. Phys. Chem. Solids* 25, 53.
- Ruvalds, J. (1969). *J. Phys. Chem. Solids* 30, 305.
- Schoenberg, D. (1962). *Phil. Trans. Roy. Soc.* A255, 85.
- Schoenberg, D., and P.J. Stiles (1964). *Proc. Roy. Soc.* A281, 62.
- Stark, R.W. (1962). *Phys. Rev. Lett.* 9, 482.
- Stark, R.W. (1964). *Phys. Rev.* 135, A1968.
- Stark, R.W. (1965). *Proc. IXth Int. Conf. Low Temp. Phys.*, Plenum Press, New York, pp. 712.
- Stark, R.W. (1967). 162, 589.
- Stark, R.W. (1977). Private communication. These high frequencies were observed in 1967.
- Stark, R.W., T.G. Eck, W.L. Gordon, and F. Moazed (1962). *Phys. Rev. Lett.* 8, 360.
- Stark, R.W. and L.R. Windmiller (1968). *Cryogenics* 8, 272.
- Tilden, S.B., and M.B. Denton (1978). Convers -- An Interpretive Compiler, Chemistry Department, University of Arizona.
- Tilden, S.B., and M.B. Denton (1979). *J. Auto. Chem.* 1, 128.
- Tukey, J.W. (1967). In Spectral Analysis of Time Series, B. Harris, ed., Wiley, New York, pp. 25.
- White, G.K. (1968). Experimental Techniques in Low Temperature Physics, 2nd ed., Oxford University Press, London, pp. 162 ff.
- Young, R.C. (1965). *Phys. Rev. Lett.* 15, 262.